

UNIVERSITY OF SOUTHERN DENMARK

MASTER THESIS

**Light-Matter Interactions in
Two-Dimensional Materials And
Nanostructured Waveguides**

Supervisor

Prof. S. Hofferberth
Prof. N. A. MORTENSEN
Dr. P. A. D. GONÇALVES
Assist. Prof. J. D. COX

Author

T. P. RASMUSSEN



May 31, 2020

Abstract

This thesis presents a broad range of descriptions regarding classical plasmonic systems in two- and three-dimensions, with special attention to the 2D material graphene.

The first part of the thesis introduces the fundamental concepts of classical electrodynamics, which constitute the building blocks necessary to describe classical plasmonics. This framework is then used to develop the theoretical description of plasmonic excitations at planar dielectric-metal interfaces, where the dispersion relation is derived at both single and double interface geometries. The hybridized modes of the double-layer systems have then been identified, along with the possibility of tuning these modes by variation of the interface separation. Next, after having dealt with plasmonics in 3D, the attention is turned to the 2D material graphene, where the corresponding electronic and optical properties are studied. Utilizing the tight-binding method reveals the particle-hole symmetric electronic band structure of undoped graphene, together with its low-energy linear spectrum in the vicinity of the Dirac points, which is responsible for the excellent electronic features of this material. A brief investigation of graphene's conductivity is performed, which demonstrates a Drude-like conductivity in THz to mid-IR frequency region for doped graphene. This coverage of the conductivity is followed by an outline of the transfer-matrix method in systems containing one or two planar graphene sheets, from which the constant absorbance of graphene at visible frequencies is derived. Equipped with the optoelectronic insights of graphene, the physics governing plasmonic excitations in single and double planar graphene systems is presented, which enlightens the ability to actively tune the resonance frequency in graphene through adjustments of the doping level. The dispersion relation is presented for both systems, which display an impressive degree of field confinement at frequencies in THz to mid-IR spectral region, as opposed to the light-like dispersion of SPPs at dielectric-metal interfaces in this regime.

Finally a study of parabolic shaped waveguides have been carried out. The dispersion relation is derived for a Drude metal parabolic channel, which is followed by the same analysis in a graphene-covered dielectric waveguide, leading to the findings of ultra-confined surface plasmons, exceeding those in planar graphene.

Resumé

Denne afhandling præsenterer en bred vifte af beskrivelser omhandlende plasmoniske systemer i to og tredimensionale systemer, med ekstra fokus på 2D materialet grafen.

Den første del af afhandlingen introducerer de fundamentale koncepter i klassisk elektrodynamik, hvilket udgør de nødvendige byggesten til at udarbejde klassisk *plasmonics*. Disse rammer er derefter brugt til at udvikle den teoretiske beskrivelse af plasmoniske excitationer ved plane dielektrisk-metal grænseflader, hvor *dispersion relation* er udledt for både geometrier af enkelt og dobbelte grænseflader. De hybridiserede plasmontilstande i den dobbelte grænsefladegeometri er derefter blevet identificeret, sammen med muligheden for at justere disse tilstande ved variation af separationen mellem grænsefladerne. Dernæst, efter at have kortlagt beskrivelsen af *plasmonics* i 3D, bliver fokuset drejet mod 2D materialet grafen, hvor de tilsvarende elektroniske og optiske egenskaber bliver studeret. Anvendelse af *Tight-Binding* modellen afdækker den symmetriske partikel-hul båndstruktur af doteret grafen, sammen med dets lineære lavenergiske spektrum i nærheden af Dirac punktet, hvilket er grunden til de fantastiske elektronske egenskaber i dette materiale. En kort beskrivelse af konduktiviteten af grafen er udarbejdet, hvilket demonstrerer en Drudeliggende konduktivitet for doteret grafen i frekvensintervallet fra THz til midt IR. Denne gennemgang af konduktiviteten er efterfulgt af en skitsering af transfer-matrix metoden i systemer med en og to plane grafenplader, hvorfra den konstante absorbans ved synlige frekvenser er udledt. Udstyret med indsigten i de optiske og elektronske egenskaber af grafen, bliver den fysiske beskrivelse af plasmoniske excitationer i plane enkelt og dobbeltlag grafen systemer præsenteret, hvilket belyser grafens evne til aktivt at justere resonansfrekvensen gennem variation af doteringsniveauet. *Dispersion relation* bliver præsenteret for begge systemer, hvilket viser en imponerende grad af lyslokalisering for frekvenser omkring midt IR i det elektromagnetiske spektrum, i modsætning til den lyslignende *dispersion relation* for konventionelle overfladeplasmoner i dette regime.

Til sidst er paraboliske bølgekanaler blevet studeret. *Dispersion relation* for en parabolisk bølgekanal lavet af et Drudemetal er blevet udledt, hvilket er efterfulgt af en identisk analyse for en dielektrisk bølgekanal overdækket af grafen. Denne udbyggende analyse fører til opdagelsen af en ekstraordinær lyslokalisering, som overgår lokaliseringsen i fladt grafen.

Acknowledgement

First of all I would like to thank my main supervisors, Prof. N. Asger Mortensen and Prof. S. Hofferberth, for providing me with the opportunity to write this thesis and to guide me throughout the process. A special thanks should go to Asger, for his constant encouragement and openness to all sorts of questions with scientific as well as personal character.

In addition, I wish to thank my two co-supervisors, P. A. D. Gonçalves and J. D. Cox, for their great patience, open door, and far-reaching knowledge on the subjects of the thesis, which lead to a lot of insightful and inspiring discussions.

I would like to express my deepest gratitude to the whole of the Quantum Plasmonics group, who have made the past year very enjoyable, and have sparked my interest in the field of plasmonics and the art of research in general. This highly professional environment have kept my motivation and curiosity high throughout the thesis.

On a more personal level, I would like to extend my thanks to my friends and family for, once in a while, providing me with distractions from physics. Especially I express a profound thankfulness to my close family for their endless support in a very difficult time of my master degree. I could not have succeeded in this degree if it wasn't for them.

Contents

Abstract	i
Resumé	ii
Acknowledgement	iii
1 Introduction	1
2 Electromagnetic Properties of Solids	3
2.1 Fundamentals of Classical Electrodynamics	3
2.1.1 Maxwell's equation and response functions	3
2.1.2 The local-response approximation	6
2.1.3 Boundary conditions at interfaces	6
2.2 The Drude model	7
3 Surface Plasmon Polaritons at Metal/Dielectric Interfaces	10
3.1 Single Dielectric-Metal Interface	10
3.1.1 Dispersion relation	11
3.1.2 Propagation length and field confinement	14
3.2 Double Dielectric-Metal Interface	16
3.2.1 Dispersion relation	17
4 Optical and Electronic Properties of Graphene	21
4.1 Electronic band structure of graphene	21
4.1.1 Real and reciprocal space description of graphene	21
4.1.2 The tight-binding model	23
4.1.3 Massless Dirac Hamiltonian	25
4.2 Conductivity of graphene	26
4.3 Transfer-matrix method for graphene	28
4.3.1 Transfer-matrix for single graphene layer	28
4.3.2 Transfer-matrix for double graphene layer	31
5 Plasmonic Excitation in Graphene	33
5.1 Single Graphene Interface	33
5.1.1 GSP dispersion relation	34

5.1.2	Penetration depth and field confinement for GSPs	37
5.1.3	Numerical example of GSP localization	38
5.1.4	Single-layer graphene fields profile of GSPs	39
5.2	Double Graphene Interface	41
5.2.1	Spectrum of double-layer graphene geometry	41
5.2.2	Alternative approach to DLG dispersion	43
6	Plasmons in Parabolic Waveguides	45
6.1	Parabolic Waveguides	45
6.1.1	Dispersion relation	46
6.2	Graphene-covered parabolic waveguide: Bulges and Valleys	50
7	Conclusions And Outlook	55
	Appendices	57
A	Transparency of Graphene	58
B	Excitation of GSPs	61
C	Guided Plasmons in the Hyperbolic Wedge Geometry	67
	Bibliography	76

Acronyms

1D One-dimensional

2D Two-dimensional

3D Three-dimensional

BGP Bulge graphene plasmon

CPP Channel plasmon polariton

DFT Density functional theory

DLG Double layer graphene

DMD Dielectric-metal-dielectric

DOS Density of states

GSP Graphene surface plasmon

IR Infrared

LRA Local-response approximation

LSP Localized surface plasmon

MDM Metal-dielectric-metal

RPA Random-phase approximation

SLG Single layer graphene

SPP Surface plasmon polariton

TB Tight-binding

TE Transverse electric

TM Transverse magnetic

VGP Valley graphene plasmon

VPP Volume plasmon polariton

Chapter 1

Introduction

Light has been an essential part of science to mankind since the beginning of our documented time. Light was used by the ancient people to acquire knowledge about the distant stars of the universe, and is used today to study objects at the microscopic length scale. One of the biggest breakthroughs in science came along with the dynamical theory of the electromagnetic field, published by Maxwell in 1865 [1], which laid out a crucial foundation for the technological revolution in the upcoming centuries. One such example is the branch of physics called nanophotonics, in which the fascinating field of plasmonics lies.

Plasmonics - the main subject of this thesis - deals with the study of plasmons, which classically are viewed as collective excitations in the free-electron plasma of a metal, mediated by the Coulomb force. The first microscopic description of plasmons were given by Pines and Bohm in 1952 [2], where a quantum mechanical theory, called the random-phase approximation (RPA), was established.

Plasmons in thin films was initially considered by Ritchie in 1957 [3], which introduced the concept of surface plasmons. The idea is that the plasmons at the surface of the conductor couples to free-space electromagnetic radiation. The resulting quasi-particle is termed a surface plasmon polariton (SPP) if the coupling takes place at a planar interface, or localized surface plasmon (LSP) if it takes place at a closed surface of a small particle [4]. Although the theoretical groundwork was covered in the 20th century, decorative exploitation of the plasmons dates multiple centuries, even millennia, back in time. Common examples of such uses is the famous Lycurgus cup, or the stained glass windows in Gothic churches, where the illustrative colors in both cases is caused by nanoscopic gold particles supporting LSPs.

Surface plasmons have the ability to confine light beyond the diffraction limit, which enables substantially higher local field intensity and the possibility of subwavelength waveguiding. Plasmonics have advanced to a great extent throughout the last couple of decades, owed to the extensive improvement of characterization and nanofabrication techniques. The interest in this field have especially increased in the scientific community in recent years, which is partly due to the study of the two dimensional material graphene. Graphene - isolated for the first time in 2004 [5] - is a 2D allotrope of carbon with its carbon atoms

arranged in an hexagonal in-plane crystalline structure. Graphene exhibits outstanding electronic and thermal as well as mechanical properties; It possesses a remarkably large thermal conductivity [6], its free low-energy electrons behave as massless Dirac fermions described by the relativistic Dirac Hamiltonian [7], and to top it all off, the graphene sheet is flexible. Doped graphene is able to sustain plasmonic excitations in the THz to mid-IR spectral region - this excitation is called a graphene surface plasmon (GSP). The resonant frequency of the GSPs depend on the doping level, which is to say that graphene is tunable. This ability to actively tune GSPs is of vital importance when it comes to the potential implementation of graphene in technological devices.

The first part of this thesis deals with the classical description of plasmonics, which is build upon the foundation of classical electrodynamics. In this framework the dispersion relation of SPPs propagation along single planer dielectric-metal interfaces is discussed, along with the corresponding field confinement and propagation length. The ideas developed in these discussions is then extended to SPPs in double interface geometries, more specifically dielectric-metal-dielectric (DMD) and metal-dielectric-metal (MDM) structures. The second part of the thesis introduces the important optical and electronic properties of graphene, which is used to derive the plasmonic excitations in single-layer graphene (SLG) and double-layer graphene (DLG). Finally the last chapter of the thesis introduces the concept of subwavelength waveguides. First the dispersion relation is derived in a Drude-metal parabolic channel in the electrostatic limit, then the same procedure is used for a graphene-covered dielectric parabolic bulge and valley. The discussion of the graphene-free parabolic channel in the thesis is merely a reproduction of already existing papers, while the research on the graphene-covered parabola have been conducted by the author, guided by the supervisors.

Chapter 2

Electromagnetic Properties of Solids

2.1 Fundamentals of Classical Electrodynamics

2.1.1 Maxwell's equation and response functions

It is possible to describe the interaction of metals with electromagnetic radiation in the classical framework of Maxwell's macroscopic equations. This is a favourable approach since the rapidly changing microscopic fields from interaction between charged particles in the metal and electromagnetic waves can be omitted by the exchange of an overall averaged macroscopic field. Maxwell's equations of macroscopic electromagnetism read as¹ [8]

$$\nabla \cdot \mathbf{D}(\mathbf{r}, t) = \rho_f(\mathbf{r}, t), \quad (2.1.1a)$$

$$\nabla \cdot \mathbf{B}(\mathbf{r}, t) = 0, \quad (2.1.1b)$$

$$\nabla \times \mathbf{E}(\mathbf{r}, t) = -\frac{\partial \mathbf{B}(\mathbf{r}, t)}{\partial t}, \quad (2.1.1c)$$

$$\nabla \times \mathbf{H}(\mathbf{r}, t) = \mathbf{J}_f(\mathbf{r}, t) + \frac{\partial \mathbf{D}(\mathbf{r}, t)}{\partial t}, \quad (2.1.1d)$$

where \mathbf{E} denotes the electric field, \mathbf{H} the magnetic field, \mathbf{D} the electric displacement and \mathbf{B} the magnetic induction, while \mathbf{J}_f and ρ_f represents the free current density and charge density, respectively. The free current and charge density is separated into the induced and external parts as $\mathbf{J}_f = \mathbf{J}_{\text{ind}} + \mathbf{J}_{\text{ext}}$ and $\rho_f = \rho_{\text{ind}} + \rho_{\text{ext}}$, which satisfies the continuity equation

$$\frac{\partial}{\partial t} \rho_f(\mathbf{r}, t) + \nabla \cdot \mathbf{J}_f(\mathbf{r}, t) = 0, \quad (2.1.2)$$

¹Maxwell's equations is written in SI units here. This convention will be adapted throughout the thesis.

where $\mu = \{\text{f, ind, ext}\}$ indicates its appliance in each individual case. Charge conservation is expressed through the continuity equation, and is therefore incorporated implicitly in Maxwell's equation. Two constitutive relations encapsulate the relationship between the fundamental physical fields, \mathbf{E} and \mathbf{H} , and the vectors, \mathbf{D} and \mathbf{B} . These relations take a simple form in the limiting case of a linear, uniform, non-magnetic and isotropic media

$$\mathbf{D}(\mathbf{r}, t) = \epsilon_0 \mathbf{E}(\mathbf{r}, t), \quad (2.1.3)$$

$$\mathbf{B}(\mathbf{r}, t) = \mu_0 \mathbf{H}(\mathbf{r}, t), \quad (2.1.4)$$

where ϵ_0 and μ_0 stands for the electric permittivity and the magnetic permeability of vacuum, respectively. A third constitutive relation becomes important in the case of a conducting material, which is Ohm's law

$$\mathbf{J}_{\text{ind}}(\mathbf{r}, t) = \sigma \mathbf{E}(\mathbf{r}, t), \quad (2.1.5)$$

where σ , denoting the conductivity, generally takes the form of a second-rank tensor in the case of anisotropic mediums. The linear relationships in Eq (2.1.3) and (2.1.5) can be written in a more general manner [8]

$$\mathbf{D}(\mathbf{r}, t) = \epsilon_0 \int \epsilon(\mathbf{r} - \mathbf{r}', t - t') \mathbf{E}(\mathbf{r}', t') d\mathbf{r}' dt', \quad (2.1.6)$$

$$\mathbf{J}_{\text{ind}}(\mathbf{r}, t) = \int \sigma(\mathbf{r} - \mathbf{r}', t - t') \mathbf{E}(\mathbf{r}', t') d\mathbf{r}' dt', \quad (2.1.7)$$

where ϵ and σ expresses the bound-response dielectric function and free-carrier conductivity, respectively, and \mathbf{D} and \mathbf{J}_{ind} depends on the value of \mathbf{E} at all times t' and all locations \mathbf{r}' . In writing of equation (2.1.6) and (2.1.7) it is implicitly assumed that $t' > t$ for both the dielectric function and the conductivity, in order to preserve causality. These general versions of the constitutive relations account for both temporal and spacial dispersion, thus giving a non-local description of the response.

Translational invariance have been assumed in the relations (2.1.6) and (2.1.7), so that only the difference in space is of importance. This assumption enables a specially simple form after a Fourier transformation in space and time², which leads to³

²The forward and backward Fourier transformation will be defined as

$$\tilde{f}(k_x, k_y, k_z, \omega) = \frac{1}{(2\pi)^4} \iiint f(x, y, z, t) e^{i(-k_x x - k_y y - k_z z + \omega t)} dx dy dz dt,$$

and

$$f(x, y, z, t) = \iiint \tilde{f}(k_x, k_y, k_z, \omega) e^{i(k_x x + k_y y + k_z z - \omega t)} dk_x dk_y dk_z d\omega,$$

respectively.

³This is derived using the convolution theorem, which states that Fourier transform of convolution in one domain (space or time) equals point-wise multiplication in the other (momentum or frequency), i.e $\mathcal{F}(f * g) = \mathcal{F}(f) \cdot \mathcal{F}(g)$, where \mathcal{F} denotes forward Fourier transform operator.

$$\mathbf{D}(\mathbf{k}, \omega) = \epsilon_0 \epsilon(\mathbf{k}, \omega) \mathbf{E}(\mathbf{k}, \omega), \quad (2.1.8)$$

$$\mathbf{J}(\mathbf{k}, \omega) = \sigma(\mathbf{k}, \omega) \mathbf{E}(\mathbf{k}, \omega) \quad (2.1.9)$$

The discussion so far has treated the material response due to free and bound charges separately through σ in \mathbf{J}_{ind} and $\epsilon \equiv \epsilon_b$ in \mathbf{D} , respectively. However, it is usually preferred to combine both of these contributions into a single dielectric function in plasmonics. One way to realize this function is to first write the frequency-domain version of Eq. (2.1.1d) ($\partial_t \rightarrow -i\omega$), and then to expand \mathbf{J}_f into its induced and external parts

$$\nabla \times \mathbf{H}(\mathbf{r}, \omega) = \mathbf{J}_{\text{ext}}(\mathbf{r}, \omega) - i\omega \tilde{\mathbf{D}}(\mathbf{r}, \omega), \quad (2.1.10)$$

where $\tilde{\mathbf{D}}(\mathbf{r}, \omega) = \mathbf{D}(\mathbf{r}, \omega) + \frac{i}{\omega} \mathbf{J}_{\text{ind}}(\mathbf{r}, \omega)$ describes the total dielectric function through $\tilde{\mathbf{D}}(\mathbf{r}, \omega) \equiv \epsilon_0 \int \epsilon(\mathbf{r}, \mathbf{r}'; \omega) \mathbf{E}(\mathbf{r}', \omega) d\mathbf{r}'$, leading to

$$\epsilon(\mathbf{r}, \mathbf{r}'; \omega) = \epsilon_b(\mathbf{r}, \mathbf{r}'; \omega) + i \frac{\sigma(\mathbf{r}, \mathbf{r}'; \omega)}{\omega \epsilon_0}. \quad (2.1.11)$$

This modified version of the electric displacement satisfies Maxwell's equations (2.1.1) upon replacing $\rho_f \rightarrow \rho_{\text{ext}}$, $\mathbf{J}_f \rightarrow \mathbf{J}_{\text{ext}}$ and $\mathbf{D} \rightarrow \tilde{\mathbf{D}}$

$$\nabla \cdot \tilde{\mathbf{D}}(\mathbf{r}, \omega) = \rho_{\text{ext}}(\mathbf{r}, \omega), \quad (2.1.12a)$$

$$\nabla \cdot \mathbf{B}(\mathbf{r}, \omega) = 0, \quad (2.1.12b)$$

$$\nabla \times \mathbf{E}(\mathbf{r}, \omega) = i\omega \mathbf{B}(\mathbf{r}, \omega), \quad (2.1.12c)$$

$$\nabla \times \mathbf{H}(\mathbf{r}, \omega) = -i\omega \tilde{\mathbf{D}}(\mathbf{r}, \omega) + \mathbf{J}_{\text{ext}}(\mathbf{r}, \omega). \quad (2.1.12d)$$

Consequently one can exploit the advantages of having all the induced effects in the system contained into a single field, $\tilde{\mathbf{D}}$, as opposed to describing the induced quantities via two fields, as in Eq. (2.1.1). For instance, using Eq. (2.1.12) means that only $\tilde{\mathbf{D}}$ and the corresponding dielectric function ϵ_b needs to be considered when no external charges or currents is present.

Finally it is worth mentioning that appropriate curl identities can be used together with the curl equations of Maxwell in order to derive the Helmholtz equation, which in the absence of free charges and currents (i.e $\mathbf{J}_f = \rho_f = 0$) reads [4]

$$\left(\nabla^2 - \frac{1}{v^2} \frac{\partial^2}{\partial t^2} \right) \mathbf{E}(\mathbf{r}, t) = 0, \quad (2.1.13)$$

where an identical relation holds for the the magnetic field, and $v = \frac{c}{\sqrt{\epsilon}}$. This equation describes the propagation of electromagnetic waves through a medium with relative permittivity ϵ .

2.1.2 The local-response approximation

Although the constitutive relations defined in the previous section presents a clean and general formulation, this picture can be cumbersome to use in practice. The non-local dielectric function $\epsilon(\mathbf{r}, \mathbf{r}'; \omega)$, which depends on all locations, demand specification of seven coordinates and more often than not is unknown, lead to obvious difficulties. This obstacle can be overcome by the introduction of the local-response approximation (LRA), which ignores the non-local response, meaning that the response functions is determined solely in terms of the frequency, i.e. $\epsilon(\omega)$ and $\sigma(\omega)$. Thus the LRA simplifies the constitutive relations to

$$\mathbf{D} = \epsilon_0 \epsilon_{\text{LRA}}(\omega) \mathbf{E}(\mathbf{r}, \omega), \quad (2.1.14)$$

and

$$\mathbf{J} = \sigma_{\text{LRA}}(\omega) \mathbf{E}(\mathbf{r}, \omega), \quad (2.1.15)$$

where $\epsilon_{\text{LRA}} \equiv \epsilon(\omega)$ and $\sigma_{\text{LRA}} \equiv \sigma(\omega)$ will be adopted throughout the rest of the thesis. The LRA is valid as long as the excitation wavevector is much smaller than the Fermi momentum of the electrons, which will be satisfied in all the considered plasmonic systems in this thesis.

2.1.3 Boundary conditions at interfaces

All the electromagnetic fields and material properties discussed so far have been under the assumption of a single homogeneous medium. This medium is now subdivided into two parts, separated by an arbitrary interface. Discontinuity of Maxwell's equation and the constitutive relations arises at this interface, although they still hold true in each of the media. Introduction of appropriate boundary conditions relate the fields at each side of the interface. The boundary conditions is derived from the integral form of Maxwell's equations together with the divergence and Stoke's theorem [8], yielding

$$\hat{\mathbf{n}} \cdot (\mathbf{D}_1 - \mathbf{D}_2) = \sigma_s, \quad (2.1.16a)$$

$$\hat{\mathbf{n}} \cdot (\mathbf{B}_1 - \mathbf{B}_2) = 0, \quad (2.1.16b)$$

$$\hat{\mathbf{n}} \times (\mathbf{B}_1 - \mathbf{B}_2) = \mu_0 \mathbf{J}_s, \quad (2.1.16c)$$

$$\hat{\mathbf{n}} \times (\mathbf{E}_1 - \mathbf{E}_2) = 0. \quad (2.1.16d)$$

Equation (2.1.16a) and (2.1.16b) represents the boundary condition normal to the interface, while (2.1.16c) and (2.1.16d) represents the tangential ones. The subscripts refers to the two half-spaces and $\hat{\mathbf{n}}$ denotes the normal unit vector, pointing from medium 2 into medium 1. The quantities σ_s and \mathbf{J}_s expresses, respectively, the possible existence of a surface charge and surface current density, which naturally satisfies the two-dimensional version of the continuity equation, $\nabla \cdot \mathbf{J}_s + \partial_t \rho_s = 0$.

2.2 The Drude model

The optical behaviour of metals can be described by a plasma model, called the Drude model [9], at which the electrons are modelled to move freely among fixed positive ion cores (comprising both the nucleus and the tightly bound electrons). The motion of the electrons, exposed to an external electric field $\mathbf{E}(t) = \mathbf{E}_0 e^{-i\omega t}$, can in this model be described classically through Newton's second law, which takes the form [10]

$$\frac{d}{dt}\mathbf{p}(t) = -e\mathbf{E}(t) - \gamma\mathbf{p}(t), \quad (2.2.1)$$

where e is the elementary charge, \mathbf{p} the average momentum of the electrons and γ is the scattering rate given by the inverse of the relaxation time τ , which in turn is defined as the average time between collisions of the free electrons with the immobile ions. Taking the time dependence of $\mathbf{p}(t)$ to be the same as for the external field $\mathbf{E}(t)$, the solution to equation (2.2.1) becomes

$$\mathbf{p}(t) = \frac{e\mathbf{E}(t)}{i\omega - \gamma}. \quad (2.2.2)$$

The induced current density arising from n_e electrons per unit volume moving with net velocity \mathbf{v} , is $\mathbf{J} = -en_e\mathbf{v}$. Writing the net velocity in terms of the average momentum, and then substituting Eq. (2.2.2) into this relation yields

$$\mathbf{J} = -\frac{en_e\mathbf{p}}{m} = \frac{e^2n_e}{m} \frac{\mathbf{E}(t)}{\gamma - i\omega} \quad (2.2.3)$$

The expression for the optical conductivity can now be found by comparing this current density with the constitutive relation (2.1.5), which leads to

$$\sigma(\omega) = \frac{e^2n_e}{m} \frac{1}{\gamma - i\omega} \quad (2.2.4)$$

Substituting this conductivity into the previously derived dielectric function in Eq. (2.1.11) yields [11, 10]

$$\boxed{\epsilon(\omega) = \epsilon_b(\omega) - \frac{\omega_p^2}{\omega^2 + i\gamma\omega}}, \quad (2.2.5)$$

where $\omega_p^2 = \frac{e^2n_e}{m\epsilon_0}$ denotes the *plasma frequency* of the free electron gas. In the case of the free-electron model, we have that $\epsilon_b = 1$. However, for conventional plasmonic metals like

Au, Ag and Cu, a correction to this model is needed due to filled d-bands producing a highly polarized background. This correction is introduced by a higher value of ϵ_b , which usually lies in the interval $1 \leq \epsilon_b \leq 10$.

Albeit its simple nature, this model is able to describe the essential properties of metals in the infrared regime of the electromagnetic spectrum. The reason lies in the fact that the frequency dependence of the optical response is highly influenced by intraband transitions in this part of the spectrum, thus yielding relatively good predictions. However, the great predictions of the model falls apart considerably for the noble metals in the visible and ultraviolet regions, where interband transitions, among other things, starts to dominate. This does indeed not come as a surprise, since the model at hand only takes into account a single band.

The behaviour mentioned above is illustrated in Fig 2.1, which compare experimental values of the dielectric function (taken from Johnson and Christy [12]) with the Drude model in the case of gold and silver. The blue and red dashed curve (circles) represents, respectively, the real and imaginary part of the Drude model dielectric function (experimentally determined dielectric function). This figure clearly shows the previously discussed frequency dependent accuracy of the Drude model. The model fits the data well at at energies smaller than ≈ 3 eV, while significant deviations starts to occur above this energy.

The presence of interband transitions can be included to the model, by the addition of a resonant term to the original equation of motion, whose resonant frequency represents the transition energy between the bands. This extra contribution leads to a dielectric function, which also consists of a Lorentz-oscillator term, while keeping the classical picture intact. It is worth mentioning, that one of the main advantages of the Drude model lies in its accurate prediction despite its great simplicity. One needs to rely on a quantum mechanical formulation in order to get a more rigorous description of the optical properties of the metals [13].

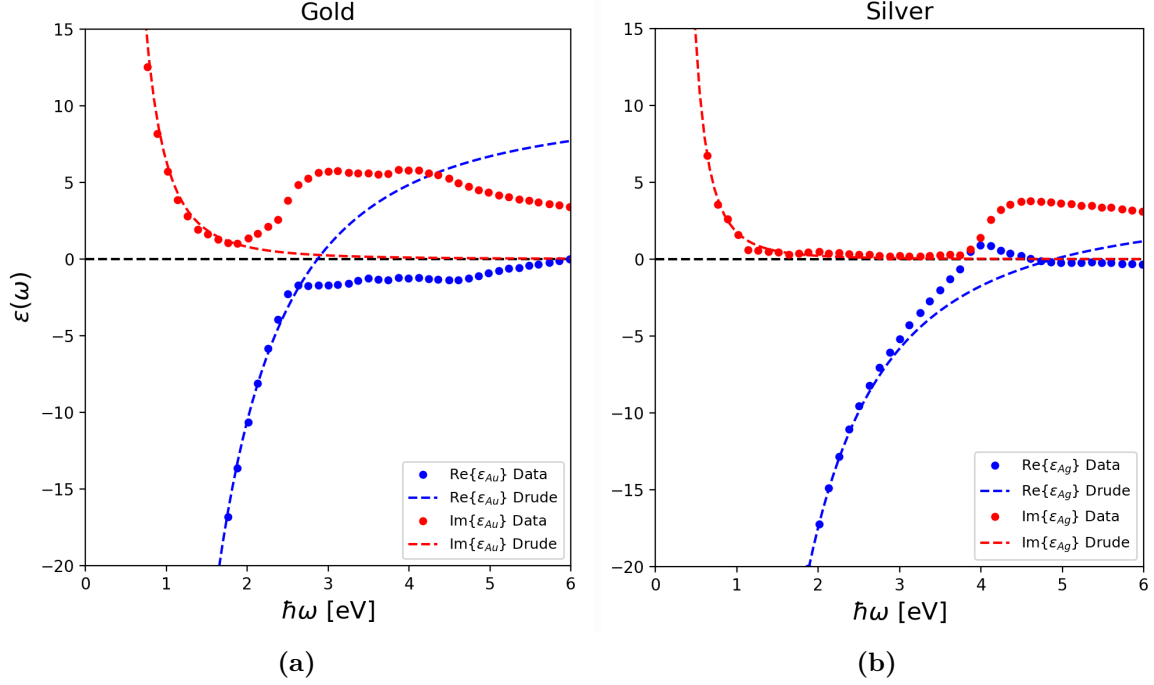


Figure 2.1: Dielectric function of two frequently used noble metals in the plasmonic community: gold (left figure) and silver (right figure). The filled circles represents experimentally obtained values taken from Johnson and Christy [12]. The dashed lines show the corresponding Drude model, which for gold have been obtained with the parameters: $\epsilon_b = 10.0$, $\hbar\omega_p = 9.08$ eV and $\hbar\gamma = 78$ meV, while the following parameters were used for silver: $\epsilon_b = 3.5$, $\hbar\omega_p = 9.16$ eV and $\hbar\gamma = 21$ meV, taken from [14]

Chapter 3

Surface Plasmon Polaritons at Metal/Dielectric Interfaces

Now that the fundamental theory of interaction between electromagnetic fields and matter in the framework of Maxwell's equations have been established, we are in possession of the underlying building blocks necessary to discuss the field of classical plasmonics. Equipped with Maxwell's equations, the boundary conditions and the relevant local response function, the plasmonic excitations can be perfectly characterized in the regime of classical electromagnetism.

The intention of the following chapter is to present the essential concepts of the classical plasmonic theory. These concepts are of crucial importance, and will constitute the foundation on which the upcoming chapters are built.

3.1 Single Dielectric-Metal Interface

The simplest system capable of sustaining surface plasmon-polaritons (SPPs) is that of a single flat dielectric-metal interface. For the sake of simplicity, both media is assumed to be isotropic and semi-infinite. The dielectric have been chosen to occupy the space defined by $z < 0$, while the metal is located at $z > 0$, which is schematically illustrated in Fig 3.1

The dielectric nature of the two mediums at hand is fundamentally different from each other. The dielectric medium is described by a positive and real valued dielectric constant, ϵ_1 , while the properties of the metal is characterized by a frequency-dependent complex dielectric function, $\epsilon_2(\omega)$. It suffices, at this stage, to use the dielectric function (2.2.5) derived in section (2.2) from the Drude model with $\epsilon_b(\omega) = 1$ to describe $\epsilon_2(\omega)$ ¹.

¹This approximation is valid as long as the energy of the incoming light is not sufficient to cause interband transitions, i.e the infrared regime for the commonly used noble metals in plasmonics.



Figure 3.1: Illustration of the single dielectric-Metal Interface geometry with the corresponding axis convention, where the interface separating the two media is located at $z = 0$. The y -axis points into the paper and the system is assumed to be uniform along this axis.

3.1.1 Dispersion relation

Examination of propagating solutions to Maxwell's equations is now carried out in the form of transverse magnetic (TM) (or p-polarized) waves. In this case the fields can be written as

$$\mathbf{E}_j(\mathbf{r}, t) = (E_{j,x}\hat{\mathbf{x}} + E_{j,z}\hat{\mathbf{z}})e^{-\kappa_j|z|}e^{i(qx-\omega t)}, \quad (3.1.1a)$$

$$\mathbf{B}_j(\mathbf{r}, t) = B_{j,y}\hat{\mathbf{y}}e^{-\kappa_j|z|}e^{i(qx-\omega t)}, \quad (3.1.1b)$$

where $j = 1, 2$ denotes the media shown in Fig 3.1, q identifies the propagation constant (taken to point along the x -axis in the present case), κ_j describes an exponential decay of the fields along the z -axis and the usual harmonic time-dependence $e^{-i\omega t}$ have been assumed. Inserting these fields into Maxwell's equations (2.1.12c) and (2.1.12d) leads to the following field amplitude relations

$$B_{j,y} = -\frac{\omega\epsilon_j}{c^2q}E_{j,z}, \quad (3.1.2a)$$

$$B_{j,y} = -is_j\frac{\omega\epsilon_j}{c^2\kappa_j}E_{j,x}, \quad (3.1.2b)$$

$$E_{j,x} = -is_j\frac{\kappa_j}{q}E_{j,z}, \quad (3.1.2c)$$

and

$$\kappa_j^2 = q^2 - \epsilon_j\frac{\omega^2}{c^2} \quad (3.1.3)$$

where s_j , defined as $s_j = \delta_{j2} - \delta_{j1}$, is ensuring field confinement to the interface. The last step is to relate the fields on each side of the interface. This is done by invoking the tangential boundary condition of Maxwell's equations (2.1.16c) and (2.1.16d), which yields

$$E_{1,x} = E_{2,x}, \quad (3.1.4)$$

$$B_{1,y} = B_{2,y}. \quad (3.1.5)$$

Inserting the results from Eq. (3.1.2) in these boundary conditions leads to the following equation [11]

$$\boxed{\frac{\epsilon_1}{\kappa_1(q, \omega)} + \frac{\epsilon_2(\omega)}{\kappa(q, \omega)} = 0}, \quad (3.1.6)$$

which establishes the condition for existence of a SPP dispersion relation. It is seen in Eq. (3.1.1) that one must have $\text{Re}\{\kappa_{1,2}\} > 0$ if the fields is to be confined to the interface. Therefore if $\epsilon_1 > 0$, which is common for most dielectric mediums, then one must have that $\text{Re}\{\epsilon_2(\omega)\} < 0$ in order to satisfy the SPP condition (3.1.6). This means that excitation of SPPs only takes place at interfaces between two media with opposite sign of the real part of their dielectric permittivities.

It is possible to achieve an expression relating the SPP wavevector to the frequency by insertion of Eq. (3.1.3) in Eq. (3.1.6) [11]

$$\boxed{q_{SPP} = \frac{\omega}{c} \sqrt{\frac{\epsilon_1 \epsilon_2(\omega)}{\epsilon_1 + \epsilon_2(\omega)}}}. \quad (3.1.7)$$

This dispersion relation for the single dielectric-metal interface SPP can be analyzed in two separate cases, namely with and without the presence of damping.

Without Loss ($\gamma = 0$):

The Drude dielectric function in the case of zero attenuation is simply found by setting $\gamma = 0$ in Eq. (2.2.5), which leads to

$$\epsilon_2(\omega) = 1 - \frac{\omega_p^2}{\omega^2}. \quad (3.1.8)$$

The SPP dispersion relation obtained by insertion of this dielectric function into Eq. (3.1.7) is represented by the blue continuous curve in panel (a) of Fig. 3.2, which depicts the bound excitations confined to the interface. The bound nature of SPPs dictates a real valued q and κ_j , hence the dispersion relation must be located to the right of the light line (red dashed line). Accordingly, it is not possible to excite SPPs directly by light, instead alternative

methods has to be invoked, which are suited for coupling light to the surface plasmons. Taking the limit for small wavevectors, where the dispersion curve approaches the light line, it is seen that $\kappa_1 \ll 1$. Consequently the electromagnetic field is not well confined to the interface and will reach far into the dielectric medium. Taking the opposite limit, where $q \rightarrow \infty$, it is observed in Fig. 3.2a that the SPP dispersion asymptotically approaches a specific frequency. This frequency is dubbed the *surface plasmon frequency* and is derived by setting $\epsilon_1 + \epsilon_2(\omega) = 0$ in Eq. (3.1.7), leading to [4]

$$\omega_{sp} = \frac{\omega_p}{\sqrt{1 + \epsilon_1}}. \quad (3.1.9)$$

Although this thesis will mainly be concerned with SPPs, it is worth noting that a second branch appears in the lossless case for frequencies above ω_p (green continuous curve in Fig. 3.2a). This branch represents the volume plasmon polaritons (VPPs) and characterizes collective oscillations of the free electrons in the bulk material². The metals become transparent to the incoming light in this upper region, since $\omega > \omega_p$, and is therefore referred to as radiative modes.

With loss ($\gamma \neq 0$):

All metals is in reality exposed to some degree of losses. These losses come in a variety of different forms, but all have the same attenuating effect on the propagating SPPs. The Drude model encapsulate all of these contributions into a single parameter γ (see Eq. (2.2.5)). This simple approach fits the description of the optical response of the metals rather well at low frequencies, but breaks down once interband transitions become significant.

The lossy SPP dispersion relation in the framework of the Drude model is depicted in Fig 3.2b with the corresponding light line. One of the most noteworthy aspect of this dispersion relation is the limited value of $\text{Re}\{q\}$, as opposed to the possibility of an infinite valued wavevector in the lossless case. The consequence of this limitation is a lower restriction on the SPP wavelength, given by $\lambda_{SPP} = 2\pi/\text{Re}\{q\}$, which in turn leads to less confinement to the interface. Finally notice the emergence of modes in the region bounded by ω_{sp} and ω_p , which is in contrast to the lossless modes.

²The VPP dispersion relation is general given by $q(\omega) = \sqrt{\epsilon_2(\omega)} \frac{\omega}{c}$, which without the presence of losses can be reduced to $\omega(q) = \sqrt{\omega_p^2 + q^2 c^2}$.

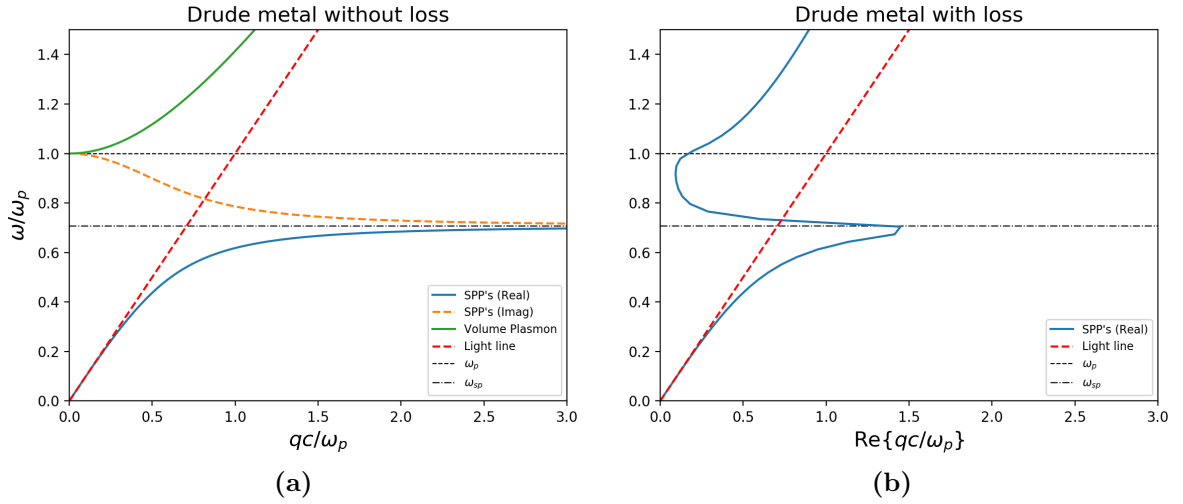


Figure 3.2: Dispersion relation of surface plasmon polariton in the a single dielectric-metal interface. The metal have been modelled in the framework of the Drude model and is placed in air ($\epsilon_1 = 1$). **(a)** Drude metal without damping ($\gamma = 0$). **(b)** Drude metal taking damping into account ($\gamma = \frac{\omega_p}{20}$).

3.1.2 Propagation length and field confinement

The complex-valued dielectric function arising from the existence of damping mechanisms in the system naturally leads to a corresponding complex wavevector $q = q' + iq''$. The damping in the x-direction of the SPP will therefore be described by an exponentially decaying term of the form $\exp(-q''x)$. The real and imaginary part of the wavevector is given by [11]

$$q' = \frac{\omega}{c} \sqrt{\frac{\epsilon_1 \epsilon_2'}{\epsilon_1 + \epsilon_2'}}, \quad (3.1.10a)$$

$$q'' = \frac{1}{2} \frac{\omega}{c} \left(\frac{\epsilon_1 + \epsilon_2'}{\epsilon_1 \epsilon_2'} \right)^{3/2} \frac{(\epsilon_2'')^2}{\epsilon_2'}. \quad (3.1.10b)$$

The intensity of the electromagnetic field falls off as $\exp(-2q''x)$, the characteristic propagation length is therefore given by [11]

$$L_{SPP} = \frac{1}{2q''}, \quad (3.1.11)$$

which defines the length, where the SPP intensity has been decreased by $1/e$. The propagation length is illustrated in Fig. 3.3a, where the blue and red curve corresponds to an

air-silver and silica-silver interface respectively. One aspect worth noting from this plot is the big variety of propagation lengths in the given wavelength interval, ranging from a few to 100 micrometers in the visible wavelengths up to even 1000 micrometers in the infrared region. Further note, that the minimum in the propagation length (approximately at 400nm for the air-silica interface) corresponds to the plasmon frequency ω_{sp} , which is due to the previously stated definition of this quantity.

Among the many interesting properties of SPPs, one of the most prominent features is the degree of light confinement to a dielectric-metal interface. This confinement of light, perpendicular to the interface, is usually on scales below the diffraction limit, which in the field of optics sets a theoretical limit to the separation of two airy discs [15]. The intensity of the electromagnetic fields in the perpendicular direction decrease exponentially as $\exp(-\kappa_j|z|)$, thus the field confinement can, as in the case of the characteristic propagation length, be described by the following quantity [11]

$$\zeta_j = \frac{1}{\text{Re}\{\kappa_j\}}, \quad (3.1.12)$$

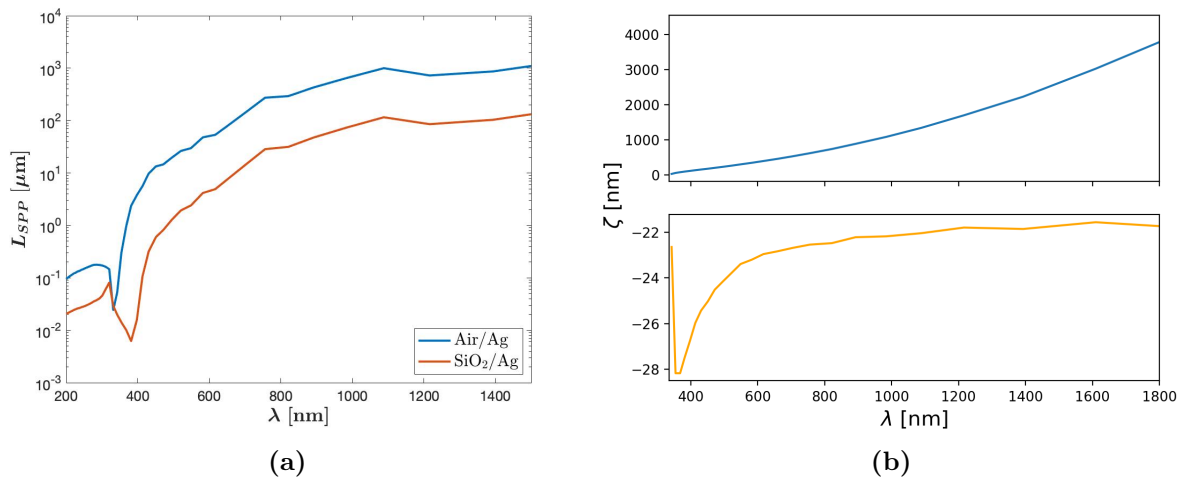


Figure 3.3: (a) Experimentally determined propagation length of silver submerged in air (blue curve) and SiO₂ (red curve). The calculation was done from $L_{SPP} = (2q'')^{-1}$ and with data from Johnson and Christy [12]. (b) Penetration depth of SPPs into air (upper subfigure) and silve (lower subfigure), obtained from Johnson and Christy dielectric data [12]

dubbed the penetration depth. This quantity have been illustrated as a function of the wavelength in the case of a air-silver interface in Fig. 3.3b. It becomes apparent from this plot that the penetration depth is strikingly different in the two media. The behaviour in

the dielectric (air) is steadily increasing as a function of the wavelength of the incoming light, consequently the field confinement is suppressed. The metal (silver), on the other hand, exhibits a rather constant nature for frequencies below ω_{sp} and is observed to be several orders of magnitude smaller as compared to the dielectric.

It is now clear that an inevitable trade-off exists in plasmonics regarding SPPs. Large propagation lengths comes at a cost, which is smaller field confinement and vice versa. Setting up an experiment involving SPPs therefore typically lead to some kind of compromise for the quantities discussed above, since one cannot have both.

3.2 Double Dielectric-Metal Interface

The previous section treated the most simple system capable of sustaining SPPs. However, the material discussed in that section can be further developed into systems comprising two (and in principle more) planar interfaces between dielectrics and metals. The dispersion relation will be derived and visualized in this section for both the metal-dielectric-metal (MDM) and the dielectric-metal-dielectric (DMD) structures.

The spectrum of SPPs in planar double-interfaces are derived in much the same fashion as for the single interface system. The situation at hand is schematically illustrated in figure 3.4.

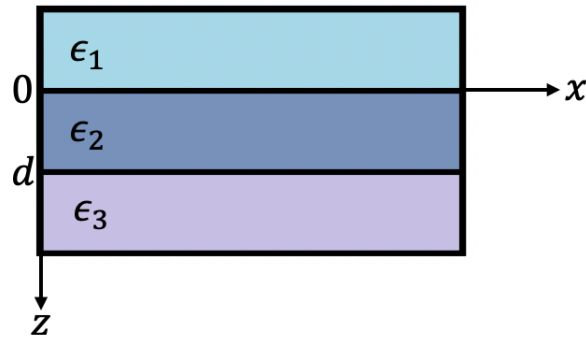


Figure 3.4: Schematic illustration of a three-layered system, able to sustain propagating SPPs. The system could be that of a symmetric MDM structure, meaning that $\epsilon_2 \equiv \epsilon_2(\omega)$, or that of a symmetric MDM, at which $\epsilon_1 \equiv \epsilon_1(\omega)$ and $\epsilon_3 \equiv \epsilon_3(\omega)$. The separation between the two cladding media is denoted d and the cladding media themselves is assumed to be semi-infinite.

The difference between the case of single and double interfaces, is that the double interface geometry permits a superposition of exponentially growing and decaying fields in the middle medium, ϵ_2 . When the spacing, d , separating medium one and three is sufficiently large, the three-layered system can be regarded as two isolated single interface structures. The interesting physics, however, emerges when this separation is decreased to a distance, at

which communication between the electromagnetic fields is possible. This "communication" leads to new hybridized modes with different properties.

3.2.1 Dispersion relation

The spectral properties will, just as for the single interface, be derived in the form of TM surface waves, and the electromagnetic fields in medium one and three is therefore given by Eq. (3.1.1). Accordingly the results in Eq. (3.1.2) and (3.1.3) still holds in these two media. Medium two (where $0 < z < d$), on the other hand, should, as mentioned earlier, be described as a superposition of exponentially growing and decaying waves, taking the form

$$\mathbf{E}_2(\mathbf{r}, t) = \left[\left(E_{2,x}^{(+)} \hat{\mathbf{x}} + E_{2,z}^{(+)} \hat{\mathbf{z}} \right) e^{\kappa_2 z} + \left(E_{2,x}^{(-)} \hat{\mathbf{x}} + E_{2,z}^{(-)} \hat{\mathbf{z}} \right) e^{-\kappa_2 z} \right] e^{i(qx - \omega t)}, \quad (3.2.1a)$$

$$\mathbf{B}_2(\mathbf{r}, t) = \left(B_{2,y}^{(+)} e^{\kappa_2 z} + B_{2,y}^{(-)} e^{-\kappa_2 z} \right) \hat{\mathbf{y}} e^{i(qx - \omega t)}. \quad (3.2.1b)$$

Inserting these fields into Maxwell's equations results in the following expressions

$$B_{2,y}^{(+)} = -\frac{\omega \epsilon_2}{c^2 q} E_{2,z}^{(+)}, \quad (3.2.2a)$$

$$B_{2,y}^{(+)} = i \frac{\omega \epsilon_2}{c^2 \kappa_2} E_{2,x}^{(+)}, \quad (3.2.2b)$$

$$B_{2,y}^{(-)} = -\frac{\omega \epsilon_2}{c^2 q} E_{2,z}^{(-)}, \quad (3.2.2c)$$

$$B_{2,y}^{(-)} = -i \frac{\omega \epsilon_2}{c^2 \kappa_2} E_{2,x}^{(-)}, \quad (3.2.2d)$$

$$\kappa_2 = \sqrt{q^2 - \epsilon_2 \omega^2 / c^2} \quad (3.2.3)$$

which relates the amplitude of the magnetic field with the associated amplitude of the electric field. Two sets of boundary conditions needs to be exploited, in order to derive the dispersion relation, because of the existence of two interfaces. The first condition at $z = 0$ for the interface separating medium one and two reads

$$E_{1,x} = E_{2,x}^{(+)} + E_{2,x}^{(-)}, \quad (3.2.4)$$

$$B_{1,y} = B_{2,y}^{(+)} + B_{2,y}^{(-)}, \quad (3.2.5)$$

while the second condition at $z = d$ for the interface between medium two and three is given by

$$E_{2,x}^{(+)} e^{\kappa_2 d} + E_{2,x}^{(-)} e^{-\kappa_2 d} = E_{3,x} e^{-\kappa_3 d}, \quad (3.2.6)$$

$$B_{2,y}^{(+)} e^{\kappa_2 d} + B_{2,y}^{(-)} e^{-\kappa_2 d} = B_{3,y} e^{-\kappa_3 d}. \quad (3.2.7)$$

It is obvious at this point, that finding the spectral properties in the double layer system is more involved as compared to the single interface. For instance, finding a non-trivial solution for the electric field now involves four equations, as is the case for the magnetic field. Fortunately Eq. (3.1.1) and (3.2.2) can be collected into a single linear matrix equation

$$\begin{bmatrix} -1 & 1 & 1 & 0 \\ -\frac{\epsilon_1}{\kappa_1} & \frac{\epsilon_2}{\kappa_2} & -\frac{\epsilon_2}{\kappa_2} & 0 \\ 0 & e^{\kappa_2 d} & e^{-\kappa_2 d} & -e^{-\kappa_3 d} \\ 0 & \frac{\epsilon_2}{\kappa_2} e^{\kappa_2 d} & -\frac{\epsilon_2}{\kappa_2} e^{-\kappa_2 d} & \frac{\epsilon_3}{\kappa_3} e^{-\kappa_3 d} \end{bmatrix} \begin{bmatrix} E_{1,x} \\ E_{2,x}^{(+)} \\ E_{2,x}^{(-)} \\ E_{3,x} \end{bmatrix} = 0. \quad (3.2.8)$$

The non-trivial solution is then calculated by setting the determinant of Eq. (3.2.8) equal to zero, which leads to the following condition [11]

$$\left(1 + \frac{\epsilon_2 \kappa_1}{\epsilon_1 \kappa_2}\right) \left(1 + \frac{\epsilon_2 \kappa_3}{\epsilon_3 \kappa_2}\right) = \left(1 - \frac{\epsilon_2 \kappa_1}{\epsilon_1 \kappa_2}\right) \left(1 - \frac{\epsilon_2 \kappa_3}{\epsilon_3 \kappa_2}\right) e^{-2\kappa_2 d}. \quad (3.2.9)$$

It is implicit in Eq. (3.2.9) that κ_j is a function of both the frequency and the wavevector $\kappa_j(q, \omega)$ and that the dielectric function in the metallic media depends on the frequency $\epsilon(\omega)$ ³. Taking the limit $d \rightarrow \infty$, meaning that the separation of medium one and three becomes large, this equation reduces to the following two conditions

$$\frac{\epsilon_1}{\epsilon_2} + \frac{\kappa_1}{\kappa_2} = 0 \quad , \quad \frac{\epsilon_3}{\epsilon_2} + \frac{\kappa_3}{\kappa_2} = 0. \quad (3.2.10)$$

These conditions can be identified with two isolated single interface dispersion relations. However, this should not come as a surprise, since the fields is unable to interact with one another in medium two if the spacing, d , is too large.

A special case worth discussing, is that of a symmetric MDM or DMD geometry, where medium one and three is made of the exact same material, i.e $\epsilon_1 = \epsilon_3$ and $\kappa_1 = \kappa_3$. These new conditions simplifies the dispersion relation and leads to two distinct modes given by [11]

$$\omega_+ : \tanh\left(\frac{\kappa_2 d}{2}\right) = -\frac{\epsilon_2 \kappa_1}{\epsilon_1 \kappa_2}, \quad (3.2.11)$$

$$\omega_- : \coth\left(\frac{\kappa_2 d}{2}\right) = -\frac{\epsilon_2 \kappa_1}{\epsilon_1 \kappa_2}. \quad (3.2.12)$$

³The dielectric function of the dielectric medium could, in principle, also depends on the frequency, however the effect from this frequency dependence will be ignored here for the sake of simplicity.

The "+" and "-" subscript in Eq. (3.2.11) and (3.2.12) denotes respectively the high and low-frequency mode.

The behaviour of these hybridized modes in symmetric DMD structures is shown for a variety of different separations, d , in Fig. 3.5a. It is seen that a relatively large thickness of 50 nm (solid blue curve) almost resembles the dispersion relation for the single interface (dot dashed purple curve), which supports the $d = \infty$ limit discussed above. A rather small gap of 5 nm (solid orange curve), on the other hand, differs substantially from the single planar interface, clearly distinguishing the high frequency mode (upper branch) from the low frequency mode (lower branch). This splitting of the modes arises because of the interaction of the fields, which perturbs the system and hence removes the degeneracy in the system. Further notice that the ω_+ mode is able to overcome the surface plasmon frequency, ω_{sp} , if the film is sufficiently thin, as opposed to the single interface, where no propagating solutions existed in the region bounded by ω_{sp} and ω_p . The low frequency mode, on the contrary, does not cross ω_{sp} , regardless of the film thickness. Accordingly this mode has the ability to achieve very large wavevectors, meaning that the SPP wavelength can be exceptionally small.

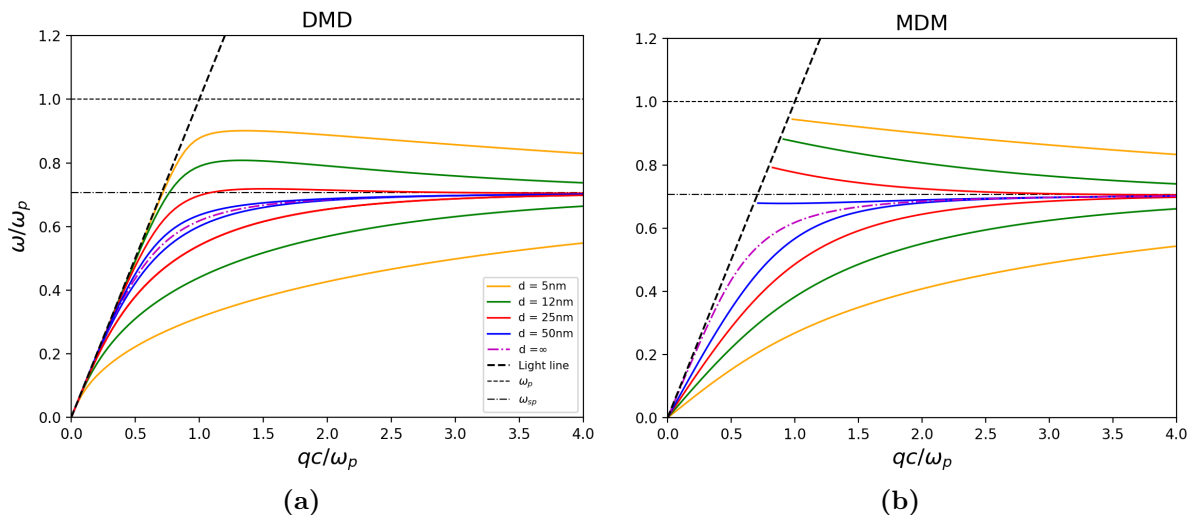


Figure 3.5: (a) Hybridized modes in planar DMD system. (b) Hybridized modes in planar MDM system. The dielectric medium consists of air ($\epsilon_{dielectric} = 1$) and the metal is described by the Drude model without damping ($\gamma = 0$) and $\omega_p = 9.2$ eV.

The dispersion relation for the MDM structure depicted in Fig. 3.5b shows the same dependence on the film thickness as the DMD geometry. One striking difference, however, between these two systems appears near the light line for the high frequency modes, since these modes doesn't go to zero.

This analysis of double interface structures could indeed be further developed in the case of a non-zero damping parameter, γ , in the Drude mode [16]. In accordance with the previous sections, one would expect a maximum value for the wavevector, eventually

bending back and crossing the light line. Looking at the DMD structure, it turns out that the introduction of damping won't influence the two modes in the same way [11]. The propagation length of the high frequency mode increases when the separation decreases, while the low frequency mode shows the opposite behaviour. The high and low frequency mode is, for this reason, often called the long- and short-range surface plasmon-polariton, respectively.

Chapter 4

Optical and Electronic Properties of Graphene

Graphene is a two-dimensional material made of carbon atoms, which are arranged in a hexagonal structure. Graphene was isolated for the first time in 2004 [5] and have, since that day, been gaining a lot of research interest due to some of its exceptional properties; it shows a remarkably large thermal conductivity [6], is stronger than steel and at the same time flexible [17]; The free electrons in graphene behaves as massless Dirac fermions satisfying the relativistic Dirac equation. Graphene has, on behalf of these uncommon features, been called a "*wonder material*".

This chapter will serve to review and discuss the optical and electronic properties of graphene. The knowledge acquired will then constitute the foundation, necessary to describe the optical response of graphene in the upcoming chapters.

4.1 Electronic band structure of graphene

4.1.1 Real and reciprocal space description of graphene

Carbon is element number six in the periodic table and has the following electronic configuration

$$[C] = 1s^2 2s^2 2p^2. \quad (4.1.1)$$

This ground state configuration of the carbon atom is, however, not able to create the amount of bonds required in graphene. The $2s$ orbital therefore fuse with the $2p$ orbitals under the promotion of an electron to the $2p_z$ orbital [18]. The hybridization of the $2s$, $2p_x$ and $2p_y$ orbitals now originate the strong in-plane σ -bonds separated by 120° , while the remaining $2p_z$ electron constitute the weaker out-of-plane π -bond. The π -band can be said to be half-filled, since the $2p_z$ orbital only contains a single electron [7]. It is these electrons that give the characteristic low-energy electronic properties of graphene.

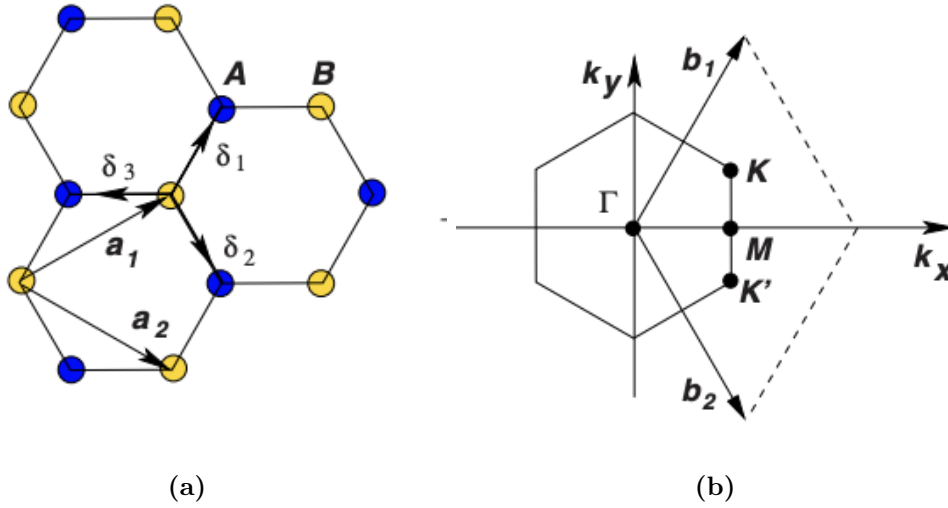


Figure 4.1: Hexagonal structure and the corresponding Brillouin zone of one-atom thick graphene. **(a)** Real space structure of graphene made up of two sublattices A (blue dots) and B (yellow dots). \mathbf{a}_1 and \mathbf{a}_2 denote the primitive lattice vectors and δ_j ($j \in \{1, 2, 3\}$) represents the nearest-neighbour vectors. **(b)** Representation of the space reciprocal to the real space, where \mathbf{b}_1 and \mathbf{b}_2 indicate the primitive reciprocal lattice vectors. The symmetry points in the first Brillouin zone are given by Γ , M , K and K' . The figure has been taken from A. H. C. Neto [7].

The hexagonal structure of graphene in real space is shown in Fig. 4.1a. This structure can equivalently be viewed as a composition of two sublattices, denoted by lattice A and B, where all neighbours to a carbon atom in lattice A always lies in lattice B. The vectors describing this nearest neighbour distance is given by

$$\delta_1 = \frac{a}{2}(1, \sqrt{3}) \quad , \quad \delta_2 = \frac{a}{2}(1, -\sqrt{3}) \quad \text{and} \quad \delta_3 = -a(1, 0), \quad (4.1.2)$$

where $a \simeq 1.42 \text{ \AA}$ is the separation between two carbon atoms in the lattice. These nearest-neighbour vectors turn out to be of crucial importance in the discussion of the tight-binding model. The primitive lattice vectors of real space can be constructed as follows

$$\mathbf{a}_1 = \frac{a}{2}(3, \sqrt{3}) \quad \text{and} \quad \mathbf{a}_2 = \frac{a}{2}(3, -\sqrt{3}). \quad (4.1.3)$$

The associated reciprocal lattice is illustrated in Fig. 4.1b, where the space is now spanned by the reciprocal primitive lattice vectors¹

¹The primitive reciprocal vectors are found through the relation $\mathbf{a}_i \cdot \mathbf{b}_j = 2\pi\delta_{ij}$ known from condensed matter theory [10]

$$\mathbf{b}_1 = \frac{2\pi}{3a}(1, \sqrt{3}) \quad \text{and} \quad \mathbf{b}_2 = \frac{2\pi}{3a}(1, -\sqrt{3}). \quad (4.1.4)$$

Finally the points \mathbf{K} and \mathbf{K}' dubbed the Dirac points, for reasons that will be clarified in the next section, is given by

$$\mathbf{K} = \frac{2\pi}{3a} \left(1, \frac{1}{\sqrt{3}}\right) \quad \text{and} \quad \mathbf{K}' = \frac{2\pi}{3a} \left(1, -\frac{1}{\sqrt{3}}\right). \quad (4.1.5)$$

4.1.2 The tight-binding model

The electronic band structure of a solid reveals a lot of information regarding the possible energy states that electrons take within this material, as well as the forbidden energies, this structure is therefore very desirable to obtain. One of the frequently used methods to calculate the band structure of solids is that of the tight-binding (TB) model [10]. It turns out that graphene follows this trend, where the TB approach have become a common way to describe the properties of this material [7]. The electronic structure could in principle be determined by other and more sophisticated methods, like density functional theory (DFT) for instance. However, the advantage of the TB model lies in its ability to describe the essential structures of the Hamiltonian, even though that the model is of great simplicity. The first theoretical work of graphene, done by Wallace in 1947 [19], was actually done with the TB-model in the attempt to describe the band structure of graphite, which is the 3D version of graphene.

The TB model can be used for many degrees of complexity, which depends on the amount of neighbours taken into account. Graphene is sufficiently described by the nearest neighbour TB model, which consists of a Hamiltonian with only a single hopping parameter, t , although more involved Hamiltonians could be exploited by the introduction of a higher order hopping parameter.

The nearest neighbour TB Hamiltonian for the $2p_z$ electrons originating the π -bonds in graphene is given by [11, 7]

$$H_{TB} = t \sum_{n,m} \{ |A, \mathbf{R}_n\rangle \langle B, \mathbf{R}_n + \boldsymbol{\delta}_m| + \text{H.c.} \}, \quad (4.1.6)$$

where t represents the nearest-neighbour hopping parameter of the electrons, given by $t \approx -2.7\text{eV}$ and H.c. stands for the Hermitian conjugate of the first term. The Wannier state $|A, \mathbf{R}_n\rangle$ describes a carbon atom in sublattice A in the unit cell located at position \mathbf{R}_n . A similar description holds for $\langle B, \mathbf{R}_n + \boldsymbol{\delta}_m|$, that is the Wannier state of a carbon atom in sublattice B located some distance (given by Eq. (4.1.2)) from the carbon atom in sublattice A.

One common way to define the Wannier states is in terms of bloch states [10]

$$|A, \mathbf{R}_n\rangle = \frac{1}{\sqrt{N}} \sum_{\mathbf{k}} e^{-i\mathbf{k}\cdot\mathbf{R}_n} |A, \mathbf{k}\rangle, \quad (4.1.7)$$

$$\langle B, \mathbf{R}_n + \boldsymbol{\delta}_m | = \frac{1}{\sqrt{N}} \sum_{\mathbf{k}} e^{i\mathbf{k}\cdot(\mathbf{R}_n + \boldsymbol{\delta}_m)} \langle B, \mathbf{k} | \quad (4.1.8)$$

where the Bloch states have been written in Fourier representation and N is the total number of unit cells in the system. Introducing Eq. (4.1.7) and (4.1.8) into the TB Hamiltonian (4.1.6) yields

$$H_{TB} = t \sum_{\mathbf{k}} \{ |A, \mathbf{k}\rangle \langle B, \mathbf{k} | \phi(\mathbf{k}) + \text{H.c.} \}, \quad (4.1.9)$$

where the following definition have been used

$$\phi(\mathbf{k}) = \sum_{m=1}^3 e^{i\mathbf{k}\cdot\boldsymbol{\delta}_m}. \quad (4.1.10)$$

The TB Hamiltonian (4.1.9) can be written in an alternative way as $H_{TB} = \sum_{\mathbf{k}} \boldsymbol{\psi}_{\mathbf{k}}^\dagger \mathbf{H}_{\mathbf{k}} \boldsymbol{\psi}_{\mathbf{k}}$, where $\boldsymbol{\psi}_{\mathbf{k}}^\dagger = [|A, \mathbf{k}\rangle, |B, \mathbf{k}\rangle]$ and

$$\mathbf{H}_{\mathbf{k}} = \begin{bmatrix} 0 & t\phi(\mathbf{k}) \\ t\phi^*(\mathbf{k}) & 0 \end{bmatrix}. \quad (4.1.11)$$

The spectrum is now found by calculating the eigenvalues of $\mathbf{H}_{\mathbf{k}}$, which yields [11]

$$E_{\mathbf{k}} = \pm t |\phi(\mathbf{k})| = \pm t \sqrt{3 + 2 \cos(\sqrt{3}k_x a) + 4 \cos\left(\frac{\sqrt{3}}{2}k_x a\right) \cos\left(\frac{3}{2}k_y a\right)}. \quad (4.1.12)$$

The plus sign in Eq. (4.1.12) describes the upper conduction band, while the minus sign refers to the lower valence band. Consequently it is concluded that the spectrum of undoped graphene is particle-hole symmetric. The electronic band structure of graphene is shown in Fig. 4.2a. It becomes apparent in this figure that the two bands touch at six points in the first Brillouin zone, corresponding to the symmetry points \mathbf{K} and \mathbf{K}' . However, each of these six points is shared in between a total of three Brillouin zones, which means that one Brillouin zone has two independent points of this character. The fact that the valence and the conduction band touches each other, and that the density of states (DOS) is very small at this energy classifies graphene as a semi-metal.

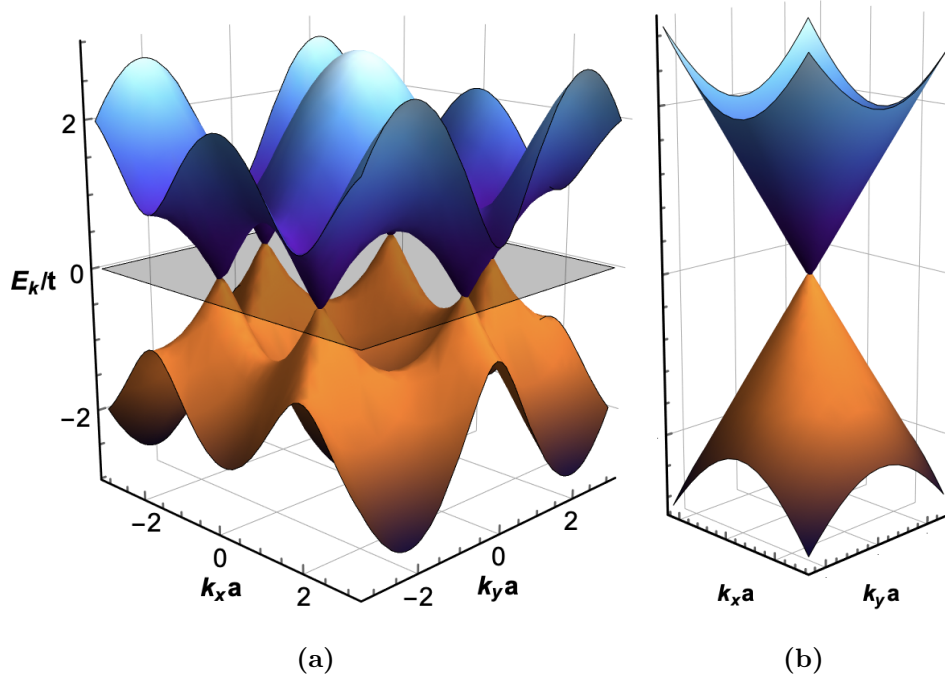


Figure 4.2: Electronic band structure of graphene calculated from the tight-binding model (4.1.12). (a) Valence (lower orange) and conduction (upper blue) band within the first Brillouin zone. These two bands touch each other at six distinct points, called Dirac points, denoted \mathbf{K} and \mathbf{K}' . (b) A close-up on one of the Dirac points, showing the low energy linear behaviour of the spectrum.

4.1.3 Massless Dirac Hamiltonian

The vast majority of interesting features in graphene arises because of its linear low-energy electronic spectrum near \mathbf{K} and \mathbf{K}' . This linearity have been depicted in Fig 4.2b, where a close-up have been performed in the vicinity of a Dirac point (named after the conical shape of the spectrum).

The significance of the Dirac point thus motivates an expansion around \mathbf{K} . Writing a new wavevector $\mathbf{k} = \mathbf{K} + \mathbf{q}$, which have been shifted by small amount from the Dirac point (i.e. $|\mathbf{q}|/|\mathbf{K}| \ll 1$), it follows, to first order in momentum, that²

$$\phi(\mathbf{k}) \approx \frac{3}{2}iaq_y - \frac{3}{2}aq_x. \quad (4.1.13)$$

Inserting this equation into the Hamiltonian (4.1.11) results in

²This can be realized by inserting the definitions of δ_i into Eq. (4.1.10) and then Taylor expanding the exponentials to first order in q .

$$\mathbf{H}_{\mathbf{k}} \approx \hbar v_F \begin{bmatrix} 0 & -q_x + iq_y \\ -q_x - iq_y & 0 \end{bmatrix}, \quad (4.1.14)$$

where $v_F \equiv 3ta/(2\hbar)$ is the Fermi velocity of the π electrons in graphene with an approximate value of $v_F \approx c/300 = 1 \times 10^6$ [7]. The spectrum is found by calculating the eigenvalue of this Hamiltonian, which yields

$$\boxed{E_{\pm} = \pm \hbar v_F q}, \quad (4.1.15)$$

where $q \equiv |\mathbf{q}| = \sqrt{q_x^2 + q_y^2}$. It is thus seen that the band structure exhibits a linear behaviour in the vicinity of the Dirac points, as was previously stated. This linearity of the spectrum is indeed responsible for many of graphene's profound properties. The Hamiltonian (4.1.14) can be written in terms of the pauli matrices, which is accomplished by a transformation to real space³

$$\mathbf{H} \approx \hbar v_F \begin{bmatrix} 0 & i\partial_x + \partial_y \\ i\partial_x - \partial_y & 0 \end{bmatrix} = -v_F(\sigma_x p_x + \sigma_y p_y) = -v_F \boldsymbol{\sigma} \cdot \mathbf{p}, \quad (4.1.16)$$

where the pauli matrices are denoted by σ_x and σ_y . This Hamiltonian justifies the naming of the Dirac points, since Eq. (4.1.16) mimics the Dirac Hamiltonian for fermions in two dimensions⁴.

4.2 Conductivity of graphene

A response functions describes the relationship between an external perturbation and the response of a material. Examples of such response functions could be the conductivity or the dielectric function. It was seen in Sec. (2.2) that each of these two quantities could be described in terms of the other, meaning that the choice between them is completely a matter of convenience in the situation at hand. Graphene is no exception to these considerations, meaning that the optical surface conductivity is of crucial importance when it comes to the physics describing the response of a graphene sheet to electromagnetic radiation.

It is a common practice to divide the conductivity into two contributions. The first contribution accounts for the possibility of electrons to perform intraband transitions within the valence or conduction band (where momentum is not conserved), while the second contribution describes the vertical interband transitions from the valence to the conduction band (this process conserves momentum). The total conductivity of graphene thus takes the form

³Conversion into real space is recognized through the momentum operator $\mathbf{p} = -i\hbar \frac{\partial}{\partial \mathbf{r}} = \hbar \mathbf{q}$.

⁴The Dirac Hamiltonian in two dimensions for a spin 1/2 particle is given by $H_D = c \sum_i \alpha_i p_i + \beta mc^2$, which can be identified with Eq. (4.1.16) in the limit of zero mass, while identifying α with σ and c with v_F

$$\sigma_g(\omega) = \sigma_{intra}(\omega) + \sigma_{inter}(\omega) \quad (4.2.1)$$

An analytical expression can be obtained for the conductivity of graphene via Kubo's formula in the scheme of linear response theory [20, 21, 22]. The intraband conductivity with this approach becomes [11]

$$\sigma_{intra}(\omega) = \frac{\sigma_0}{\pi} \frac{4}{\hbar\gamma - i\hbar\omega} \left[E_F + 2k_B T \ln \left(1 + e^{-E_F/k_B T} \right) \right], \quad (4.2.2)$$

where k_B is Boltzmann's constant, γ is the relaxation time, E_F is the Fermi energy and σ_0 is the universal dynamic conductivity of graphene given by $\sigma_0 = e^2\pi/2h$, while the expression for the interband transitions reads

$$\sigma_{inter}(\omega) = \sigma_0 \left[G(\hbar\omega/2) + i \frac{4\hbar\omega}{\pi} \int_0^\infty \frac{G(E) - G(\hbar\omega/2)}{(\hbar\omega)^2 - 4E^2} dE \right], \quad (4.2.3)$$

where

$$G(x) = \frac{\sinh\left(\frac{x}{k_B T}\right)}{\cosh\left(\frac{E_F}{k_B T}\right) + \cosh\left(\frac{x}{k_B T}\right)}. \quad (4.2.4)$$

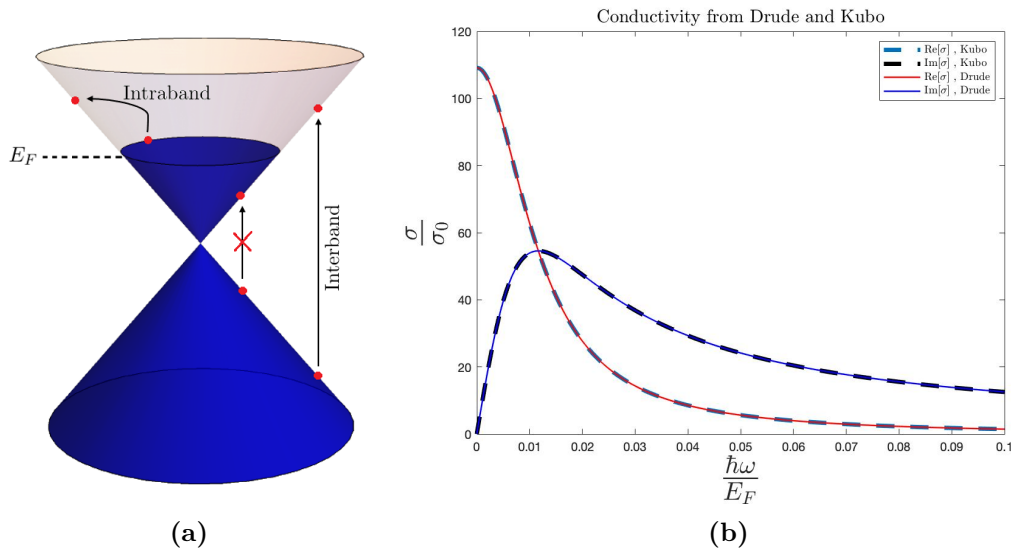


Figure 4.3: (a) Illustration of the possible electron/hole transitions in doped graphene, where the red cross imply a forbidden transition. (b) Optical conductivity of graphene from both Drude (solid lines) and Kubo's expression (dashed lines) in the THz regime. The parameters have been chosen to be $E_F = 0.3$ eV and $\hbar\gamma = 3.7$ meV.

These expressions does at first glance seem relatively complicated, fortunately they can be simplified in the limit of zero temperature [7], leading to [11]

$$\sigma_{intra}(\omega) = \frac{\sigma_0}{\pi} \frac{4E_F}{\hbar\gamma - i\hbar\omega}, \quad (4.2.5)$$

$$\sigma_{inter}(\omega) = \sigma_0 \left[\Theta(\hbar\omega - 2E_F) + \frac{i}{\pi} \ln \left| \frac{\hbar\omega - 2E_F}{\hbar\omega + 2E_F} \right| \right], \quad (4.2.6)$$

where $\Theta(\hbar\omega - 2E_F)$ denotes the Heaviside step-function. The types of possible band transitions have been schematically illustrated in Fig. 4.3a in the case of doped graphene. The red cross indicates a transition, which is forbidden due to the principle of Pauli blocking. The interband conductivity (4.2.6) naturally accounts for this restriction in the Heaviside step-function, meaning that this term yields zero contribution once $2E_F > \hbar\omega$. Consequently the optical conductivity of graphene can approximately be described by a single term, which is that of the intraband Drude-like conductivity

$$\sigma_g(\omega) \approx \frac{\sigma_0}{\pi} \frac{4E_F}{\hbar\gamma - i\hbar\omega}. \quad (4.2.7)$$

For typical doping levels of graphene in room temperature, this argument holds for frequencies in the THz and mid-IR regime. This simple description of graphene's response function is verified in Fig. 4.3b, where the approximated conductivity of graphene (4.2.7) have been plotted together with the full conductivity (4.2.1) in the THz spectral region. Clearly these two solutions is inseparable in this spectral region, meaning that the approximated drude conductivity of graphene is indeed justified. It is expected, however, that this approximation will start to fail once the frequency reaches a certain value, at which interband transitions becomes significant.

4.3 Transfer-matrix method for graphene

Transfer-matrices are used in optics to describe the propagation of electromagnetic waves through different dielectrics, conductors or a combination of both. This method utilizes boundary conditions, in order to encapsulate the effect of multiple layers on the fields into a single matrix, which then relates the fields at one point in space \mathbf{R}' given an initial point \mathbf{R} . It is therefore advantageous to exploit the transfer-matrix method when the problem at hand involves the calculation of transmission and reflection coefficients in structured multilayer systems. This method will be discussed with special attention to systems containing one or two graphene layers.

4.3.1 Transfer-matrix for single graphene layer

The geometry at hand is shown schematically in Fig. 4.4, where the graphene layer is positioned between two dielectrics, denoted ϵ_1 and ϵ_2 , which is assumed to be semi-infinite.

The transfer-matrix method deals with incoming and reflected waves in the two dielectrics, which leads to the following magnetic field

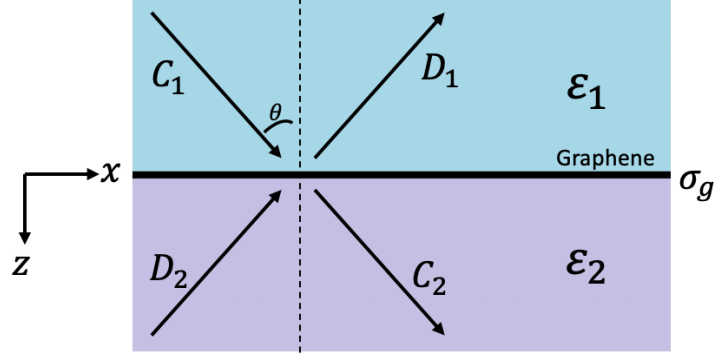


Figure 4.4: Scattering of electromagnetic radiation on a single-layer graphene placed at $z = 0$ between two dielectric media with relative permittivity ϵ_1 and ϵ_2 . The optical conductivity of the graphene sheet is described by σ_g .

$$\mathbf{B}_y^{(j)}(\mathbf{r}, t) = (C_j e^{ik_{j,z}z} + D_j e^{-ik_{j,z}z}) e^{i(qx - \omega t)} \hat{\mathbf{y}}, \quad (4.3.1)$$

where transverse magnetic waves have been assumed, C_j and D_j are constants to be determined and j denotes medium index. Inserting this magnetic field into Maxwell's equation (2.1.12d) yields the electric field

$$\mathbf{E}_x^{(j)}(\mathbf{r}, t) = \frac{k_{j,z} c^2}{\omega \epsilon_j} (C_j e^{ik_{j,z}z} - D_j e^{-ik_{j,z}z}) e^{i(qx - \omega t)} \hat{\mathbf{x}}, \quad (4.3.2)$$

where $k_{j,z}$ is given by

$$k_{j,z} = \sqrt{\epsilon_j \frac{\omega^2}{c^2} - q^2}. \quad (4.3.3)$$

The boundary conditions across the graphene interface is then introduced in order to relate the field amplitudes in the two dielectrics. These boundary conditions is given by

$$E_x^{(1)}(z = 0) = E_x^{(2)}(z = 0), \quad (4.3.4)$$

$$B_y^{(1)}(z = 0) - B_y^{(2)}(z = 0) = \mu_0 \sigma_g E_x^{(1)}(z = 0), \quad (4.3.5)$$

demonstrating the continuity and discontinuity of the tangential components of the the electric and magnetic field respectively, and where σ_g expresses the optical conductivity of

graphene. Substituting the fields in Eq. (4.3.1) and (4.3.2) into the boundary conditions leads to a system of linear equations containing the field amplitudes, which can be cast into a single matrix equation

$$\begin{bmatrix} 1 & -1 \\ 1 & 1 \end{bmatrix} \begin{bmatrix} C_1 \\ D_1 \end{bmatrix} = \begin{bmatrix} \eta_1 & -\eta_1 \\ 1 + \xi_{\sigma,1} & 1 - \xi_{\sigma,1} \end{bmatrix} \begin{bmatrix} C_2 \\ D_2 \end{bmatrix}, \quad (4.3.6)$$

where the following definitions have been used

$$\eta_1 = \frac{\epsilon_1 k_{2,z}}{\epsilon_2 k_{1,z}} \quad \text{and} \quad \xi_{\sigma,1} = \frac{\sigma_g k_{2,z}}{\omega \epsilon_0 \epsilon_2}, \quad (4.3.7)$$

with the subscript 1 referring to the first interface, which will be convenient for future purposes. The relation between the amplitudes in medium one and two is then given by

$$\begin{bmatrix} C_1 \\ D_1 \end{bmatrix} = \mathbf{T}_{1 \rightarrow 2} \begin{bmatrix} C_2 \\ D_2 \end{bmatrix}, \quad (4.3.8)$$

where $\mathbf{T}_{1 \rightarrow 2}$ is the single layer graphene transfer matrix, reading

$$\mathbf{T}_{1 \rightarrow 2} = \frac{1}{2} \begin{bmatrix} 1 + \eta_1 + \xi_{\sigma,1} & 1 - \eta_1 - \xi_{\sigma,1} \\ 1 - \eta_1 + \xi_{\sigma,1} & 1 + \eta_1 - \xi_{\sigma,1} \end{bmatrix}. \quad (4.3.9)$$

The elements of this transfer-matrix⁵ can now be used to derive the reflection and transmission coefficients for a single graphene layer via [23]

$$r = \frac{T_{21}^{1 \rightarrow 2}}{T_{11}^{1 \rightarrow 2}} \quad \text{and} \quad t = \frac{1}{T_{11}^{1 \rightarrow 2}}. \quad (4.3.10)$$

The norm squared of the transmission, t , and reflection coefficient, r , yields the transmittance and the reflectance

$$\mathcal{T}_{SLG} = \frac{\epsilon_1 k_{2,z}}{\epsilon_2 k_{1,z}} \left| \frac{2}{1 + \eta_1 + \xi_{\sigma,1}} \right|^2 \quad \text{and} \quad \mathcal{R}_{SLG} = \left| \frac{1 - \eta_1 + \xi_{\sigma,1}}{1 + \eta_1 + \xi_{\sigma,1}} \right|^2, \quad (4.3.11)$$

respectively. It is then straight forward to evaluate the absorbance

⁵The following notation will be adapted $\mathbf{T}_{1 \rightarrow 2} = \begin{bmatrix} T_{11}^{1 \rightarrow 2} & T_{12}^{1 \rightarrow 2} \\ T_{21}^{1 \rightarrow 2} & T_{22}^{1 \rightarrow 2} \end{bmatrix}$.

$$\boxed{\mathcal{A}_{SLG} = 1 - \mathcal{T}_{SLG} - \mathcal{R}_{SLG}}. \quad (4.3.12)$$

Assuming that the light beam approaches the graphene sheet at normal incidence leads to the following transmittance

$$\mathcal{T}_{SLG}^{normal} = \sqrt{\frac{\epsilon_1}{\epsilon_2}} \left| \frac{2\sqrt{\epsilon_2}}{\sqrt{\epsilon_1} + \sqrt{\epsilon_2} + \frac{\sigma_g}{c\epsilon_0}} \right|^2, \quad (4.3.13)$$

while the reflectance becomes

$$\mathcal{R}_{SLG}^{normal} = \left| \frac{\sqrt{\epsilon_2} - \sqrt{\epsilon_1} + \frac{\sigma_g}{c\epsilon_0}}{\sqrt{\epsilon_2} + \sqrt{\epsilon_1} + \frac{\sigma_g}{c\epsilon_0}} \right|^2. \quad (4.3.14)$$

This transmittance, reflectance and the corresponding absorbance is plotted as a function of frequency in Fig. 4.5b for a single layer of graphene surrounded by air on both sides. An interesting thing to note here, is that the absorbance is frequency independent at frequencies corresponding to visible light, with a value of approximately 2.3%, which constitute the universal absorption of a single-layer graphene. This result may be derived in an alternative way, using the fine-structure constant, given in appendix A.1.

4.3.2 Transfer-matrix for double graphene layer

One of the great advantages of the transfer-matrix method lies in the straight forward generalization to double- or multi-layered graphene structures. For instance, the overall transfer-matrix for a double-layered graphene system, where the two graphene layers is separated by a dielectric medium of thickness d , is simply given by two transfer-matrices with identical structure as (4.3.9) and a propagation matrix, $\mathbf{P}_2(d)$, describing the plane wave propagation of the electromagnetic beam in medium 2. This reasoning thus enables the writing of the double-layer graphene transfer-matrix without any further calculations

$$\mathbf{T}_{1 \rightarrow 3} = \mathbf{T}_{1 \rightarrow 2} \cdot \mathbf{P}_2(d) \cdot \mathbf{T}_{2 \rightarrow 3}, \quad (4.3.15)$$

where the propagation matrix are given by

$$\mathbf{P}_2(d) = \begin{bmatrix} e^{-ik_{2,z}d} & 0 \\ 0 & e^{ik_{2,z}d} \end{bmatrix}. \quad (4.3.16)$$

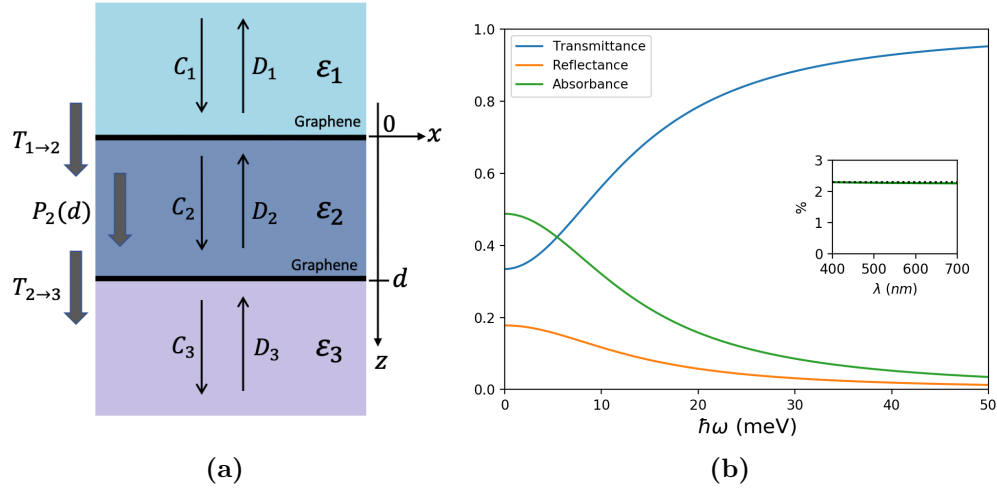


Figure 4.5: (a) Illustration of double layered graphene system exposed to electromagnetic radiation at normal incidence. The graphene sheets is placed at $z = 0$ and $z = d$ and separated by a dielectric medium of distance d with corresponding permittivity ϵ_2 . The matrices describing the propagation of the radiation is shown to the left of the figure. (b) Transmittance, reflectance and absorbance of a single-graphene layer as a function of the frequency. The light beam is assumed approach the graphene sheet at normal incidence. The subfigure illustrates the frequency-independent absorption of graphene at visible wavelengths, with a value of $\approx 2.3\%$ represented by the black-dotted line. Parameters: $\epsilon_1 = \epsilon_2 = 1$, $E_F = 0.1$ eV and $\hbar\gamma = 8$ meV.

The meaning of these matrices is schematically illustrated in Fig 4.5a, where the electromagnetic radiation is assumed to hit the graphene layers at normal incidence. The transmittance, reflectance and absorbance now follows naturally by replacing $1 \rightarrow 2$ by $1 \rightarrow 3$ in Eq. (4.3.9) [11]

$$\mathcal{T}_{DLG} = \frac{\epsilon_1 k_{3,z}}{\epsilon_3 k_{1,z}} \left| \frac{1}{T_{11}^{1 \rightarrow 3}} \right|^2, \quad (4.3.17)$$

$$\mathcal{R}_{DLG} = \left| \frac{T_{21}^{1 \rightarrow 3}}{T_{11}^{1 \rightarrow 3}} \right|^2, \quad (4.3.18)$$

$$\mathcal{A}_{DLG} = 1 - \mathcal{T}_{DLG} - \mathcal{R}_{DLG}. \quad (4.3.19)$$

Clearly these equations resembles an identical structure as for the single-layer graphene equations. In fact, the form of equation (4.3.17)-(4.3.19) remains the same for a system of N graphene layers, where N can take any positive finite number. The transfer-matrix method is therefore a good candidate to compute the band-structure of photonic crystals [11].

Chapter 5

Plasmonic Excitation in Graphene

The unique electronic properties of graphene, together with its two-dimensional nature makes this material a very interesting prospect in the field of plasmonics [11]. Doped graphene does not experience significant damping from interband transitions in the THz and mid-IR part of the electromagnetic spectrum (as discussed in Sec. (4.2)) and is therefore able to sustain plasmonic excitations in this regime. One favourable aspect of graphene surface plasmons (GSPs), as compared to the conventional SPPs at surfaces of three-dimensional (3D) conductors, is the relationship between the Fermi level and the corresponding frequency of the plasmon resonance. This means, in other words, that the GSP is tunable simply by adjusting the doping level in the graphene sheet. Additionally, GSPs are able to attain small losses, thus achieving relatively long lifetimes.

This chapter will mainly be concerned with the description of the dispersion relation for GSPs in the case of single and double graphene interfaces. This will equip us with the information needed in order to discuss properties like field confinement, propagation length and tuneability.

5.1 Single Graphene Interface

The simplest imaginable system able to sustain GSPs, is that of a single planar infinite graphene sheet separating two semi-infinite dielectric mediums. This geometry has been depicted in Fig. 5.1a. The graphene sheet is located at $z = 0$ and the dielectric constant of the two dielectric media has been denoted ϵ_1 and ϵ_2 .

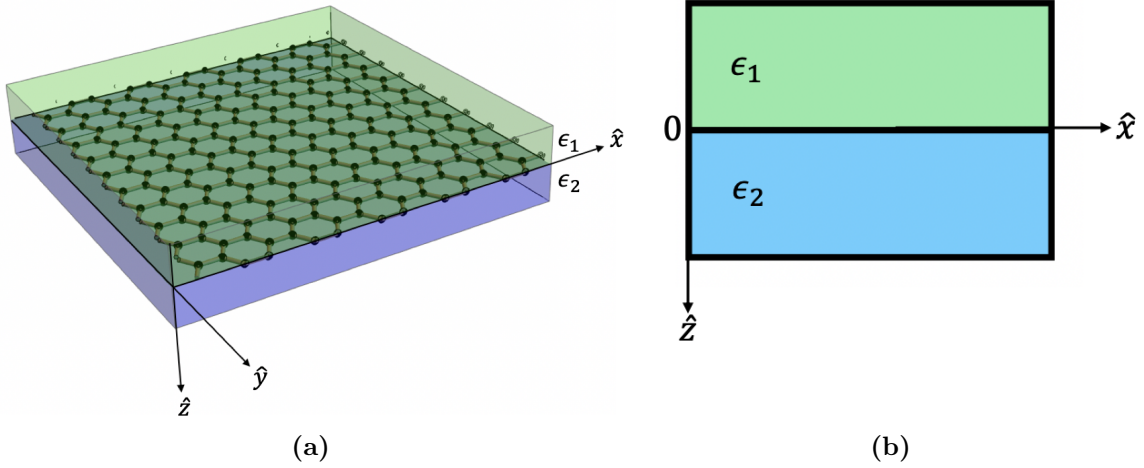


Figure 5.1: Drawing of a monolayer graphene located between two dielectric media with dielectric constants ϵ_1 and ϵ_2 , referring respectively to the $z < 0$ and $z > 0$ half-spaces. The graphene sheet is placed at $z = 0$.

5.1.1 GSP dispersion relation

TM-waves (p-polarized electromagnetic waves) will serve as the starting point for investigating the dispersion relation of GSPs. This derivation very much goes along the same lines as for the SPP at a single dielectric-metal interface in Sec. (3.1.1). The electric and magnetic fields in the two dielectric media is, in this case, given by Eq. (3.1.1). Inserting these fields into Maxwell's curl equations (2.1.12c) and (2.1.12d) yields

$$E_{j,x} = is_j \frac{\kappa_j c^2}{\omega \epsilon_j} B_{j,y} \quad (5.1.1)$$

$$E_{j,z} = -\frac{qc^2}{\omega \epsilon_j} B_{j,y} \quad (5.1.2)$$

The tangential boundary conditions, which links the electromagnetic fields on the two sides of the graphene sheet together is given by Eq. (2.1.16c) and (2.1.16d), and reads

$$E_{1,x}(x, z)|_{z=0} = E_{2,x}(x, z)|_{z=0}, \quad (5.1.3)$$

$$B_{1,y}(x, z)|_{z=0} - B_{2,y}(x, z)|_{z=0} = \mu_0 J_x(x) = \mu_0 \sigma_{xx} E_{2,x}(x, z)|_{z=0}. \quad (5.1.4)$$

These two boundary conditions describe the continuity of electric field and the discontinuity of the magnetic field across the interface occupied by the graphene sheet. It is assumed that the graphene sheet has zero extension along the z-axis, meaning that it can be regarded as a truly two-dimensional material, where the frequency dependent conductivity $\sigma(\omega)$

incorporates all the electromagnetic properties. The GSP dispersion relation is now derived by inserting the fields into the boundary conditions (5.1.3) and (5.1.4), which leads to [11]

$$\boxed{\frac{\epsilon_1}{\kappa_1(q, \omega)} + \frac{\epsilon_2}{\kappa_2(q, \omega)} + i \frac{\sigma(\omega)}{\omega \epsilon_0} = 0}, \quad (5.1.5)$$

where κ_j is given by Eq. (3.1.3). The conductivity in Eq. (5.1.5) is a function of the frequency, while κ_j is a function of both the frequency and the wavevector. Thus it becomes apparent, that this dispersion relation is an implicit equation, which cannot be solved analytically. Consequently one has to rely on numerical methods in order to even solve this simple geometry.

It is seen that the third term of the GSP dispersion relation (5.1.5) contains an imaginary unit, accordingly this equation only has real solutions when the real part of the conductivity is zero and the imaginary part is positive. Contrary, the dispersion relation delivers complex solutions in the case of a non-zero real part of the conductivity. This does not come as a surprise, since it is well-known that the real part of the conductivity is related to the attenuation in the system. The solutions to the dispersion relation will now be discussed in the case of zero damping ($\gamma = 0$) and a non-zero damping ($\gamma \neq 0$).

Zero damping ($\gamma = 0$):

It was seen in Sec. (4.2) that the optical conductivity of graphene could be described by a Drude-like expression

$$\sigma(\omega) = \sigma_0 \frac{4i}{\pi} \frac{E_F}{\hbar\omega + i\hbar\gamma}, \quad (5.1.6)$$

for the frequency interval between THz and mid-IR, if $E_F \gg k_B T$ and $E_F \gg \hbar\omega$. This conductivity is now substituted into the GSP dispersion relation and solutions is then calculated numerically for $\gamma = 0$, the result is shown in Fig. 5.2a. This spectrum of the GSP very much resembles the same behaviour as the ordinary SPP dispersion relation at metal-dielectric interfaces discussed in Sec. (3). However, the main difference is that the GSP is able to sustain high field confinement in the THz to mid-IR frequency interval, as opposed to the free light-like behaviour of dielectric-metal SPPs in this regime.

The dispersion relation once again lies to the right of the corresponding light line, which demonstrates the bound nature of the GSP. It is therefore necessary to implement special techniques in order to excite these types of plasmons in flat graphene, example of such a technique will be discussed in the form of the Otto configuration in Sec. (B.1). The great advantage of GSPs being tunable via doping is seen as the appearance of the Fermi level in Eq. (5.1.6). The frequency which satisfies the resonance condition of the GSP is therefore increased for an increase in the Fermi level, this behaviour have been illustrated in Fig. 5.2b.

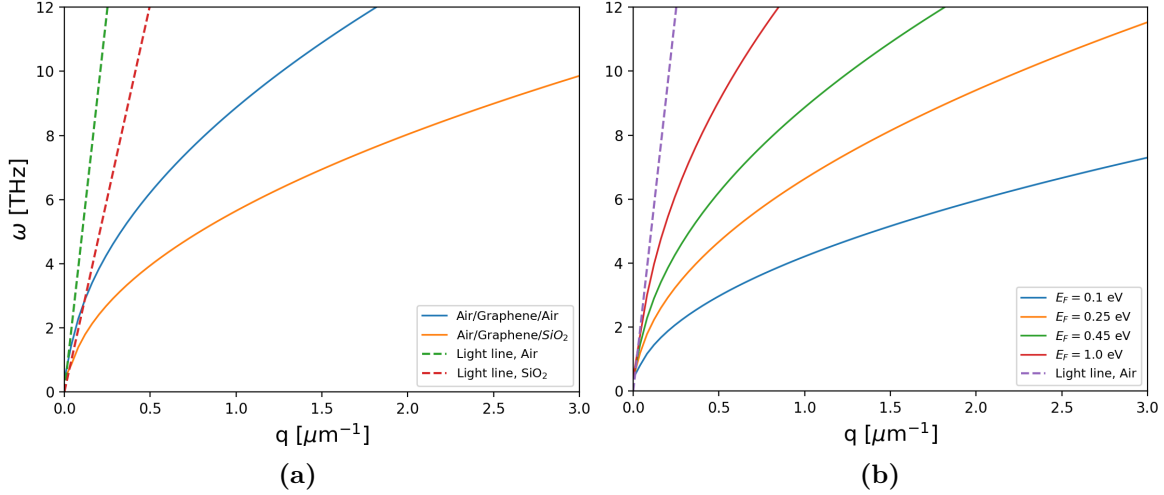


Figure 5.2: (a) Spectrum of TM GSPs for an air/graphene/air geometry (solid blue curve) and for an air/graphene/SiO₂ structure (solid orange curve), in which the graphene conductivity have been modelled without damping ($\gamma = 0$). The dashed straight lines corresponds to the light lines in air (green) and in SiO₂ (red). The following parameters have been used: $E_F = 0.45$ eV, $\epsilon_1 = 1$ and $\epsilon_2 = 3.9$. (b) Lossless single graphene sheet dispersion relation for different values of the Fermi level in an air/graphene/air geometry ($\epsilon_1 = \epsilon_2 = 1$).

Non-zero damping ($\gamma \neq 0$):

In the case of zero damping, then the conductivity is purely imaginary and hence the wavevectors solving the dispersion relation is real. When the damping is non-zero, on the other hand, then the wavevectors becomes complex instead, $q = q' + iq''$, where the imaginary part is identified with the damping. The spectrum for TM GSPs for different values of the damping parameter have been depicted in Fig. 5.3.

It is seen that the dispersion relation crosses the light line at small wavevectors, which is in opposition to the previously discussed SPP and GSP dispersion relations. One would then expect that GSPs could be excited by direct exposure of electromagnetic waves. However, this is not the case, since the region for small wavevectors constitute the overdamped regime ($\omega/\gamma < 1$), at which GSPs can't exist. Further notice that the frequency increases when the damping parameter is raised towards larger values. This change in the spectrum is only observed for sufficiently small wavevectors, which has been shown in the subfigure. On the other hand, the modes becomes indistinguishable when the frequencies approach larger values.

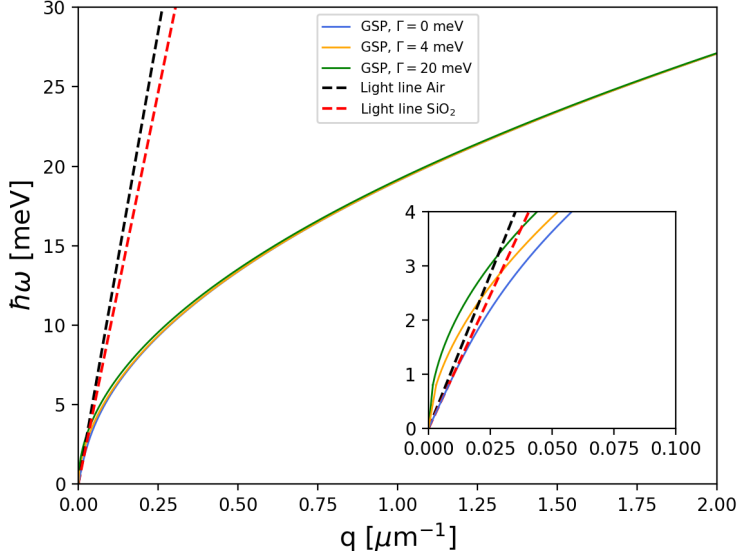


Figure 5.3: Numerical solution to Eq. (5.1.5) using different non-zero values of the damping parameter $\Gamma \equiv \hbar\gamma$. The solution with zero damping ($\Gamma = 0$) in the plot serves as a comparison to the attenuated modes and the dashed lines illustrate the light lines in the dielectric mediums. A zoom onto small wavevectors have been performed in the sub-figure, where the axis labels are identical to the main figure. Parameters: $\epsilon_1 = 1$, $\epsilon_2 = 4$ and $E_F = 0.5$ eV.

5.1.2 Penetration depth and field confinement for GSPs

Although the GSP dispersion has to be solved numerically, it is possible to simplify the expression by assuming a symmetric geometry, in which $\epsilon_1 = \epsilon_2$, thus Eq. (5.1.5) becomes

$$1 + i \frac{\sigma(\omega)}{2\omega\epsilon\epsilon_0} \sqrt{q^2 - \epsilon \frac{\omega^2}{c^2}} = 0, \quad (5.1.7)$$

where $\epsilon = (\epsilon_1 + \epsilon_2)/2$ denotes the average value of the dielectric constants. The propagation length and field confinement can now be analysed by inserting the full complex drude conductivity (5.1.6) into the simplified dispersion relation (5.1.7) and isolating for $\kappa(q, \omega)$

$$\kappa(q, \omega) = \frac{\epsilon \hbar}{2\alpha c} \frac{(\omega^2 + i\gamma\omega)}{E_F}. \quad (5.1.8)$$

The field confinement can now be found by substituting (5.1.8) into the expression for penetration depth (3.1.12), which yields

$$\zeta_{GSP} = \frac{1}{\text{Re}\{\kappa\}} = \frac{2\alpha \hbar c}{\epsilon} \frac{E_F}{(\hbar\omega)^2}. \quad (5.1.9)$$

Thus the field confinement of the GSP resembles the same frequency dependence, as for the SPP in the dielectric medium, meaning that it increases (decreases) for larger (smaller) frequencies (see Fig. 3.3b), provided that the doping level is held constant.

The GSP dispersion in the symmetric environment can be further simplified in the electrostatic limit ($\kappa \rightarrow q$). This wavevector does, in general, take complex values (assuming real valued frequencies) because of the fact that the damping parameter is non-zero, and the dispersion relation reads

$$q' + iq'' \approx \frac{\epsilon \hbar}{2\alpha c} \frac{(\omega^2 + i\gamma\omega)}{E_F}. \quad (5.1.10)$$

It is then straight forward to read of the real and imaginary part of the wavevector from (5.1.10), which yields

$$q' = \frac{\epsilon}{2\alpha \hbar c} \frac{(\hbar\omega)^2}{E_F}, \quad (5.1.11)$$

$$q'' = \frac{\epsilon \hbar}{2\alpha c} \frac{\gamma\omega}{E_F}. \quad (5.1.12)$$

Now the GSP propagation length is evaluated by substituting the imaginary part into Eq. (3.3a), defining the point at which the GSP intensity has fallen off by $1/e$, obtaining

$$L_{GSP} = \frac{1}{2q''} = \frac{\alpha c E_F}{\epsilon \hbar \gamma\omega}. \quad (5.1.13)$$

This length does, as anticipated, decrease with an increased damping parameter in the case of a constant doping level.

5.1.3 Numerical example of GSP localization

The wavelength of the GSP can be obtained using the real part of the wavevector $\lambda_{GSP} = 2\pi/\text{Re}\{q'\}$. Comparing the GSP wavelength with that of light in vacuum, λ_0 , yields

$$\frac{\lambda_{GSP}}{\lambda_0} = \frac{\alpha 2E_F}{\epsilon \hbar\omega}. \quad (5.1.14)$$

Assuming a situation, at which a plane graphene sheet is placed between a piece of SiO₂ with $\epsilon_{SiO_2} = 4$, and air with $\epsilon_{air} = 1$, the average dielectric environment becomes $\epsilon = 2.5$. Using a doping level of $E_F = 0.3$ eV and frequency of $\omega/2\pi = 12$ THz, we get a ratio of $\lambda_{GSP}/\lambda_0 \approx 0.036$. This means that the wavelength of the GSP is significantly smaller as compared to the wavelength of the incoming light. The frequency of 12 THz corresponds to a wavelength of $\lambda_0 \approx 25$ μm , which according to the calculated ratio leads to $\lambda_{GSP} \approx 880$ nm. This degree of localization by far exceeds the diffraction limit defining the minimal distance by which one can separate two airy discs in a microscope. It becomes apparent that the confinement of the GSPs increases with an increase of the frequency. However a natural upper bound exists for this confinement, which is related to the Fermi frequency $\omega_F \hbar = E_F$. Electromagnetic radiation with frequencies beyond this value will contribute to interband transitions and hence intensify the losses in the system.

5.1.4 Single-layer graphene fields profile of GSPs

The fields of the derived p-polarized GSP dispersion relation in single-layer graphene (SLG) can be explicitly visualized by some simple considerations. The visualization in this section will be done for the electric field, although it should be mentioned that an identical procedure could be done for the magnetic field as well.

First a characteristic frequency ω_c is introduced in Eq. (5.1.5), then the equation is solved numerically in order to retrieve the corresponding characteristic wavevector q_c . Combining the expressions for the electric field amplitudes in Eq. (5.1.1) and (5.1.2) yields

$$E_{j,z} = i s_j \frac{q}{\kappa_j} E_{j,x}. \quad (5.1.15)$$

The amplitudes is now normalized with $E_{1,x}$, so that the field components reads

$$E_{1,x} = 1, \quad (5.1.16)$$

$$E_{1,z} = -i \frac{q_c}{\kappa_1(q_c, \omega_c)}, \quad (5.1.17)$$

$$E_{2,x} = 1, \quad (5.1.18)$$

$$E_{2,z} = i \frac{q_c}{\kappa_2(q_c, \omega_c)}, \quad (5.1.19)$$

where the boundary condition (5.1.3) have been utilized. The electric vector field is evaluated by insertion of these components into

$$\mathbf{E}_{GSP}(\mathbf{r}) = E_x(x, z)\hat{\mathbf{x}} + E_z(x, z)\hat{\mathbf{z}}, \quad (5.1.20)$$

where E_x and E_z in the two dielectric mediums is given by

$$E_\mu(x, z) = \begin{cases} \text{Re}\{E_{1,\mu} e^{-\kappa_1|z|} e^{iqx}\}, & \text{if } z \leq 0 \\ \text{Re}\{E_{2,\mu} e^{-\kappa_2|z|} e^{iqx}\}, & \text{if } z > 0 \end{cases}, \quad (5.1.21)$$

with $\mu = x, z$. These electric fields is shown in Fig. 5.4. The upper figure illustrates a vectorial density plot of the total field, which have been evaluated from Eq. (5.1.20), while the middle and lower figure represents a density plot of the x- and z-component respectively. The collective nature of the GSPs is clear in these figures, with alternating strong and weak electric fields as one moves along the x-axis in the vicinity of the graphene sheet (solid black line). Further notice the exponential decay of the field intensity when the distance to the graphene plane increases. Finally the symmetric and antisymmetric behaviour of the x- and z-component, respectively, becomes apparent in the middle and lower figure.

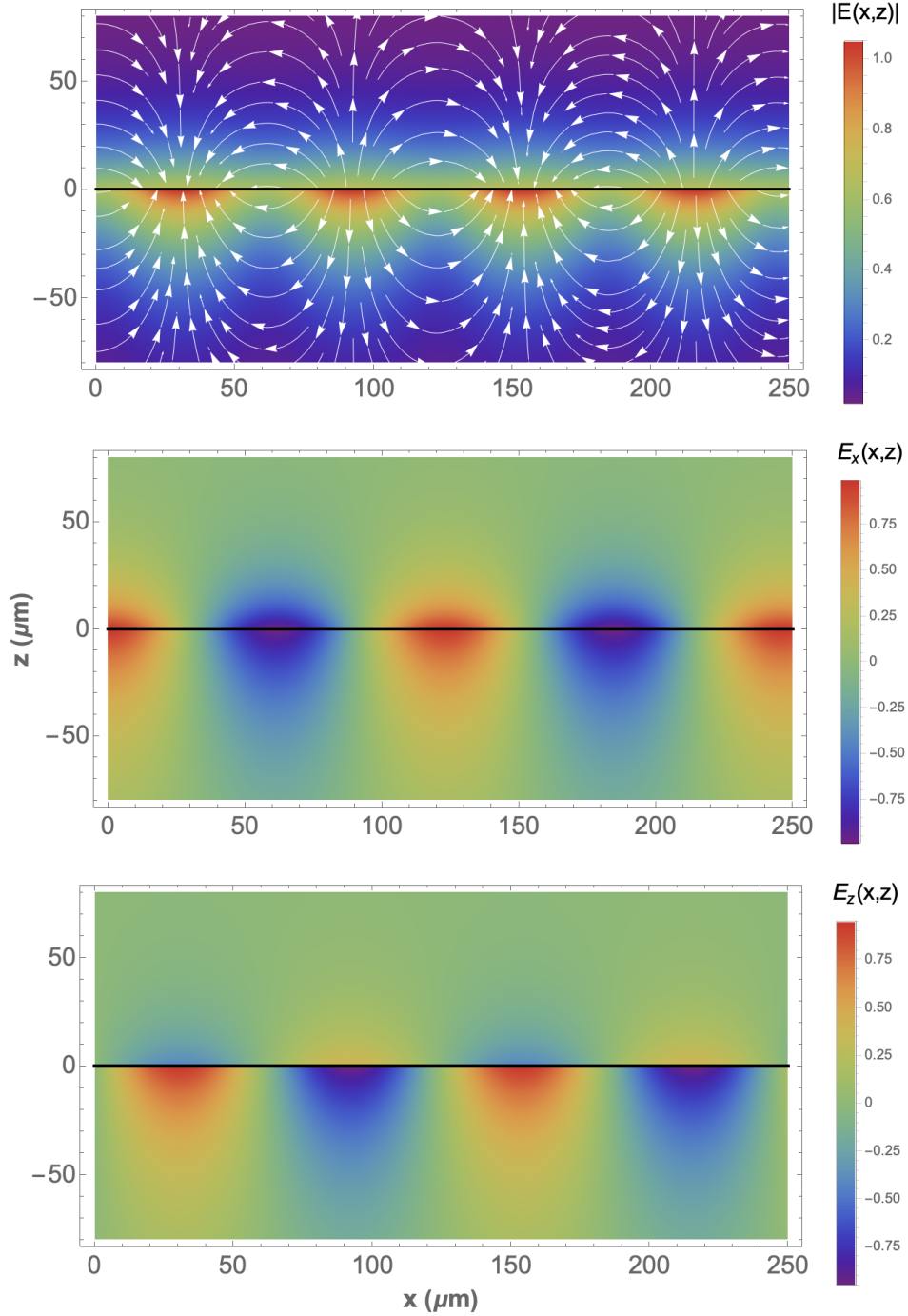


Figure 5.4: Illustration of the electric fields due to propagating TM GSPs in $\text{SiO}_2/\text{graphene}/\text{air}$ structure. The black solid line at $z = 0$ indicates the graphene sheet. Parameters: $\gamma = 0$, $\epsilon_{\text{air}} = 1$, $\epsilon_{\text{SiO}_2} = 3,8$, $\omega_c = 2\pi \cdot 1\text{THz}$ and $q_c = 0,051\mu\text{m}$.

5.2 Double Graphene Interface

The case of a system with two sheets of doped graphene separated by a distance d is now examined. The middle medium is assumed to be that of a dielectric with dielectric constant ϵ_2 , and the two surrounding media is denoted by ϵ_1 and ϵ_3 for the upper and lower medium, respectively. The structure at hand have been depicted in Fig. 5.5.

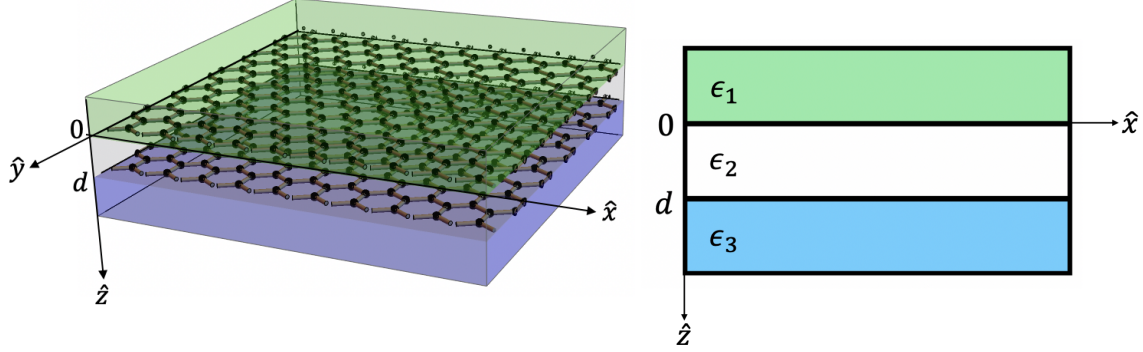


Figure 5.5: Illustration of a double-layer graphene geometry. The two graphene sheets, located at $z = 0$ and $z = d$, are separated by dielectric medium of thickness d and dielectric constant ϵ_2 . The upper and lower media, defined by the relative permittivities ϵ_1 and ϵ_3 respectively, is assumed to be semi-infinite.

5.2.1 Spectrum of double-layer graphene geometry

The derivation of the double-layer graphene (DLG) spectrum does, in general, follow the same procedure as for the ordinary double dielectric-metal interface SPPs. Solutions to Maxwell's equations is therefore assumed to take the form of Eq. (3.1.1) for the medium at $z < 0$ and $z > d$, while a superposition of exponentially growing and decaying waves takes place in the middle medium ($0 > z > d$) given by Eq. (3.2.1a) and (3.2.1b). The boundary conditions at the $z = d$ interface reads

$$E_{2,x}^{(+)} e^{\kappa_2 d} + E_{2,x}^{(-)} e^{-\kappa_2 d} = E_{3,x} e^{-\kappa_3 d}, \quad (5.2.1)$$

$$B_{2,y}^{(+)} e^{\kappa_2 d} + B_{2,y}^{(-)} e^{-\kappa_2 d} - B_{3,y} e^{-\kappa_3 d} = \mu_0 \sigma(\omega) E_{3,x} e^{-\kappa_3 d}, \quad (5.2.2)$$

and

$$E_{1,x} = E_{2,x}^{(+)} + E_{2,x}^{(-)}, \quad (5.2.3)$$

$$B_{1,y} = B_{2,y}^{(+)} + B_{2,y}^{(-)} + \mu_0 \sigma(\omega) E_{1,x}, \quad (5.2.4)$$

for the $z = 0$ interface, where identical doping levels for the two graphene sheets have been assumed. These boundary conditions together with the expressions relating the amplitudes

of the magnetic and electric field in upper and lower medium in Eq. (3.1.2a)-(3.1.2b) and in the middle medium (3.2.2a)-(3.2.2d), form a system of linear equations, which can be written in the following matrix form

$$\begin{bmatrix} -1 & 1 & 1 & 0 \\ \frac{\epsilon_1}{\kappa_1} + i\frac{\sigma}{\omega\epsilon_0} & -\frac{\epsilon_2}{\kappa_2} & \frac{\epsilon_2}{\kappa_2} & 0 \\ 0 & e^{\kappa_2 d} & e^{-\kappa_2 d} & -e^{-\kappa_3 d} \\ 0 & \frac{\epsilon_2}{\kappa_2} e^{\kappa_2 d} & -\frac{\epsilon_2}{\kappa_2} e^{-\kappa_2 d} & \left(\frac{\epsilon_3}{\kappa_3} + i\frac{\sigma}{\omega\epsilon_0}\right) e^{-\kappa_3 d} \end{bmatrix} \begin{bmatrix} E_{1,x} \\ E_{2,x}^{(+)} \\ E_{2,x}^{(-)} \\ E_{3,x} \end{bmatrix} = 0. \quad (5.2.5)$$

The condition for a non-trivial solutions is then found by setting the determinant of the matrix in Eq. (5.2.5) equal to zero, which after some algebra leads to [11]

$$e^{-\kappa_2 d} \left(\frac{\epsilon_3}{\kappa_3} + i\frac{\sigma}{\omega\epsilon_0} - \frac{\epsilon_2}{\kappa_2} \right) \left(\frac{\epsilon_1}{\kappa_1} + i\frac{\sigma}{\omega\epsilon_0} - \frac{\epsilon_2}{\kappa_2} \right) = e^{\kappa_2 d} \left(\frac{\epsilon_3}{\kappa_3} + i\frac{\sigma}{\omega\epsilon_0} + \frac{\epsilon_2}{\kappa_2} \right) \left(\frac{\epsilon_1}{\kappa_1} + i\frac{\sigma}{\omega\epsilon_0} + \frac{\epsilon_2}{\kappa_2} \right). \quad (5.2.6)$$

A plot of this DLG dispersion relation is given in Fig. 5.6. This spectrum share some of the features from the MDM and DMD SPPs discussed in Sec. (3.2). The interaction of fields from the two grapene sheets in the middle medium create hybridized modes, assuming that the spacing, d , between the graphene layers is sufficiently small. Consequently this perturbation removes the degeneracy in the system, and two distinct modes appears; one with a larger frequency, called the optical mode, and one with a smaller frequency, which is dubbed the acoustic mode. Two different separations is shown in Fig. 5.6, which is 100nm (solid lines) and 400nm (dot-dashed lines). It becomes obvious from these two separations that the "communication" between the fields, and hence the splitting of the modes, increases when the spacing decreases. The black dashed line represents the SLG spectrum, thus serving as a point of reference.

A way to verify the sense of Eq. (5.2.6) is to take the limit $\kappa_2 d \rightarrow \infty$, which yields

$$\left(\frac{\epsilon_3}{\kappa_3} + i\frac{\sigma}{\omega\epsilon_0} + \frac{\epsilon_2}{\kappa_2} \right) \left(\frac{\epsilon_1}{\kappa_1} + i\frac{\sigma}{\omega\epsilon_0} + \frac{\epsilon_2}{\kappa_2} \right) = 0. \quad (5.2.7)$$

This corresponds to the derived spectrum of a SLG (5.1.5). The first parenthesis in Eq. (5.2.7) represents the graphene interface separating medium 2 and 3, while the second parenthesis describes the graphene interface separating medium 1 and 2.

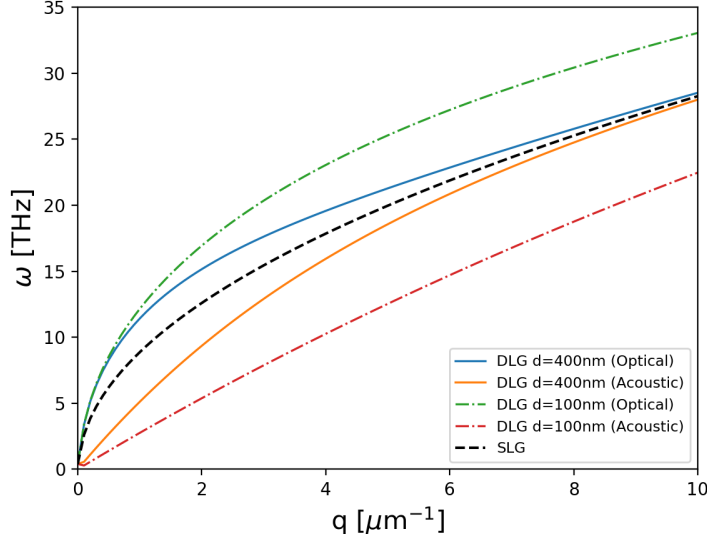


Figure 5.6: TM GSP dispersion relation in a double-layer graphene structure for $d = 100\text{nm}$ (solid lines) and $d = 400\text{nm}$ (dot-dashed lines). The black dashed line represents the dispersion relation of a single-layer graphene, to which the splitting of the spectrum can be compared to. Parameters: $\epsilon_1 = \epsilon_2 = \epsilon_3 = 1$, $\gamma = 0$ and $E_F = 0.45\text{ eV}$.

5.2.2 Alternative approach to DLG dispersion

The transfer-matrix method for SLG and DLG configurations were discussed previously in Sec. (4.3), which resulted in the reflection and transmission coefficients. It turns out that this method can also be used to derive the condition for plasmonic excitations in any structured N-layer graphene system.

Taking a DLG system, as the one depicted in Fig. 5.5, into consideration, the transfer matrix for the whole geometry is given by $\mathbf{T}_{1 \rightarrow 3}$ in Eq. (4.3.15), where $\mathbf{T}_{2 \rightarrow 3}$ takes the same form as $\mathbf{T}_{1 \rightarrow 2}$, but with η_2 and $\xi_{\sigma,2}$ instead of η_1 and $\xi_{\sigma,1}$. The subscripts refers to the interface at which the quantity is defined, so that

$$\eta_2 \equiv \frac{\epsilon_2 k_{3,z}}{\epsilon_3 k_{2,z}} \quad \text{and} \quad \xi_{\sigma,2} \equiv \frac{\sigma_g k_{3,z}}{\omega \epsilon_0 \epsilon_3}. \quad (5.2.8)$$

The condition for plasmonic excitation in the DLG geometry is found as the poles of the reflection coefficient, which is to say that $\mathbf{T}_{11}^{1 \rightarrow 3} = 0$ since $r_{DLG} = \frac{\mathbf{T}_{21}^{1 \rightarrow 3}}{\mathbf{T}_{11}^{1 \rightarrow 3}}$. Calculating the matrix equation for $\mathbf{T}_{1 \rightarrow 3}$ explicitly with the definitions given in Eq. (4.3.7) and Eq. (5.2.8), and setting $\mathbf{T}_{11}^{1 \rightarrow 3} = 0$ leads to

$$\begin{aligned} e^{-ik_{2,z}d} [1 + \eta_2 + \xi_{\sigma,2} - \eta_1 - \eta_1\eta_2 - \eta_1\xi_{\sigma,2} + \xi_{\sigma,1} + \eta_2\xi_{\sigma,1} + \xi_{\sigma,1}\xi_{\sigma,2}] \\ = e^{ik_{2,z}d} [-1 + \eta_2 - \xi_{\sigma,2} + \eta_1 - \eta_1\eta_2 + \eta_1\xi_{\sigma,2} + \xi_{\sigma,1} - \eta_2\xi_{\sigma,1} + \xi_{\sigma,1}\xi_{\sigma,2}]. \end{aligned} \quad (5.2.9)$$

Inserting the definitions of η_1 , η_2 , $\xi_{\sigma,1}$ and $\xi_{\sigma,2}$ and using that $k_{j,z} = i\sqrt{q^2 - \epsilon_j\omega^2/c^2} \equiv i\kappa_j$ simplifies Eq. (5.2.9) to

$$e^{i\kappa_2 d} \left(\frac{\epsilon_3}{\kappa_3} + i \frac{\sigma_g}{\omega \epsilon_0} - \frac{\epsilon_2}{\kappa_2} \right) \left(\frac{\epsilon_1}{\kappa_1} + i \frac{\sigma_g}{\omega \epsilon_0} - \frac{\epsilon_2}{\kappa_2} \right) = e^{\kappa_2 d} \left(\frac{\epsilon_3}{\kappa_3} + i \frac{\sigma_g}{\omega \epsilon_0} + \frac{\epsilon_2}{\kappa_2} \right) \left(\frac{\epsilon_1}{\kappa_1} + i \frac{\sigma_g}{\omega \epsilon_0} + \frac{\epsilon_2}{\kappa_2} \right), \quad (5.2.10)$$

which is identical to the DLG dispersion relation derived in Sec. (5.2.1). This method works in the case of a single graphene layer as well, where the dispersion relation is derived using the poles of the SLG reflection coefficient instead. Finally it is worth to mention that this procedure can be extended to the ordinary SPPs; The only difference in this case is that $\sigma_g(\omega) = 0$, so that the transfer-matrix across the interface separating the dielectric and the conducting material reads

$$\mathbf{T}_{1 \rightarrow 2}^{SPP} = \begin{bmatrix} 1 + \eta_1 & 1 - \eta_1 \\ 1 - \eta_1 & 1 + \eta_1 \end{bmatrix}. \quad (5.2.11)$$

Chapter 6

Plasmons in Parabolic Waveguides

So far the optical features of SPPs at a metal-dielectric interface and GSPs in flat SLG and DLG structures have been investigated. The findings from these discussions inspire a different group of structures called SPP waveguides. One type of such structures utilizes a metal gap between two dielectrics, also called a DMD waveguide. An example of a DMD waveguide could be that of a parabolic shaped metal surrounded by a dielectric medium¹. One of the prominent advantages of SPP waveguides, is their ability to confine light in the vertical direction as well as the direction parallel to the interface, effectively creating a 1D channel for the wave to propagate in (herein the name waveguide). This degree of confinement thus exceeds that of the SPPs propagating along a flat interface, at which only vertical confinement exists.

The first part of this chapter deals with the theoretical description of surface plasmons propagating along a parabolic shaped waveguide, where the dispersion relation is derived. The second part extends the developed ideas from the first part, working out the dispersion relation for graphene plasmons propagating along parabolic-shaped dielectric bulges and valleys.

6.1 Parabolic Waveguides

This section works out the theoretical description of plasmons propagating along a waveguide with a parabolic-shaped interface, separating two semi-infinite dielectric mediums. The system under consideration have been schematically illustrated in Fig. 6.1, where ϵ_1 and ϵ_2 denotes the dielectric function of the medium making up the surroundings and the parabola, respectively. It is convenient to apply the parabolic cylinder coordinates, denoted ξ , η and z , in order to solve a problem of this character. The transformation between these coordinates and the ordinary Euclidean coordinates reads

¹Although it should be mentioned that a variety of differently shaped waveguides exists in the literature to this date. Examples of such shapes is triangular wedges and grooves, which have been investigated in a graphene-covered version by [24]

$$x = \xi\eta, \quad (6.1.1)$$

$$y = \frac{1}{2}(\eta^2 - \xi^2), \quad (6.1.2)$$

$$z = z, \quad (6.1.3)$$

where $-\infty \leq \xi \leq \infty$ and $0 \leq \eta \leq \infty$. The interface separating the two domains can then simply be understood in terms of the η coordinate, meaning that $\eta < \eta_0$ is occupied by the parabolic channel, while $\eta > \eta_0$ is occupied by the surrounding medium.

Now, this system can be handled in two different scenarios: One can assume that a non-zero current exist at the interface, which is to say that $\sigma_{2D}(\omega) \neq 0$, or the system may be solved in the more simple case, where $\sigma_{2D}(\omega) = 0$ ². This section will deal with the latter approach, while Sec. (6.2) deals with the former.

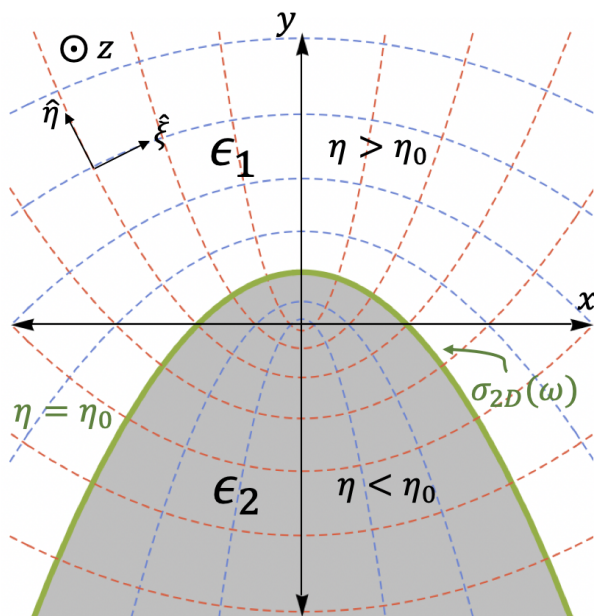


Figure 6.1: Schematic illustration of the cross section through a parabolic waveguide in the xy -plane. The interface of the waveguide at $\eta = \eta_0$ separates two semi-infinite mediums, where the dielectric function of the material restricted to the region $\eta < \eta_0$ is denoted ϵ_2 , while the dielectric function of the medium occupying $\eta > \eta_0$ is given by ϵ_1 . In Sec. (6.1) the dispersion relation is worked out in the case of $\sigma_{2D}(\omega) = 0$, whereas the same structure covered with graphene is analyzed in Sec. (6.2), i.e. $\sigma_{2D}(\omega) \neq 0$.

6.1.1 Dispersion relation

The dispersion relation will be derived in the electrostatic limit, which means that the modes of the parabola is found through solutions to Laplace's equation $\nabla^2\Phi = 0$, where Φ denotes the electrostatic potential given by $\Phi(\xi, \eta, z, t) = \phi(\xi, \eta, z)e^{i\omega t}$. Assuming that the system under consideration is translational invariant along the z -direction, the scalar potential for the electromagnetic field can be decomposed to

²This geometry have been considered in Refs [25, 26]

$$\Phi(\mathbf{r}) = \phi(\xi, \eta)e^{iqz}, \quad (6.1.4)$$

where the harmonic time dependence have been explicitly assumed and will be so throughout the rest of the derivation. Inserting this potential into Laplace's equation yields

$$\nabla^2 \Phi = \frac{1}{\xi^2 + \eta^2} \left[\frac{\partial^2 \phi(\xi, \eta)}{\partial \xi^2} + \frac{\partial^2 \phi(\xi, \eta)}{\partial \eta^2} \right] - q^2 \phi(\xi, \eta) = 0, \quad (6.1.5)$$

where the Laplacian in parabolic cylinder coordinates have been used. This partial differential equation can be solved using separation of variables. In order to carry out this calculation, the potential $\phi(\xi, \eta)$ is split into two functions, $F(\xi)$ and $G(\eta)$, describing the ξ and η dependence respectively, which lead to the following two differential equations

$$-\frac{\partial^2 F(\xi)}{\partial \xi^2} + [q^2 \xi^2 - E] F(\xi) = 0, \quad (6.1.6)$$

$$\frac{\partial^2 G(\eta)}{\partial \eta^2} - [q^2 \eta^2 + E] G(\eta) = 0, \quad (6.1.7)$$

where E denotes the separation constant. It becomes apparent that Eq. (6.1.6) is similar to the Schrödinger equation of the quantum harmonic oscillator³, to which the eigenmodes are well-know. The functions solving this differential equation is therefore, by analogy, given by

$$F(\xi) = C_{n,q} e^{-q\xi^2/2} H_n(\sqrt{q}\xi), \quad (6.1.8)$$

where H_n is the n 'th Hermite polynomial and the separation constant takes the following discrete values

$$E = q(2n + 1), \quad (6.1.9)$$

for $n = 0, 1, 2, \dots$. The normalization constant is given by

$$C_{n,q} = \frac{1}{\sqrt{2^n n!}} \left(\frac{q}{\pi} \right)^{1/4}, \quad (6.1.10)$$

³The Schrödinger equation for the harmonic oscillator with $\hbar = m = 1$ reads $-\frac{1}{2} \frac{\partial^2 \psi}{\partial x^2} + (\frac{1}{2} \omega^2 x^2 - E) \psi = 0$. Multiplying this equation through by 2 and utilizing the transformations $\omega \rightarrow q$ and $x \rightarrow \xi$ leads to $\frac{\partial^2 F(\xi)}{\partial \xi^2} + (E' - q^2 \xi^2) F(\xi) = 0$, where $E' = 2E = q(2n + 1)$.

which means that the solution to Eq. (6.1.6), and consequently Eq. (6.1.7), can be labelled by the discrete number n . The potential can now be written as $\Phi(\xi, \eta, z) = \Phi_{n,q}(\xi, \eta, z)$ to show its dependence on the discrete number, n , as well as the continuous wavevector, q [25]. The differential equation describing the η dependence is now written in terms of a new variable $\mu = \eta\sqrt{2q}$, which leads to

$$\frac{\partial^2 G(\eta)}{\partial \mu^2} - \left[n + \frac{1}{2} + \frac{\mu^2}{4} \right] G(\eta) = 0. \quad (6.1.11)$$

This equation is identified with the parabolic cylinder differential equation with solutions given by the parabolic cylinder functions $U\left(n + \frac{1}{2}, \mu\right)$ and $V\left(n + \frac{1}{2}, \mu\right)$ [27]. V and U increases and decays exponentially with μ respectively, which leads to the choice of V being the solution inside the parabolic channel and U the solution outside of it. This choice of solutions ensures the localized nature of the modes to the interface of the channel. Combining the solutions of the two differential equations (6.1.6) and (6.1.7) yields

$$\Phi_{n,q}(\xi, \eta) = \begin{cases} A_{n,q} F_n(\xi) U\left(n + \frac{1}{2}, \eta\sqrt{2q}\right) e^{iqz} & \text{for } \eta \geq \eta_0, \\ B_{n,q} F_n(\xi) V\left(n + \frac{1}{2}, \eta\sqrt{2q}\right) e^{iqz} & \text{for } \eta \leq \eta_0. \end{cases} \quad (6.1.12)$$

As usual, the potential at each side of the interface is related by appliance of the appropriate boundary conditions, which in this case is the continuity of the electric potential and the normal component of the electric displacement field across the interface separating the two dielectric mediums, I.e.

$$\phi_1^n(\xi, \eta) \Big|_{\eta=\eta_0} = \phi_2^n(\xi, \eta) \Big|_{\eta=\eta_0}, \quad (6.1.13)$$

and

$$\epsilon_1 \frac{\partial \phi_1^n(\xi, \eta)}{\partial \eta} \Big|_{\eta=\eta_0} = \epsilon_2 \frac{\partial \phi_2^n(\xi, \eta)}{\partial \eta} \Big|_{\eta=\eta_0}, \quad (6.1.14)$$

where ϕ_1^n and ϕ_2^n denotes the potential of the n 'th mode in the surrounding medium and the parabolic channel respectively. Substituting the electrostatic potential in Eq. (6.1.12) into these boundary conditions leads to the following condition for the spectrum of the electrostatic surface modes localized at the apex of the parabolic channel

$$\epsilon_2 = \epsilon_1 \frac{V\left(n + \frac{1}{2}, \eta_0\sqrt{2q}\right) U'\left(n + \frac{1}{2}, \eta_0\sqrt{2q}\right)}{U\left(n + \frac{1}{2}, \eta_0\sqrt{2q}\right) V'\left(n + \frac{1}{2}, \eta_0\sqrt{2q}\right)}, \quad (6.1.15)$$

where the prime denotes the differential with respect to the argument.

Assuming that the parabolic channel is made up of a free electron lossless Drude metal, I.e $\epsilon_2 = 1 - \omega_p^2/\omega^2$, and surrounded by a dielectric medium with ϵ_1 , the dispersion relation becomes

$$\omega_n(q) = \omega_p \left[1 - \epsilon_1 \frac{V\left(n + \frac{1}{2}, \eta_0 \sqrt{2q}\right) U'\left(n + \frac{1}{2}, \eta_0 \sqrt{2q}\right)}{U\left(n + \frac{1}{2}, \eta_0 \sqrt{2q}\right) V'\left(n + \frac{1}{2}, \eta_0 \sqrt{2q}\right)} \right]^{-1/2} \quad (6.1.16)$$

This dispersion relation of the electrostatic surface modes at the edge of the parabolic channel have been shown in Fig. 6.2, where the first four modes are shown together. The even values of n corresponds to even modes with respect to $\xi = 0$, while odd values of n leads to odd modes instead. It is clearly seen that all the modes approaches the same asymptotic value, which is that of the surface plasmon frequency for a flat dielectric-metal interface, ω_{sp} , illustrated by the black-dashed line. Since the normalized first axis is given by $\eta_0 \sqrt{2q}$, there is two ways to verify this limit, which is in terms of the wavevector q and the fixed coordinate η_0 . Arguing in terms of the wavevector, it is seen that the asymptotic value is reached when the wavevector goes toward large values. Consequently the wavelength approaches zero since $\lambda_{SPP} = \frac{2\pi}{q_{SPP}}$, which means that the apex of the parabolic channel appears as a flat interface to the SPP, and thus ω_{sp} is re-established. On the other hand, if η_0 tends to ∞ , then the curvature of the parabola tends to zero, meaning that the interface approaches that of a flat surface.

An alternative approach to this derivation is given in appendix (C), where plasmonic excitations at the apex of a hyperbolic shaped waveguide is discussed.

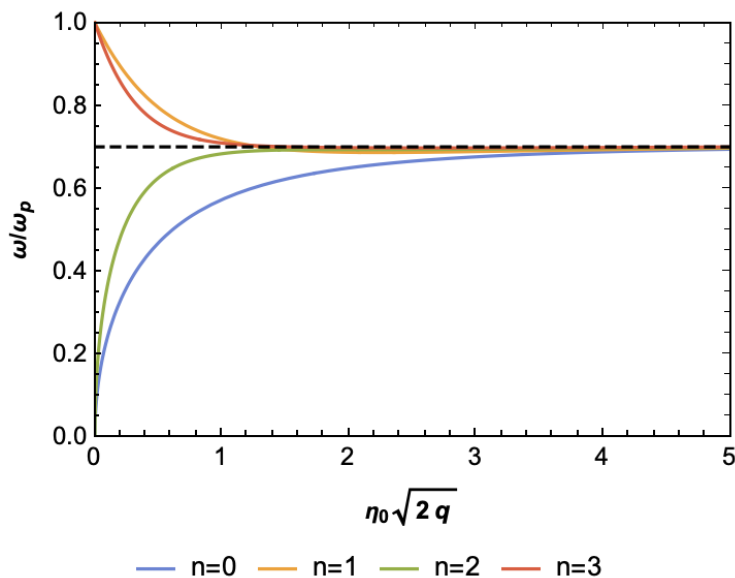


Figure 6.2: Plot of the dispersion relation related to the electrostatic surface modes of the parabolic channel. The first four modes is shown by the colored lines, while the black-dashed line indicates the surface plasmon frequency ω_{sp} as a reference point.

6.2 Graphene-covered parabolic waveguide: Bulges and Valleys

The procedure developed in the previous section is now performed on a dielectric channel of the same structure, i.e. parabola, but now covered in a sheet of graphene. Consequently a charge density is introduced at the interface separating the channel from the surrounding dielectric, defined as $\eta = \eta_0$. One can think of two different versions of such a case, which is the parabolic bulge and valley, these structures have been sketched in Fig. 6.3. Graphene plasmons propagating along this bulge and valley will be denoted bulge graphene plasmons (BGPs) and valley graphene plasmons (VGPs) respectively.

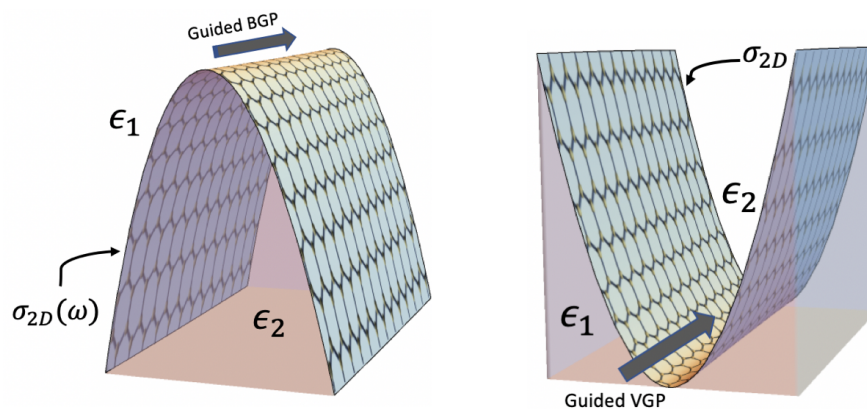


Figure 6.3: Left picture illustrates a channel plasmon polariton propagating along the apex of a graphene-covered parabolic bulge, while the right picture shows the same thing but along the graphene-covered parabolic valley.

The surface charge density leads to a surface conductivity, which effectively encapsulates the response of graphene to the electromagnetic radiation.

Once again, the dispersion relation is derived using the electrostatic limit. However, with graphene present at the interface, the plasmon excitations is found as the solution to Poisson's equation $\nabla^2\Phi(\mathbf{r}) = \frac{\rho(\mathbf{r})}{\epsilon_0}$, as opposed to Sec. (6.1), where the modes were derived using Laplace's equation. Thus the problem at hand deals with an inhomogeneous partial differential equation, which is solved by a linear combination of the solutions to the corresponding homogeneous equation. Consequently the electric potential in medium 1 and 2 is given by

$$\phi_1(\xi, \eta) = \sum_n A_n F_n(\xi) U\left(n + \frac{1}{2}, \eta\sqrt{2q}\right), \quad (6.2.1)$$

and

$$\phi_2(\xi, \eta) = \sum_n B_n F_n(\xi) V \left(n + \frac{1}{2}, \eta \sqrt{2q} \right), \quad (6.2.2)$$

respectively. The definitions $Y_n \equiv Y \left(n + \frac{1}{2}, \mu \right)$, $Y_n^0 \equiv \left(n + \frac{1}{2}, \mu_0 \right)$ and $Y_n'^0 \equiv \frac{\partial Y_n}{\partial \eta} \Big|_{\eta=\eta_0}$, with $Y = \{U, V\}$ and $\mu_0 = \eta_0 \sqrt{2q}$ will be used in the rest of this section in order to shortening the notation. The presence of the graphene sheet at the interface, $\eta = \eta_0$, modifies the boundary conditions from Sec. (6.1) to

$$\phi_1(\xi, \eta) \Big|_{\eta=\eta_0} = \phi_2(\xi, \eta) \Big|_{\eta=\eta_0}, \quad (6.2.3)$$

and

$$\epsilon_1 \frac{\partial \phi_1(\xi, \eta)}{\partial \eta} \Big|_{\eta=\eta_0} - \epsilon_2 \frac{\partial \phi_2(\xi, \eta)}{\partial \eta} \Big|_{\eta=\eta_0} = \frac{\rho_{2D}(\xi, \eta = \eta_0)}{\epsilon_0}. \quad (6.2.4)$$

The charge density $\rho_{2D}(\xi, \eta = \eta_0)$ can be expressed in terms of the potential using the continuity equation in combination with Ohm's law⁴

$$\rho_{2D}(\xi, \eta = \eta_0) = \frac{i\sigma_{2D}(\omega)}{\omega} \left[\frac{1}{\xi^2 + \eta^2} \frac{\partial^2 \phi_1(\xi, \eta)}{\partial \xi^2} - q^2 \phi_1(\xi, \eta) \right] \Big|_{\eta=\eta_0}. \quad (6.2.5)$$

Inserting this expression together with the potentials from Eq. (6.2.1)-(6.2.2) into the boundary condition in Eq. (6.2.4) leads to

$$\begin{aligned} & \sum_n A_n \frac{\epsilon_1}{\sqrt{\xi^2 + \eta_0^2}} F_n(\xi) U_n'^0 \sqrt{2q} - \sum_m B_m \frac{\epsilon_2}{\sqrt{\xi^2 + \eta_0^2}} F_m(\xi) V_m'^0 \sqrt{2q} \\ & = \frac{\sigma_{2D}(\omega)}{i\omega\epsilon_0} \left[\frac{1}{\xi^2 + \eta_0^2} \sum_j A_j U_j^0 \frac{\partial^2 F_j(\xi)}{\partial \xi^2} - q^2 \sum_j A_j F_j(\xi) U_j^0 \right], \end{aligned} \quad (6.2.6)$$

where the gradient in parabolic cylinder coordinates have been used and the factor of $\sqrt{2q}$ appears from the chain rule used to normalize the differentials on the left hand side. The second order derivative in ξ can be simplified using that $\partial_\xi^2 F_j(\xi) = (q^2 \xi^2 - E^2) F_j(\xi)$ from Eq. (6.1.6). This simplification combined with a multiplication of $F_l(\xi)$ and integration over ξ from $-\infty$ to ∞ leads to the following eigenvalue equation⁵

⁴Assuming harmonic time dependence, the continuity equation in two dimensions can be cast into $i\omega\rho_{2D}(\mathbf{r}) = \nabla_{2D} \cdot \mathbf{J}_{2D}$, and thus we get $\rho_{2D}(\mathbf{r}) = (i\omega)^{-1} \nabla_{2D} \cdot \mathbf{J}_{2D}$. Introducing Ohm's law given by $\mathbf{J}_{2D} = \sigma \mathbf{E}(\mathbf{r})$ and writing the electric field in terms of the potential yields $\rho_{2D}(\mathbf{r}) = i(\omega)^{-1} \sigma [\nabla_{2D}^2 \cdot \phi]$.

⁵Where the orthogonality of the Hermite polynomials, $\int_{-\infty}^{\infty} e^{-x^2} H_n(x) dx = \delta_{n,m}$, have been used [27].

$$\frac{\sqrt{2}}{q} \frac{i\omega\epsilon_0}{\sigma_{2D}(\omega)} A_l = \sum_{j=0}^{\infty} M_{lj} A_j, \quad (6.2.7)$$

where the elements of the matrix M_{lj} reads

$$M_{lj} = -(2j+1+b^2) \frac{V_l^0 U_j^0}{\epsilon_1 V_l^0 U_l'^0 - \epsilon_2 U_l^0 V_l'^0} \int_{-\infty}^{\infty} \frac{dx}{\sqrt{x^2+b^2}} F_l(x) F_j(x), \quad (6.2.8)$$

with $f_n(x) = \frac{1}{\sqrt{2^n n!}} \frac{1}{\pi^{1/4}} H_n(x)$ and the dimensionless parameters defined as $x \equiv \xi\sqrt{q}$ and $b = q\sqrt{\eta_0}$. It becomes clear in the interpretation of Eq. (6.2.7) that the eigenvalue to the matrix M_{lj} is given by

$$\lambda_\nu(q) = \frac{\sqrt{2}}{q} \frac{i\omega\epsilon_0}{\sigma_{2D}(\omega)}, \quad (6.2.9)$$

where the subscript ν denotes the mode eigenindex. A simple version of the dispersion relation can now be obtained under the assumption that the graphene sheet is well-described by a Drude-like lossless conductivity, i.e. $\sigma_{2D}(\omega) = i\frac{\sigma_0}{\pi} \frac{4E_F}{\hbar\omega}$. The eigenvalue equation then leads to the following energy-wavevector dispersion relation

$$\boxed{\Omega_\nu(q) = \Omega_{flat}(q) \sqrt{\frac{\epsilon_1 + \epsilon_2}{\sqrt{2}} \lambda_\nu(q)}}, \quad (6.2.10)$$

where $\Omega \equiv \hbar\omega$ and $\Omega_{flat}(q) = \sqrt{\frac{4\alpha E_F \hbar c}{\epsilon_1 + \epsilon_2}}$ is the flat graphene dispersion relation [11]. This relation holds for both the VGPs and BGPs, which corresponds to an interchange between ϵ_1 and ϵ_2 .

The dispersion relation given by Eq. (6.2.10) have been illustrated for the first three modes in Fig. 6.4 for both the bulge and the valley, shown in blue, orange and green from lowest to highest mode. The spectrum thus exhibits the same discrete nature as the Drude-metal parabolic guide discussed in the previous section. First and foremost, it is seen that the lowest order mode achieves larger wavevectors as compared to higher modes for a fixed frequency, which turns out to be a general trend throughout all of the presented configurations. Comparison between panel a) and b) indicates that an increase in the curvature of the parabola leads to larger wavevectors for the same frequency⁶. Consequently the field

⁶Using the transformations between the eucladian and parabolic coordinates in Eq. (6.1.3), it can be shown that the parabola follows the curve defined by $y = -\frac{1}{2\eta_0^2} x^2 + \frac{1}{2}\eta_0^2$, from which it is observed that the curvature is given by $a = \frac{1}{2\eta_0^2}$. The η_0 defining the parabolic interface is thus inversely proportional to the curvature, i.e. $\eta_0 = \sqrt{\frac{1}{2a}}$.

confinement in the vicinity of the apex is larger for a more narrow bulge. Furthermore, it is noticed that all the modes tends toward the flat graphene dispersion relation (black-dashed line) for the curvature of the bulge going to zero. Analysing panel a), c) and d) all together reveals that plasmons in the bulge attains larger field confinement than the case of identical environment, which in turn has a larger degree of confinement than the parabolic valley.

It is concluded from Fig. 6.4 that the dispersion relation of the graphene-covered parabolic bulge and valley lies beneath that of the flat graphene for sufficiently large curvatures, which means that these geometries is able to achieve ultra-confined surface plasmons, exceeding the already well-confined GSPs at flat graphene interfaces. On a last note, it is observed that all the modes lie far to the right of the light line (red-dashed curve), which is a natural consequence of this outstanding confinement. The electrostatic limit, on which these results have been derived, is therefore well suited for this system.

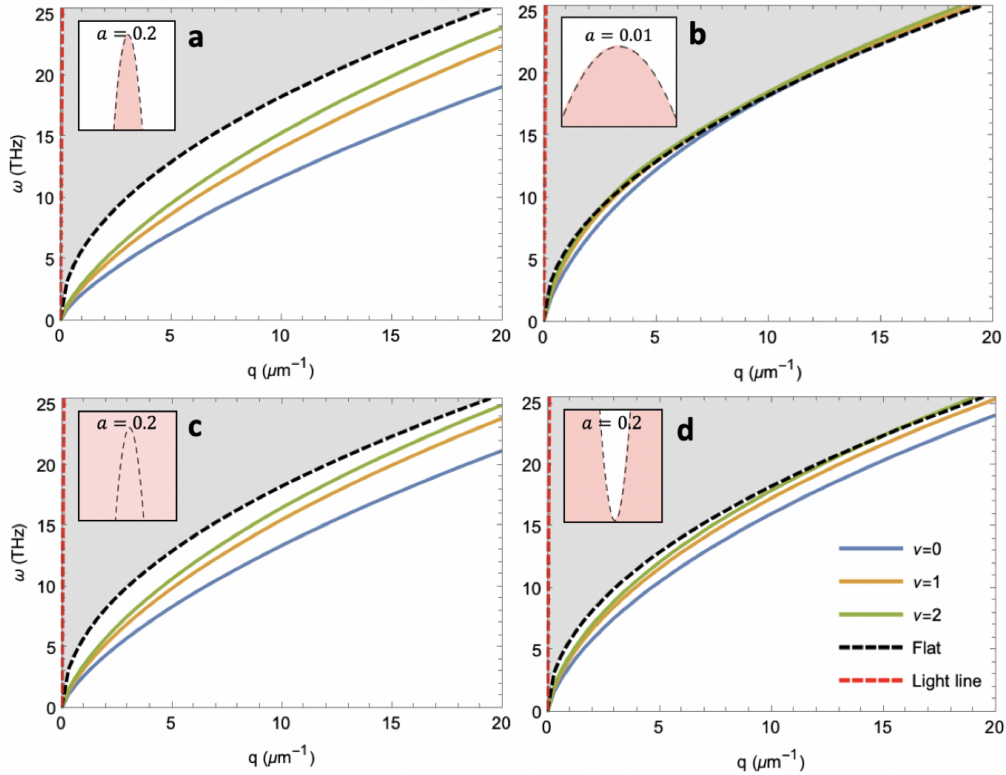


Figure 6.4: Dispersion relation of graphene plasmons in parabolic bulges and valleys. Part **a)** and **b)** illustrates the spectrum of BGPs for two different curvatures of the graphene-covered bulge, while part **d)** shows a single example of the dispersion relation for the inverse configuration, i.e. VGP. $\epsilon_1 = 1$ and $\epsilon_2 = 4$ have been used in **a)** and **b)**, followed by $\epsilon_1 = 4$ and $\epsilon_2 = 1$ in **d)**. Part **c)** depicts the spectrum of BGPs, where the dielectric constant of the surrounding medium is identical to the one making up the parabolic channel with $\epsilon_1 = \epsilon_2 = 2.5$. All the plots is produced using Eq. (6.2.10) with $E_F = 0.5$.

It is desirable to get an insight into the behaviour of the electric potential near the apex of the parabolic bulge, or equivalently the bottom of the parabolic valley. In order to find this potential, one must first find the elements of the eigenvectors entering in Eq. (6.2.7). Inserting these elements in the expansion of Eq. (6.2.1)-(6.2.2), and transforming the parabolic cylinder coordinates back to the euclidian ones, provides the potential in medium 1 and 2 through ϕ_1 and ϕ_2 , respectively. The electric potential for the first two modes in the parabolic bulge configuration have been showed in Fig. 6.5 for $a = 0.2$ and fixed frequency of $\omega = 10$ THz. It is observed that the lowest mode exhibits larger field confinement than the second-lowest mode, which is in agreement with the previous discussion regarding the dispersion relation. The frequency of the incoming light corresponds to a wavelength of $\lambda_0 = 30 \mu\text{m}$, which is many times larger than the field localization of the lowest mode shown in Fig. 6.5, where the potential extends to a few hundreds of nm in both directions. It should be mentioned that the electric potential of the parabolic valley, with identical curvature, displays a similar behaviour as the parabolic bulge, only with slightly less confinement. These potential plots therefore support our previous claim of the great degree of field confinement in the parabolic bulge and valley geometries.

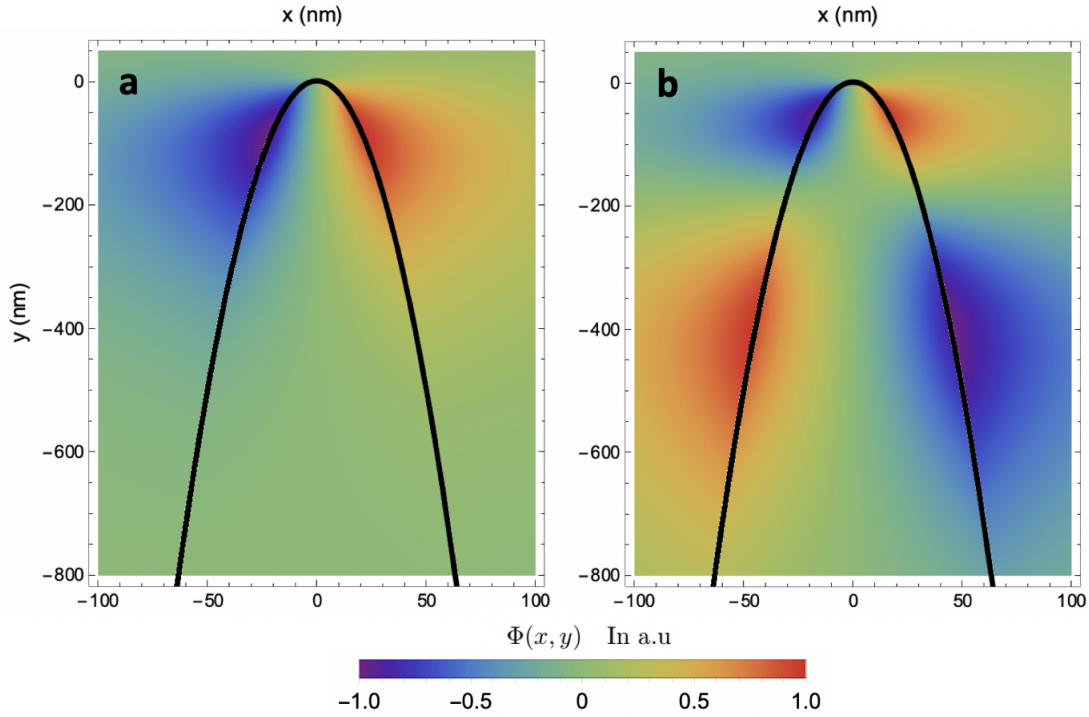


Figure 6.5: Cross section of the graphene-covered parabolic bulge with curvature $a = 0.2$ (solid black line) superimposed onto a colormap, which represents the potential $\phi(x, y)$. Plot a) and b) illustrates the lowest and second lowest mode for the bulge with a fixed frequency of $\omega_c = 10$ THz. Both plots are shown in nm scale and the parameters have been chosen as $E_F = 0.5$ eV, $\epsilon_1 = 1$ and $\epsilon_2 = 4$, which corresponds to plot a) of Fig. 6.4.

Chapter 7

Conclusions And Outlook

This thesis has presented a broad range of plasmonic systems in three and two dimensions, which have been described in the framework of classical electrodynamics.

First and foremost, the fundamental concepts of classical electrodynamics was presented, which, among other things, included Maxwell's equations, the constitutive relations and the corresponding boundary conditions. These definitions was then used together with the Drude model to work out the basic formalism of SPPs sustained at single and double dielectric-metal interfaces. Analysing the single interface revealed that the lossless Drude metal dispersion relation was located to the right of the light-line at all times, asymptotically approaching the surface plasmon frequency ω_{sp} , while the Drude metal with losses was limited to finite values of q , eventually "bending back" to the left side of the light-line. The analysis of the lossless double dielectric-metal interface was done in the form of symmetric MDM and DMD geometries, which showed a tendency of the modes to hybridize for sufficiently small separation between the two interfaces, arising because of the interaction of the modes in the middle medium. One striking difference between these modes was that the high- and low-frequency version, as the name suggests, attained larger and smaller frequencies as compared to the single interface plasmon. It was therefore concluded that the field confinement of the low-frequency mode is higher than that of the high-frequency mode.

The optical and electronic properties of graphene was then reviewed, where the real and reciprocal lattice description of graphene was established. This information, in combination with the tight-binding model, lead to the electronic band structure of graphene, from which a particle-hole symmetric structure was found. Furthermore, performing a Taylor-expansion around the symmetry point \mathbf{K} resulted in a linear band structure. Consequently the free charge carriers in graphene behave as massless Dirac fermions, which obeys the relativistic Dirac Hamiltonian. The conductivity of graphene was discussed, dealing with intraband and interband contributions separately. Utilizing suitable assumptions and considerations simplified the overall graphene conductivity to that of a Drude-like intraband conductivity, which was concluded to be valid for frequencies between THz and mid-IR. An outline of the transfer-matrix method was given in the case of single and double planar graphene

configurations, from which the reflection, transmission and absorbance was derived in both cases. The absorbance of the single graphene sheet turned out to approach a constant level of 2.3 % for frequencies in the visible part of the spectrum.

The insights of the optoelectronic properties of graphene was then used in combination with the techniques developed in the beginning of the thesis, in order to describe plasmonic excitations in single and double layered graphene systems. It was concluded that both systems acquired a great degree of field confinement in the THz spectral range, and that the GSPs could be actively tuned by simply adjusting the doping level. Once again, the appearance of hybridized modes was observed for the double interface geometry, whose separation increased (decreased) for a decrease (increase) of the distance between the interfaces. consequently two single graphene interface dispersion relations was re-established in the limit of $d \rightarrow \infty$. This discussion was followed by an alternative approach to the derivation of DLG dispersion, which was centralised around the idea of using the pole of the reflection coefficient instead. The dispersion relation of a Drude metal parabolic waveguide have been derived in the framework of parabolic cylinder coordinates in the electrostatic limit. The dispersion relation was analysed in the $\eta_0 \rightarrow \infty$ and the $q \rightarrow \infty$ limit, which both yielded the same conclusion, stating that the dispersion relation tended towards that of a single flat dielectric-metal interface. The same procedure was then performed for the graphene-covered dielectric parabolic bulge and valley. The dispersion relation for the BGP and the VGP was then presented. The modes of both structures was reported to lie beneath the flat graphene dispersion relation, which indicates an increase in localization of the GSPs. The findings indicated that the field confinement in the parabolic bulge was greater than in the parabolic valley. This confinement could be further improved by increasing the curvature of the parabolic bulge channel. Finally the corresponding potential for a fixed frequency was shown for the parabolic bulge, which served as an alternative argument for the field confinement and verified the localization in the vicinity of the apex.

The localized potential portrayed for the graphene-covered parabolic channels is largely retained for a range of different curvatures and frequencies. These parabolic channels therefore serve as an ideal candidate for a possible plasmonic component in an optoelectronic device, where sub-wavelength waveguiding is of importance [28, 29]. In this context different sizes of the channel can be designed, meeting the relevant requirements for the device.

An example of such a device could be processing microchips, at which the number of transistors have doubled every second year for the past several decades [30]. This immense increase of data transfer have started to put pressure on the electrical interconnects, which turns into "bottlenecks", limiting the overall performance of the chip [31]. These limitations could be solved by substituting the currently operating interconnects with the graphene-covered waveguide.

On a last note, the developed formalism of the graphene-covered channels could potentially be used in the future for the investigation of local disturbances in an otherwise flat graphene sheet [32], which take an approximate shape of a parabolic bulge or valley.

Appendices

Appendix A

Transparency of Graphene

It was seen in Sec. (4.3.1) that the optical transparency of graphene could be derived in the discussion of the transfer-matrix method. This transparency tended towards a constant value in the regime of visible wavelengths. This appendix serves to show an alternative way to derive the same result, but now given in terms of the fine-structure constant.

A.1 Transmittance of Monolayered Graphene

The discussion of the transparency of a single graphene layer is here carried out under the assumption that the electric field has an orthogonal incidence on the two-dimensional graphene sheet ($k_x = k_y = 0$), meaning that the graphene occupies the xy -plane. The amplitude of the electric field is in this case given by

$$E = E_0 e^{i\mathbf{k}\mathbf{r}} = e^{ik_0 n^* z} = E_0 e^{ik_0 n z} e^{-k_0 \kappa z}, \quad (\text{A.1.1})$$

where $n^* = n + i\kappa$ is the imaginary valued refractive index. The intensity of the radiation is proportional to the square of the absolute value of the electric field

$$I \propto |E|^2 = E_0^2 |e^{ik_0 n z}|^2 |e^{-k_0 \kappa z}|^2 = E_0^2 e^{-2k_0 \kappa z}. \quad (\text{A.1.2})$$

The transmittance through a graphene monolayer of thickness d is then computed by taking the ratio between the intensity of the incoming and outgoing light

$$T = \frac{I}{I_0} = \frac{E_0^2 e^{-2k_0 \kappa d}}{E_0^2} \approx 1 - 2k_0 \kappa d, \quad (\text{A.1.3})$$

where it has been assumed that the thickness d of the graphene sheet is very small. All that is left to do at this point, in order to find the transmittance, is to find the imaginary part of the refractive index, κ .

The refractive index reads $n^* = \sqrt{\epsilon_0 \mu_0}$, and is simplified under the assumption that the graphene sheet is non-magnetic ($\mu_0 = 1$). The relative permittivity is given in terms of the susceptibility $\epsilon_0 = 1 + \chi$, which leads to the following rewriting of the refractive index

$$n^* = \sqrt{1 + \chi} \approx 1 + \frac{1}{2}\chi, \quad (\text{A.1.4})$$

where a Taylor expansion have been utilized. An expression for χ is found by using the polarization density

$$\mathbf{P}(\omega) = \epsilon_0 \chi(\omega) \mathbf{E}(\omega), \quad (\text{A.1.5})$$

in combination with the current density

$$\mathbf{J}(\omega) = \sigma_{3D}(\omega) \mathbf{E}(\omega). \quad (\text{A.1.6})$$

A change in the polarization density with time induces an associated current density, which are given by

$$\mathbf{J}_P(\omega) = \frac{\partial \mathbf{P}(t)}{\partial t} = -i\omega \mathbf{E}(t) \epsilon_0 \chi(\omega). \quad (\text{A.1.7})$$

Hence, by inspection from Eq. (A.1.6) and Eq. (A.1.7), the conductivity is found to be

$$\sigma_{3D}(\omega) = -i\omega \epsilon_0 \chi(\omega). \quad (\text{A.1.8})$$

Isolating for the susceptibility yields¹

$$\chi(\omega) = \frac{i\sigma_{3D}(\omega)}{\omega \epsilon_0} = \frac{i\sigma_{2D}(\omega)}{\omega \epsilon_0 d}, \quad (\text{A.1.9})$$

which is now inserted back into Eq. (A.1.4), leading to

$$n^* \approx 1 + \frac{i\sigma_{2D}(\omega)}{2d\epsilon_0\omega}. \quad (\text{A.1.10})$$

The imaginary part of the refractive index is found by comparing Eq. (A.1.10) to $n^* = n + i\kappa$, obtaining

¹The 3D conductivity is related to the 2D conductivity through the following simple relation $\sigma_{2D} = d\sigma_{3D}$.

$$\kappa(\omega) = \frac{\text{Re}\{\sigma_{2D}\}}{2d\omega\epsilon_0}. \quad (\text{A.1.11})$$

Finally, the transmittance of a single graphene sheet is computed by substituting this expression into Eq. (A.1.3)

$$T = 1 - \frac{\text{Re}\{\sigma_{2D}\}}{c\epsilon_0} = 1 - \frac{\sigma_0}{c\epsilon_0}. \quad (\text{A.1.12})$$

This is the final result of the transmittance. However, this result can be written in a more elegant way, in terms of the fine-structure constant

$$T = 1 - \pi\alpha \approx 97,7\%, \quad (\text{A.1.13})$$

meaning that a single layer of graphene is able to absorb 2,3% of the incoming radiation. This relatively high value of the absorption for a single graphene sheet can actually be seen with the naked eye in a microscope, which have been illustrated in Fig. A.1.

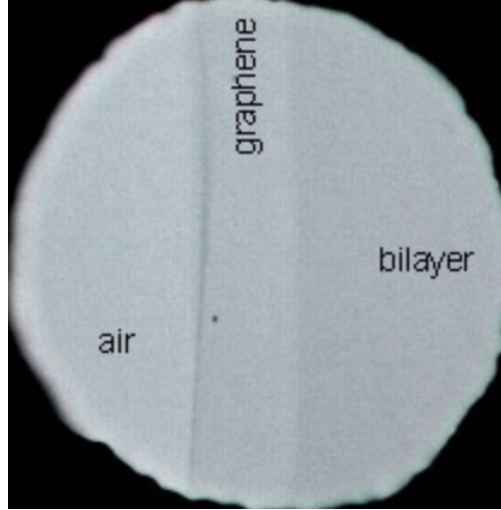


Figure A.1: Graphene placed in conventional light microscope. It is possible to see the boundary between the single graphene sheet and air because of the great ability of graphene to absorb light at visible frequencies [33].

Appendix B

Excitation of GSPs

It is not possible to excite the SPPs in graphene directly by electromagnetic radiation, because of the discrepancy between the wavevector of the incoming beam and that of the GSP. This becomes evident in the single-layered GSP dispersion plot in Fig. 5.2a, where the momentum of the GSP lies to the right of the light line at all times. This natural restriction of the GSPs also exists for the SPPs at metal-dielectric interfaces, and thus alternative excitation techniques is sought as well in these systems.

B.1 Prism coupling: Otto configuration

It is possible to couple the incident TM electromagnetic wave to the GSP by the aid of a prism, which has a dielectric constant greater than that of the surroundings. Total internal reflection, meaning that $\theta > \theta_c = \sin^{-1}(\epsilon_{diel}/\epsilon_{prism})$, inside the prism creates evanescent waves able to couple to the SPP of the plasmonic material, or the graphene sheet. This coupling takes place once the in-plane momentum of the light

$$q = \frac{\omega}{c} \sqrt{\epsilon_{prism}} \sin(\theta), \quad (\text{B.1.1})$$

equals the momentum of the GSP. The Otto configuration, which have been schematically illustrated in Fig. B.1, can be used in order to excite GSPs with a prism [34].

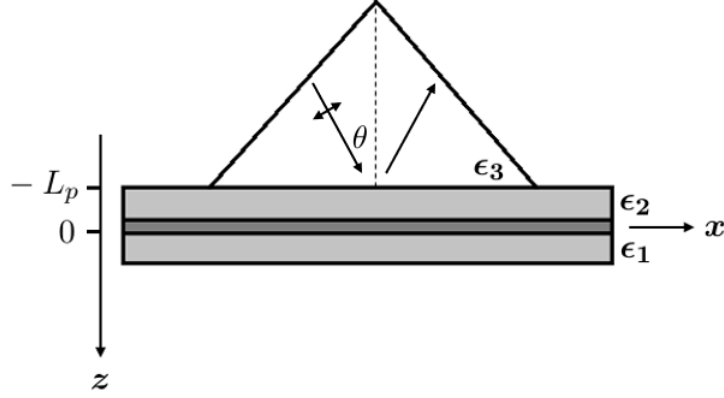


Figure B.1: SLG in the Otto configuration. The lower medium (ϵ_1) and the prism (ϵ_3) is assumed to be semi-infinite. The graphene sheet is placed at $z = 0$ and the prism at $z = -L_p$.

The red ring in Fig. B.2 indicates the momentum match in this configuration. It is clearly seen that the wavevector of the light shifts towards larger values in the presence of the prism (green dashed line), as compared to the wavevector value in air (orange dashed line).

The match of the momenta, and hence the excitation of the GSP, can equally be observed as a brief decrease in the reflected wave. The derivation of this reflectance takes as its starting point the electromagnetic fields together with the boundary conditions. Assuming total internal reflection in the prism, these fields takes the following form for $-L_p > z$

$$\mathbf{E}_3(\mathbf{r}) = \left(E_{3,x}^{(i)}, 0, E_{3,z}^{(i)} \right) e^{i\mathbf{k}_i \cdot \mathbf{r}} + \left(E_{3,x}^{(r)}, 0, E_{3,z}^{(r)} \right) e^{-i\mathbf{k}_i \cdot \mathbf{r}}, \quad (\text{B.1.2})$$

$$\mathbf{B}_3(\mathbf{r}) = \left(0, B_{3,y}^{(i)}, 0 \right) e^{i\mathbf{k}_i \cdot \mathbf{r}} + \left(0, B_{3,y}^{(r)}, 0 \right) e^{-i\mathbf{k}_i \cdot \mathbf{r}}, \quad (\text{B.1.3})$$

where i and r denotes the incoming and reflected beam in the prism, respectively. Consequently we have $\mathbf{k}_i = \sqrt{\epsilon_3} \omega / c (\sin \theta, 0, \cos \theta)$ and $\mathbf{k}_r = \sqrt{\epsilon_3} \omega / c (\sin \theta, 0, -\cos \theta)$. Exponentially growing and decaying waves in the medium defined by $-L_p < z < 0$, leads to

$$\mathbf{E}_2(\mathbf{r}) = \left[\left(E_{2,x}^{(+)}, 0, E_{2,z}^{(+)} \right) e^{\kappa_2 |z|} + \left(E_{2,x}^{(-)}, 0, E_{2,z}^{(-)} \right) e^{-\kappa_2 |z|} \right] e^{iqx}, \quad (\text{B.1.4})$$

$$\mathbf{B}_2(\mathbf{r}) = \left[\left(0, B_{2,y}^{(+)}, 0 \right) e^{\kappa_2 |z|} + \left(0, B_{2,y}^{(-)}, 0 \right) e^{-\kappa_2 |z|} \right] e^{iqx}, \quad (\text{B.1.5})$$

with $\kappa_2 = \sqrt{q^2 - \epsilon_2 \omega^2 / c^2}$, and where $q = \sqrt{\epsilon_3} \omega / c \sin(\theta)$ depicts the in-plane momentum.

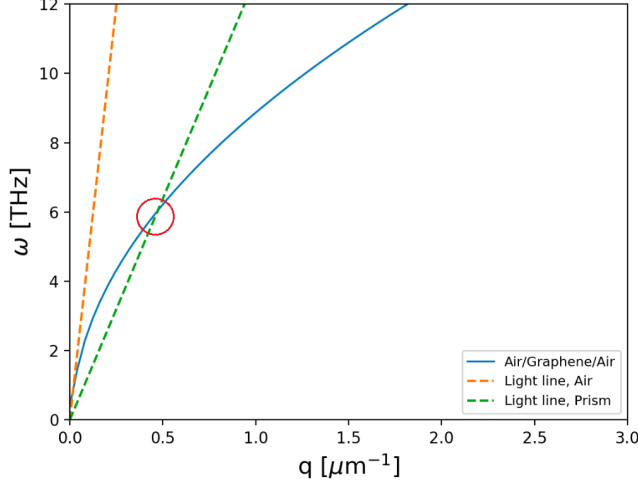


Figure B.2: Depiction of the prism coupling technique to excite GSPs in the otto configuration. The solid blue line indicates the TM GSP dispersion, while the orange dashed and green dashed lines represents the light line in air and the prism, respectively. Parameters: $E_F = 0.45$ eV, $\epsilon_1 = \epsilon_2 = 1$ and $\epsilon_3 = 14$

The last medium, bounded by $z > 0$, takes the usual form for a TM bound wave propagating along the x-direction

$$\mathbf{E}_1(\mathbf{r}) = (E_{1,x}, 0, E_{1,z})e^{-\kappa_1|z|}e^{iqx}, \quad (\text{B.1.6})$$

$$\mathbf{B}_1(\mathbf{r}) = (0, B_{1,y}, 0)e^{-\kappa_1|z|}e^{iqx}, \quad (\text{B.1.7})$$

with $\kappa_1 = \sqrt{q^2 - \omega^2/c^2\epsilon_1}$. The usual harmonic time dependence $e^{-i\omega t}$ will be assumed in the derivation. The boundary condition at $z = -L_p$ reads

$$E_{3,x}^{(i)}e^{-ik_{3,z}L_p} + E_{3,x}^{(r)}e^{ik_{3,z}L_p} = E_{2,x}^{(+)}e^{\kappa_2L_p} + E_{2,x}^{(-)}e^{-\kappa_2L_p}, \quad (\text{B.1.8})$$

$$B_{3,x}^{(i)}e^{-ik_{3,z}L_p} + B_{3,x}^{(r)}e^{ik_{3,z}L_p} = B_{2,x}^{(+)}e^{\kappa_2L_p} + B_{2,x}^{(-)}e^{-\kappa_2L_p}, \quad (\text{B.1.9})$$

while the boundary condition for $z = 0$ gives

$$E_{2,x}^{(+)} + E_{2,x}^{(-)} = E_{1,x}, \quad (\text{B.1.10})$$

$$B_{2,y}^{(+)} + B_{2,y}^{(-)} = B_{1,y} + \mu_0\sigma(\omega)E_{1,x}, \quad (\text{B.1.11})$$

where $\sigma(\omega)$ expresses the dynamical conductivity of graphene. A relationship between the magnetic ($B_{j,y}$) and electric field amplitudes ($E_{j,x}$ and $E_{j,x}^{(\pm)}$) is obtained through Maxwell's equations. Connecting these amplitudes leads to four equations, which constitute a linear system, written in matrix form as

$$\mathbf{M}_{SLG}^{otto} \begin{bmatrix} E_{3,x}^{(r)}/E_{3,x}^{(i)} \\ E_{2,x}^{(+)} / E_{3,x}^{(i)} \\ E_{2,x}^{(-)} / E_{3,x}^{(i)} \\ E_{1,x} / E_{3,x}^{(i)} \end{bmatrix} = \begin{bmatrix} e^{-ik_{3,z}L_p} \\ -\frac{\epsilon_3}{k_{3,z}} \\ 0 \\ 0 \end{bmatrix}, \quad (\text{B.1.12})$$

where

$$\mathbf{M}_{SLG}^{otto} = \begin{bmatrix} -e^{ik_{3,z}L_p} & e^{\kappa_2L_p} & e^{-\kappa_2L_p} & 0 \\ -\frac{\epsilon_3}{k_{3,z}}e^{ik_{3,z}L_p} & i\frac{\epsilon_2}{\kappa_2}e^{\kappa_2L_p} & -i\frac{\epsilon_2}{\kappa_2}e^{-\kappa_2L_p} & 0 \\ 0 & -1 & -1 & 1 \\ 0 & -\frac{\epsilon_2}{\kappa_2} & \frac{\epsilon_2}{\kappa_2} & \frac{\epsilon_2}{\kappa_2} + i\frac{\sigma(\omega)}{\omega\epsilon_0} \end{bmatrix}. \quad (\text{B.1.13})$$

The reflection coefficient is in general given by the ratio between the incoming and outgoing beam, which turns out to be the first entry in the vector on the left hand side in Eq. (B.1.12). This entry can be found by the use of Cramer's rule [35]

$$r = \frac{E_{3,x}^{(r)}}{E_{3,x}^{(i)}} = \frac{\det(\mathbf{m}_{SLG}^{otto})}{\det(\mathbf{M}_{SLG}^{otto})}, \quad (\text{B.1.14})$$

where \mathbf{m}_{SLG}^{otto} is made by changing the first column in \mathbf{M}_{SLG}^{otto} to that of the column vector on the right hand side of Eq. (B.1.12). The reflectance can now be evaluated from the modulus squared of the reflection coefficient, which yields

$$R_{SLG}^{otto} = \left| \frac{\Xi^* \Lambda^- + \Xi \Lambda^+ e^{2\kappa_2L_p}}{\Xi \Lambda^- + \Xi^* \Lambda^+ e^{2\kappa_2L_p}} \right|^2. \quad (\text{B.1.15})$$

The asterisk symbol in the above equation represents the complex conjugate and the following definitions have been used

$$\Xi = \epsilon_3 \kappa_2 + i \epsilon_2 k_{3,z}, \quad (\text{B.1.16})$$

$$\Lambda^\pm = \epsilon_2 \kappa_1 \pm \epsilon_1 \kappa_2 \pm \kappa_1 \kappa_2 \frac{i\sigma}{\omega\epsilon_0}, \quad (\text{B.1.17})$$

for the sake of simplicity. Taking the conductivity to be purely imaginary, meaning that $\text{Re}\{\sigma\} = 0$, the denominator equals the complex conjugate of the nominator, and hence $R_{SLG}^{otto} = 1$. All the energy from the incoming beam is therefore reflected¹, which is in accordance with the physical interpretation of the real part of the conductivity.

¹This would correspond to setting $\gamma = 0$ in the Drude-like conductivity for graphene, at which no losses is present in the system.

Detection of GSP excitations is depicted in Fig. B.3. The general idea is to look for points where the reflectance goes to approximately zero, which indicates GSP excitation. Two common approaches for the detection of GSP excitation is to measure the reflectance as a function of the incident angle, while the frequency is held constant, or measuring the reflectance as a function of frequency for a fixed angle. These procedures is illustrated in panel a) and panel c) in Fig. B.3. It is seen in panel a) that the decrease in reflectance occurs at increasingly higher angles when the frequency is raised. This behaviour is caused by the fact that the in-plane momentum is proportional to ω , and thus the match in momentum will happen for larger angles. The same argumentation holds for the observations made in panel c), where larger angles leads to resonance at higher frequencies, because the in-plane momentum is proportional to $\sin(\theta)$. These two approaches for detection of GSP excitation is shown together in panel d), where a color map with both the angle and frequency dependence of the reflectance, $R(\omega, \theta)$, is illustrated. The blue parts of the map corresponds to the right combination of angle and frequency needed to excite GSPs in the Otto configuration. Finally the influence of the doping level on the reflectance is shown in panel b).

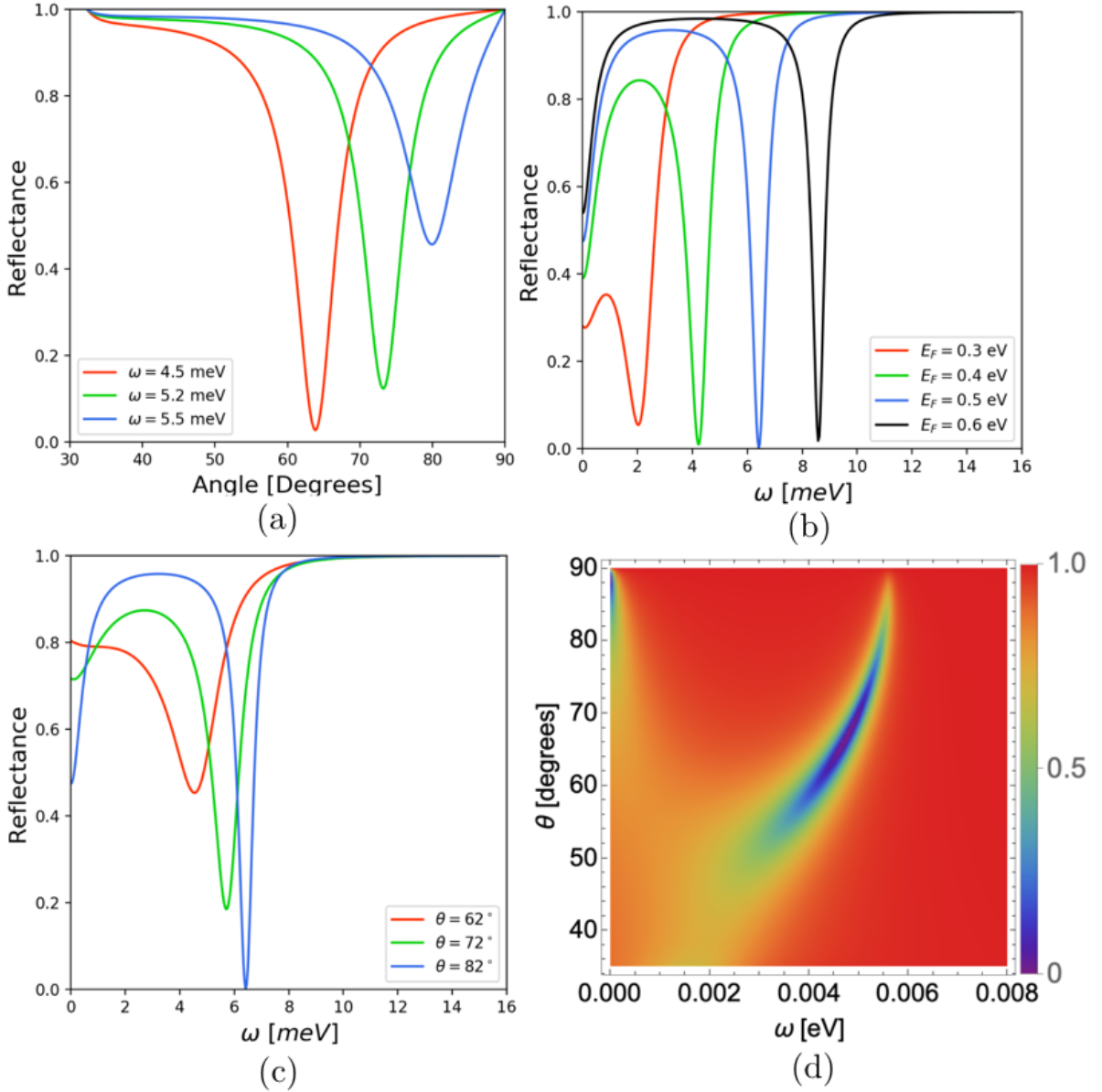


Figure B.3: Otto configuration used to produce propagating GSPs. **a)** Reflectance as a function of the angle for three arbitrary frequencies with $E_F = 0.5$ eV, identifying correct circumstances for exciting GSPs. **b)** Reflectance as a function of frequency with four different doping levels, where the angle have been fixed to $\theta = 82^\circ$. Parameters in a) and b): $\epsilon_1 = 4$, $\epsilon_2 = 1$, $\epsilon_3 = 14$, $\hbar\gamma = 0.1$ meV and $L_p = 2.5$ μm . **c)** Reflectance as a function of frequency for three distinct angles with a fixed doping level $E_F = 0$. **d)** Density plot of the reflectance as a function of the angle and the frequency, where $E_F = 0.5$ eV. Parameters in c) and d): $\epsilon_1 = \epsilon_2 = 4$, $\epsilon_3 = 14$, $\hbar\gamma = 0.1$ μm and $L_p = 20$ μm .

Appendix C

Guided Plasmons in the Hyperbolic Wedge Geometry

An alternative structure to the parabolic wedge for CPPs is that of the hyperbolic shape [25, 36, 26]. The hyperbolic geometry will, as the parabolic shape, lead to ultra confined electromagnetic radiation. The discussion of the hyperbolic structure can indeed be seen as an alternative approach to the parabolic one, since the rounding edge in the hyperbolic cylinder to first approximation looks like the parabolic cylinder.

C.1 Elliptic cylinder coordinate system

It is advantageous to adapt the elliptic cylinder coordinate system in the discussion and derivation of the electrostatic edge modes of the hyperbolic wedge, this coordinate system is shown in Fig C.1. A given location in space is now given by the coordinates u and ν , where $0 \leq u \leq \infty$, $-\alpha \leq \nu \leq \alpha$ and $-\infty \leq z \leq \infty$. The transformation between the ordinary Cartesian and elliptic cylinder coordinate system are given by

$$x = a \cosh(u) \cos(\nu) \tag{C.1.1a}$$

$$y = a \sinh(u) \sin(\nu) \tag{C.1.1b}$$

$$z = z, \tag{C.1.1c}$$

where a is the focus of the elliptic coordinate. Finally the laplacian in these coordinates takes the following form

$$\nabla^2 \Phi = \frac{1}{a^2(\sinh^2(u) \sin^2(\nu))} \left(\frac{\partial^2 \Phi}{\partial u^2} + \frac{\partial^2 \Phi}{\partial \nu^2} \right) + \frac{\partial^2 \Phi}{\partial z^2}. \tag{C.1.2}$$

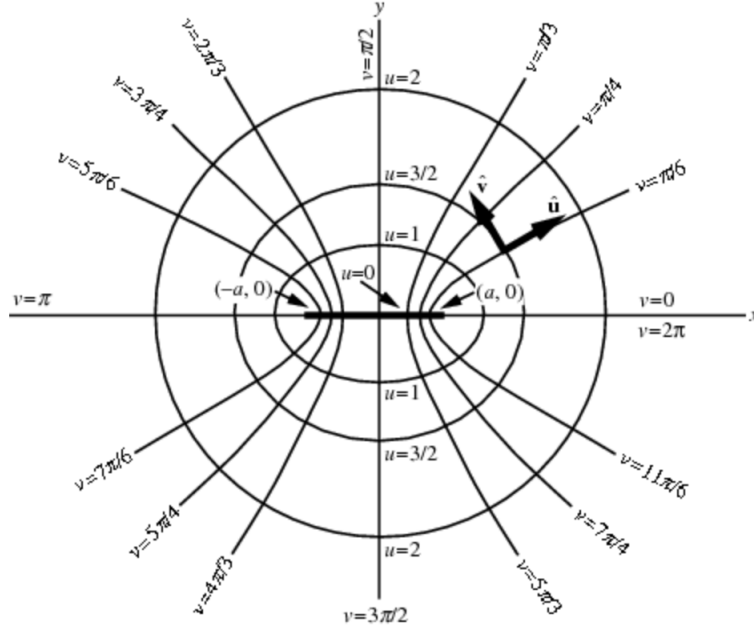


Figure C.1: Elliptic cylinder coordinate system with the coordinates u , ν and z , which points into the paper [37].

C.2 Laplace's Equation

The hyperbolic wedge is taken to occupy the space bounded by $-\alpha \leq \nu \leq \alpha$ (α is some angle between 0 and $\pi/4$), $u \geq 0$ and $-\infty \leq z \leq \infty$. The electrostatic edge modes of this dielectric wedge is found as the solution to Laplace's equation for the potential $\Phi(u, \nu, z, t)$

$$\nabla^2 \Phi(u, \nu, z, t) = 0. \quad (\text{C.2.1})$$

Translational invariance is assumed along the z -axis, which means that the z -dependence of the potential can be written in terms of a simple exponential

$$\Phi(u, \nu, z, t) = \phi(u, \nu) e^{i(kz - \omega t)}. \quad (\text{C.2.2})$$

ω and k , as usual, denotes the frequency and wave number respectively. Substituting this potential into Eq. (C.2.1) yields

$$\nabla^2 \Phi = \frac{e^{i(kz - \omega t)}}{a^2(\sinh^2(u) + \sin^2(\nu))} \left(\frac{\partial^2 \phi(u, \nu)}{\partial u^2} + \frac{\partial^2 \phi(u, \nu)}{\partial \nu^2} \right) + \frac{\partial^2 (e^{i(kz - \omega t)})}{\partial z^2} \phi(u, \nu) = 0 \quad (\text{C.2.3})$$

$$\frac{\partial^2 \phi(u, \nu)}{\partial u^2} + \frac{\partial^2 \phi(u, \nu)}{\partial \nu^2} - a^2 k^2 [\sinh^2(u) + \sin^2(\nu)] \phi(u, \nu) = 0 \quad (\text{C.2.4})$$

One way to solve this equation is to factorize the potential, so that $\phi(u, \nu) = f(u)g(\nu)$. This factorization means that Laplace's equation can be solved by separation of variables. More specifically, Eq. (C.2.4) yields two differential equations [26], one for the elliptic coordinate

$$\frac{d^2 g(\nu)}{d\nu^2} + [-E_n - 2q \cos(2\nu)] g(\nu) = 0, \quad (\text{C.2.5})$$

and one for the angular coordinate

$$\frac{d^2 f(u)}{du^2} - [-E_n - 2q \cosh(2u)] f(u) = 0, \quad (\text{C.2.6})$$

where

$$q = -\frac{k^2 a^2}{4}, \quad (\text{C.2.7})$$

and E_n is the separation constant. This separation constant is found as a perturbed version of the eigenvalues of the quantum harmonic oscillator (with a parabolic potential), given that we are sufficiently close to the rounding edge of the hyperbolic shape. These two differential equations will now be analysed separately.

C.2.1 Angular differential equation

It becomes apparent that Eq. (C.2.5) can be identified with the Mathieu differential equation, which has as its general solution a linear combination of Mathieu functions of real order [27]

$$g(\nu) = A c e_n(\nu, q) + B s e_n(\nu, q) \quad (\text{C.2.8})$$

with

$$c e_n(\nu, q) = \cos(\mu_n \nu) + \sum_{r=1}^{\infty} q^r c_r(\nu), \quad (\text{C.2.9})$$

$$s e_n(\nu, q) = \sin(\mu_n \nu) + \sum_{r=1}^{\infty} q^r s_r(\nu). \quad (\text{C.2.10})$$

μ is the order of the Mathieu function, while s_r and c_r are the Mathieu coefficients [38]. The functions $c e_n$ and $s e_n$ have distinct symmetry properties with respect to the midplane corresponding to the x-axis, or $\nu = 0$ ($\nu = \pi$) for the dielectric (vacuum) medium.

C.2.2 Elliptic differential equation

Taking a closer look at the elliptic differential equation, this equation can be written as

$$\frac{d^2 f}{du^2} - \frac{df}{du} \coth(u) + \frac{df}{du} \coth(u) - (-E_n - 2q \cosh(u)) = 0, \quad (\text{C.2.11})$$

where the u dependence of the function f is implicit. This expression may be written in terms of alternative trigonometric functions

$$\underbrace{\frac{d^2 f}{du^2} \left[\frac{\cosh^2(u)}{\sinh^2(u)} - \frac{1}{\sinh^2(u)} \right] + \frac{df}{du} \left[\frac{\cosh(u)}{\sinh^3(u)} - \frac{\cosh^3(u)}{\sinh^3(u)} \right] + \frac{df}{du} \frac{\cosh(u)}{\sinh(u)} - (-E_n - 2q \cosh(2u))}_{\mu(u)} = 0. \quad (\text{C.2.12})$$

The four terms inside $\mu(u)$ is rewritten in the following way

$$\begin{aligned} \mu(u) &= \left[\frac{d^2 f}{du^2} \frac{1}{\sinh^2(u)} - \frac{df}{du} \frac{\coth(u) \operatorname{csch}(u)}{\sinh(u)} \right] (\cosh^2(u) - 1) \\ &= \frac{1}{\sinh(u)} \left[\frac{d^2 f}{du^2} \frac{1}{\sinh(u)} - \frac{df}{du} \coth(u) \operatorname{csch}(u) \right] (\cosh^2(u) - 1) \\ &= \frac{1}{\sinh(u)} \frac{d}{du} \left[\frac{df}{du} \frac{1}{\sinh(u)} \right] (\cosh^2(u) - 1). \end{aligned} \quad (\text{C.2.13})$$

Substituting $\mu(u)$ back into Eq. (C.2.12) leads to

$$\left[\frac{1}{\sinh(u)} \frac{d}{du} \left(\frac{df}{du} \frac{1}{\sinh(u)} \right) \right] (\cosh^2(u) - 1) + \frac{df}{du} \frac{\cosh(u)}{\sinh(u)} - (-E_n - 2q \cosh(2q)) = 0. \quad (\text{C.2.14})$$

Using the chain rule backwards on the square parenthesis on the left-hand side yields

$$\frac{df}{du} \frac{1}{\sinh(u)} = \frac{df}{du} \left[\frac{d[\cosh(u)]}{du} \right]^{-1} = \frac{df}{du} \frac{du}{d[\cosh(u)]} = \frac{df}{d[\cosh(u)]}. \quad (\text{C.2.15})$$

Inserting this result back into Eq. (C.2.14) leads to

$$\frac{d^2 f}{d[\cosh(u)]^2} (\cosh^2(u) - 1) + \frac{df}{du} \frac{\cosh(u)}{\sinh(u)} - (-E_n - 2q \cosh(2q)) = 0. \quad (\text{C.2.16})$$

The identity $\cosh(2x) = 2\cosh^2(x) - 1$ is then exploited in the last term on the left-hand side

$$\frac{d^2 f}{d[\cosh(u)]^2} (\cosh^2(u) - 1) + \frac{df \cosh(u)}{du \sinh(u)} - (-4q \cosh^2(u) - E_n + 2q) = 0. \quad (\text{C.2.17})$$

Multiplying by one in the form of $\frac{-4q}{-4q}$ and $\frac{2\sqrt{-q}}{2\sqrt{-q}}$ leads to the following expression

$$\frac{df}{d[\cosh(u)]^2} \frac{1}{-4q} [-4q \cosh^2(u) + 4q] + \frac{2\sqrt{-q}}{2\sqrt{-q}} \frac{df}{d[\cosh(u)]} - [-4q \cosh^2(u) - E_n + 2q] = 0. \quad (\text{C.2.18})$$

Finally, the definition $h \equiv 2\sqrt{-q} \cosh(u)$ brings Eq. (C.2.18) on the form of the modified Bessel equation with an inhomogeneous term

$$h^2 \frac{d^2 h}{dh^2} + h \frac{df}{dh} - (h^2 - E_n + 2q) = -4q \frac{d^2 f}{dh^2}. \quad (\text{C.2.19})$$

Writing the original elliptic differential equation (C.2.6) in terms of the modified Bessel equation (C.2.19) turns out to be of great advantage in the computation of the general solution. The solution to the homogeneous part of Eq. (C.2.19) (i.e. the complementary solution) is given as a linear combination of the modified Bessel functions with imaginary order

$$y_c = c_1 I_{i\alpha}(h) + c_2 K_{i\alpha}(h), \quad (\text{C.2.20})$$

where $I_{i\alpha}(h)$ and $K_{i\alpha}(h)$ denotes the modified Bessel function of first and second kind respectively and $\alpha = (E_n + k^2 a^2 / 2)^{1/2}$. The asymptotic behaviour of the modified Bessel functions is well know, where $I_{i\alpha}(h)$ increases exponentially and $K_{i\alpha}(h)$ decreases exponentially. Hence c_1 in Eq. (C.2.20) is set to zero, in order to make physical sense of the final result. Knowing the two linearly independent solutions to the homogeneous version, the solution to the inhomogeneous Bessel equation (i.e the particular solution) can be found [39]

$$f^{inh}(h) = K_{i\alpha}(h) \int^h dt I_{i\alpha}(t) \left(\frac{4q}{t} \frac{d^2 f^{inh}(t)}{dt^2} \right) - I_{i\alpha}(h) \int^h dt K_{i\alpha}(t) \left(\frac{4q}{t} \frac{d^2 f^{inh}(t)}{dt^2} \right) + \text{constant}. \quad (\text{C.2.21})$$

The general solution to (C.2.6) is then found by adding together the complementary and particular solution

$$f(h) = c \times K_{i\alpha} + f^{inh}(h) \quad (\text{C.2.22})$$

C.3 Dispersion relation

The electrostatic potential is now found by combining the general solution for the angular and elliptic differential equation. As mentioned earlier, the angular equation yields both an even and an odd solution with respect to the midplane ($\nu = 0$), which then naturally leads to an even potential

$$\phi_n^e(u, \nu, z) = \begin{cases} Af(u)ce_n(\nu, q)e^{i(kz-\omega t)} & \text{for } -\alpha < \eta < \alpha \\ Bf(u)ce_n(\pi - \nu, q)e^{i(kz-\omega t)} & \text{for } \alpha < \eta < 2\pi - \alpha \end{cases}, \quad (\text{C.3.1})$$

and an odd potential

$$\phi_n^o(u, \nu, z) = \begin{cases} Cf(u)se_n(\nu, q)e^{i(kz-\omega t)} & \text{for } -\alpha < \eta < \alpha \\ Df(u)se_n(\pi - \nu, q)e^{i(kz-\omega t)} & \text{for } \alpha < \eta < 2\pi - \alpha \end{cases}, \quad (\text{C.3.2})$$

where $ce_n(\nu, q)$, $se_n(\nu, q)$ and $f(u)$ are given by Eq. (C.2.9), (C.2.10) and (C.2.22) respectively. The constants A , B , C and D is then identified by utilizing the following two boundary conditions

$$\frac{\partial \phi_1}{\partial \nu} \epsilon_1 \Big|_{\nu=\nu_0} = \frac{\partial \phi_2}{\partial \nu} \epsilon_2(\omega) \Big|_{\nu=\nu_0}, \quad (\text{C.3.3})$$

$$\phi_1 \Big|_{\nu=\nu_0} = \phi_2 \Big|_{\nu=\nu_0}, \quad (\text{C.3.4})$$

where ϵ_1 and $\epsilon_2(\omega)$ refers to the the dielectric function of surrounding dielectric and metal respectively. Applying these boundary conditions leads to the even and odd dielectric function

$$\epsilon_2(\omega) = -\frac{ce_n(\nu, q)ce'_n(\pi - \nu, q)}{ce'_n(\nu, q)ce_n(\pi - \nu, q)} \quad (\text{even mode}), \quad (\text{C.3.5})$$

$$\epsilon_2(\omega) = -\frac{se_n(\nu, q)se'_n(\pi - \nu, q)}{se'_n(\nu, q)se_n(\pi - \nu, q)} \quad (\text{odd mode}), \quad (\text{C.3.6})$$

where the prime denotes differentiation with respect to the argument. This dielectric function is shown in the left panel of Fig. C.2 for the first four modes. It is worth noticing that all the modes approach $\epsilon_2 = -1$ for $q \rightarrow \infty$.

Assuming that the optical behaviour of the metal, which makes up the hyperbolic shape, can be described by the Drude model leads to

$$1 - \frac{\omega^2}{\omega_p^2} = \begin{cases} -\frac{ce_n(\nu, q)ce'_n(\pi - \nu, q)}{ce'_n(\nu, q)ce_n(\pi - \nu, q)} & (\text{even mode}) \\ -\frac{se_n(\nu, q)se'_n(\pi - \nu, q)}{se'_n(\nu, q)se_n(\pi - \nu, q)} & (\text{odd mode}). \end{cases} \quad (\text{C.3.7})$$

Isolating for the normalized frequency then yield the following dispersion relation for the hyperbolic waveguide

$$\frac{\omega}{\omega_p} = \sqrt{\frac{ce'_n(\nu, q)ce_n(\pi - \nu, q)}{ce'_n(\nu, q)ce_n(\pi - \nu, q) + ce_n(\nu, q)ce'_n(\pi - \nu, q)}}, \quad (\text{C.3.8})$$

for the even modes, and

$$\frac{\omega}{\omega_p} = \sqrt{\frac{se'_n(\nu, q)se_n(\pi - \nu, q)}{se'_n(\nu, q)se_n(\pi - \nu, q) + se_n(\nu, q)se'_n(\pi - \nu, q)}}, \quad (\text{C.3.9})$$

for the odd modes. These dispersion relations is illustrated in the right panel of Fig. C.2. It is once again seen that all the modes tends toward the same asymptotic value. This value is in agreement with the surface plasmon frequency for SPPs propagating at a planar interface separating a metal and a dielectric. The sense of this agreement can be argued in two different ways: i) When $q \rightarrow \infty$ then $\lambda_{SPP} \rightarrow 0$, and thus the surface seems flat locally for the SPP. ii) The hyperbolic structure in Fig. C.1 becomes a flat surface As $a \rightarrow \infty$. Finally one notices that the even modes starts at zero in right panel, while the odd modes start at one, which was also the case for the dispersion relation in the planar DMD geometry.

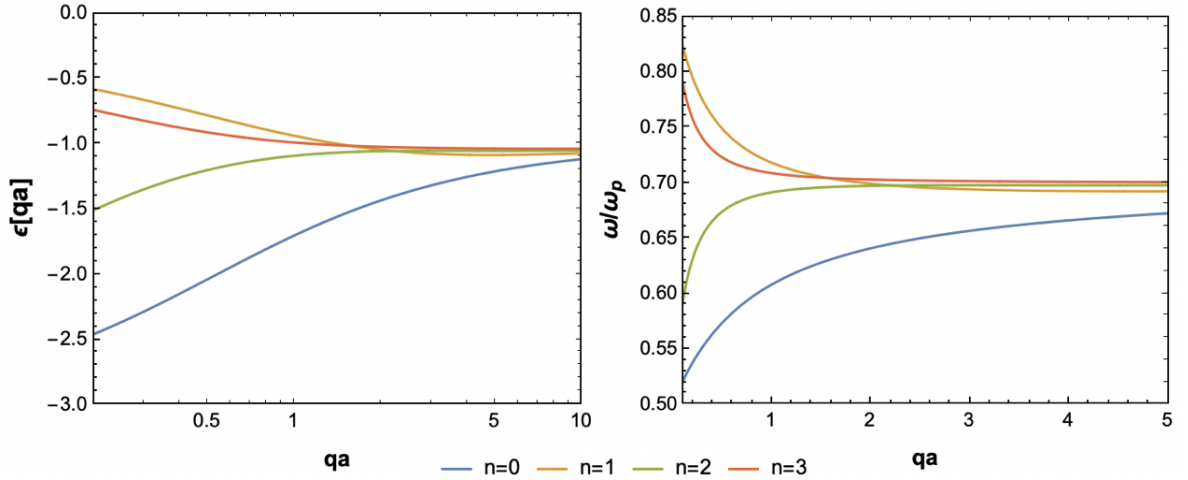


Figure C.2: Left Panel) Dielectric function of the first four modes for SPPs propagating along a hyperbolic shaped waveguide. Right Panel) Corresponding dispersion relation, where the metal have been modelled as a Drude metal with $\gamma = 0$.

Bibliography

- [1] J. C. Maxwell, “Viii. a dynamical theory of the electromagnetic field,” *Philosophical transactions of the Royal Society of London*, no. 155, pp. 459–512, 1865.
- [2] D. Pines and D. Bohm, “A collective description of electron interactions: Ii. collective vs individual particle aspects of the interactions,” *Phys. Rev.*, vol. 85, pp. 338–353, Jan 1952.
- [3] R. H. Ritchie, “Plasma losses by fast electrons in thin films,” *Phys. Rev.*, vol. 106, pp. 874–881, Jun 1957.
- [4] S. A. Maier, *Plasmonics: Fundamentals and Applications*. Springer, (2007).
- [5] K. S. Novoselov, A. K. Geim, S. V. Morozov, D. Jiang, Y. Zhang, S. V. Dubonos, I. V. Grigorieva, and A. A. Firsov, “Electric field effect in atomically thin carbon films,” *science*, vol. 306, no. 5696, pp. 666–669, 2004.
- [6] A. A. Balandin, S. Ghosh, W. Bao, I. Calizo, D. Teweldebrhan, F. Miao, and C. N. Lau, “Superior thermal conductivity of single-layer graphene,” *Nano letters*, vol. 8, no. 3, pp. 902–907, 2008.
- [7] A. C. Neto, F. Guinea, N. M. Peres, K. S. Novoselov, and A. K. Geim, “The electronic properties of graphene,” *Reviews of modern physics*, vol. 81, no. 1, p. 109, (2009).
- [8] J. D. Jackson, *Classical Electrodynamics*. Wiley, 3rd. edition (1998).
- [9] P. Drude, “Zur elektronentheorie der metalle,” *Annalen der physik*, vol. 306, no. 3, pp. 566–613, 1900.
- [10] N. W. Ashcroft and N. D. Mermin, *Solid State Physics*. Harcourt College Publishers, New York, (1976).
- [11] P. A. D. Goncalves and N. M. R. Peres, *An Introduction to Graphene Plasmonics*. World Scientific, Singapore, (2016).
- [12] P. B. Johnson and R.-W. Christy, “Optical constants of the noble metals,” *Physical review B*, vol. 6, no. 12, p. 4370, 1972.

- [13] H. Bruus and K. Flensberg, *Many-Body Quantum Theory in Condensed Matter Physics: An Introduction*. Oxford University Press, (2004).
- [14] P. A. D. Gonçalves, *Plasmonics and Light-Matter Interactions In Two-Dimensional Materials and In Metal Nanostructures*. Springer, (2020).
- [15] R. D. Halliday and K. S. Krane, *Physics Vol. 2*. Wiley, Singapore, 5th edition (2004).
- [16] H. T. Baltar, K. Drozdowicz-Tomsia, and E. M. Goldys, “Propagating surface plasmons and dispersion relations for nanoscale multilayer metallic-dielectric films,” in *Plasmonics-Principles and Applications*, IntechOpen, 2012.
- [17] C. Lee, X. Wei, J. W. Kysar, and J. Hone, “Measurement of the elastic properties and intrinsic strength of monolayer graphene,” *science*, vol. 321, no. 5887, pp. 385–388, 2008.
- [18] L. Pauling, “The nature of the chemical bond. application of results obtained from the quantum mechanics and from a theory of paramagnetic susceptibility to the structure of molecules,” *Journal of the American Chemical Society*, vol. 53, no. 4, pp. 1367–1400, 1931.
- [19] P. R. Wallace, “The band theory of graphite,” *Physical Review*, vol. 71, no. 9, p. 622, 1947.
- [20] L. Falkovsky and A. Varlamov, “Space-time dispersion of graphene conductivity,” *The European Physical Journal B*, vol. 56, no. 4, pp. 281–284, 2007.
- [21] T. Stauber, N. Peres, and A. Geim, “Optical conductivity of graphene in the visible region of the spectrum,” *Physical Review B*, vol. 78, no. 8, p. 085432, 2008.
- [22] V. Gusynin, S. Sharapov, and J. Carbotte, “On the universal ac optical background in graphene,” *New Journal of Physics*, vol. 11, no. 9, p. 095013, 2009.
- [23] T. Zhan, X. Shi, Y. Dai, X. Liu, and J. Zi, “Transfer matrix method for optics in graphene layers,” *Journal of Physics: Condensed Matter*, vol. 25, no. 21, p. 215301, 2013.
- [24] P. A. D. Gonçalves, E. Dias, S. Xiao, M. Vasilevskiy, N. A. Mortensen, and N. Peres, “Graphene plasmons in triangular wedges and grooves,” *ACS Photonics*, vol. 3, no. 11, pp. 2176–2183, 2016.
- [25] L. Dobrzynski and A. A. Maradudin, “Electrostatic edge modes in a dielectric wedge,” *Phys. Rev. B*, vol. 6, pp. 3810–3815, Nov 1972.
- [26] A. D. Boardman, R. Garcia-Molina, A. Gras-Marti, and E. Louis, “Electrostatic edge modes of a hyperbolic dielectric wedge: Analytical solution,” *Phys. Rev. B*, vol. 32, pp. 6045–6047, Nov 1985.

- [27] Abrahamowitz and Stegun, *Handbook of mathematical functions: with formulas, graphs and mathematical tables*. Dover Publications, New York, (1952).
- [28] H. A. Atwater, “The promise of plasmonics,” *Scientific American*, vol. 296, no. 4, pp. 56–63, 2007.
- [29] E. Ozbay, “Plasmonics: merging photonics and electronics at nanoscale dimensions,” *science*, vol. 311, no. 5758, pp. 189–193, 2006.
- [30] M. M. Waldrop, “The chips are down for moore’s law,” *Nature News*, vol. 530, no. 7589, p. 144, 2016.
- [31] Y. I. Ismail, “Interconnect design and limitations in nanoscale technologies,” in *2008 IEEE International Symposium on Circuits and Systems*, pp. 780–783, IEEE, 2008.
- [32] U. Bangert, M. Gass, A. Bleloch, R. Nair, and A. Geim, “Manifestation of ripples in free-standing graphene in lattice images obtained in an aberration-corrected scanning transmission electron microscope,” *physica status solidi (a)*, vol. 206, no. 6, pp. 1117–1122, 2009.
- [33] R. R. Nair, P. Blake, A. N. Grigorenko, K. S. Novoselov, T. J. Booth, T. Stauber, N. M. Peres, and A. K. Geim, “Fine structure constant defines visual transparency of graphene,” *Science*, vol. 320, no. 5881, pp. 1308–1308, 2008.
- [34] A. Otto, “Excitation of nonradiative surface plasma waves in silver by the method of frustrated total reflection,” *Zeitschrift für Physik A Hadrons and nuclei*, vol. 216, no. 4, pp. 398–410, 1968.
- [35] H. Anton and C. Rorres, *Elementary Linear Algebra*. Wiley, Singapore, (2014).
- [36] L. C. Davis, “Electrostatic edge modes of a dielectric wedge,” *Phys. Rev. B*, vol. 14, pp. 5523–5525, Dec 1976.
- [37] “Elliptic cylindrical coordinates.” <https://mathworld.wolfram.com/EllipticCylindricalCoordinates.html>. Accessed: 2020-05-30.
- [38] N. W. McLachlan, *Theory and Applications of Mathieu Functions*. Dover Publications, New York, (1951).
- [39] P. M. Morse and H. Feshbach, *Methods of Theoretical Physics*. McGraw-Hill, New York, (1953).